Simplified Modelling of Semi-Submersible Floating Offshore Wind Turbines for Time-Domain Dynamic Analyses

Auteur : Mertens, Neil
Promoteur(s) : Rigo, Philippe
Faculté : Faculté des Sciences appliquées
Diplôme : Master : ingénieur civil mécanicien, à finalité spécialisée en "Advanced Ship Design"
Année académique : 2022-2023
URI/URL : http://hdl.handle.net/2268.2/19336

Simplified Modelling of Semi-Submersible Floating Offshore Wind Turbines for Time-Domain Dynamic Analyses

submitted on 27 August 2023

by

MERTENS Neil | Am Kornhof 16 | 4761 Rocherath | Belgium | Neil.Mertens@student.uliège.be

Student ID No.: S181689 (ULiège); GA9768682 (UPM)

First Reviewer:

Professor, Sascha, Kosleck

Chair of Ocean Engineering at the University of Rostock

Universitätsplatz 1

18055 Rostock

Germany

Second Reviewer:

Msc., Antonio, Medina Manuel

Junior Researcher at the Polytechnic University of Madrid

Avenida de la Memoria 4

28040 Madrid

Spain

TABLE OF CONTENT

LIST OF FIGURES

LIST OF TABLES

DECLARATION OF AUTHORSHIP

I declare that this thesis and the work presented in it are my own and have been generated by me as the result of my own original research.

Where I have consulted the published work of others, this is always clearly attributed.

Where I have quoted from the work of others, the source is always given. With the exception of such quotations, this thesis is entirely my own work.

I have acknowledged all main sources of help.

Where the thesis is based on work done by myself jointly with others, I have made clear exactly what was done by others and what I have contributed myself.

This thesis contains no material that has been submitted previously, in whole or in part, for the award of any other academic degree or diploma.

I cede copyright of the thesis in favour of the Polytechnic University of Madrid.

Date: 27 August 2023   Signature:

Mertens Neil electronic signature

ACKNOWLEDGEMENTS

ABSTRACT

Offshore wind has great potential for coming years, with the EU-27 countries targeting to nearly quadruple their current capacity of 16.1 GW (end of 2022) to 60 GW by 2030 [Rab23]. Within this field, floating offshore wind turbines (FOWTs) have become an area of great interest due to their capability to operate in greater water depths with higher and steadier wind speeds, achieving significantly higher capacity factors than bottom-fixed turbines, as evidenced in [Equ21]. To facilitate the further development of those floating structures, there is need for reliable numerical software capable of accurately predicting their dynamic behaviour. Furthermore, analysing these systems presents a significant challenge due to the high complexity of the aero-hydro-servo-elastic model, which establishes a coupling between the hydrodynamics of the floater, the structural dynamics and aerodynamics of the turbine, the dynamics of the mooring lines and the complex control system that combines all these aspects.

The objective of this thesis is to identify which modelling parameters are of importance for an accurate evaluation of a floating wind turbine's dynamic behaviour in the basic design stage, with the ultimate goal of creating a simplified model that accurately reflects the turbine's dynamics, while reducing computational expenses. A 3D diffraction and radiation software is used to conduct frequency analyses during conceptual design and results are utilised as inputs for the basic design stage, where a time domain finite element dynamic analysis is performed. An existing model is employed as the reference, and different environmental load cases are utilised to form the design space in which modifications are tested.

The semi-submersible floater concept is utilised for this study, as it offers benefits such as a low life cycle cost, a simple and cost-efficient float-out process, and a suitability for a wide range of water depths, as detailed in [LKC18] and [Mai+20]. Nacelle acceleration, platform pitch and tower base bending moment prove useful to determine the accuracy of the dynamic analysis, for which the *OrcaFlex* software is chosen, while simulation duration is used as a metric for computational cost. A sensitivity analysis reveals that small variations in modelling parameters can result in significant changes in dynamic outputs. Additionally, the intricate interrelationship among diverse domains, encompassing aerodynamics, structural dynamics, and hydrodynamics, is emphasised. The simplified turbine model created in this study provides a good overview over the system dynamics while reducing computational costs significantly. It is well-suited for the comparison of different floater layouts, allowing for rapid, reasonably accurate results.
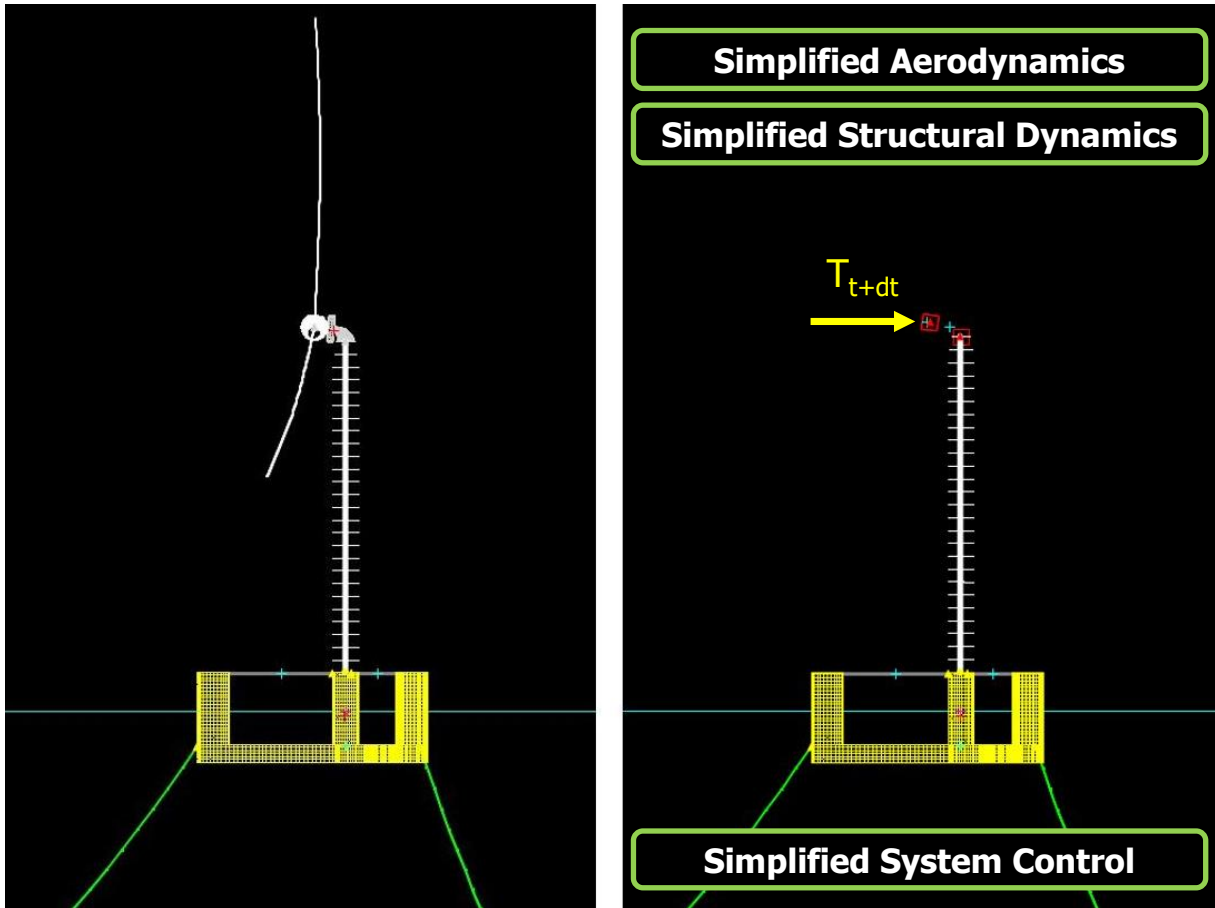
Figure 1: Scope and graphical representation of the simplified turbine model

LIST OF ABBREVIATIONS

ABL   Atmospheric Boundary Layer

BEM   Boundary Element Method

BEMT   Blade Element Momentum Theory

CFD   Computational Fluid Dynamics

DLCs   Design Load Cases

FEM   Finite Element Method

FOWT   Floating Offshore Wind Turbine

FVW   Free Vortex Wake method

GDW   Generalized Dynamic Wake method

HHTBL   Horizontally Homogeneous Turbulent Boundary Layer

LCOE   Levelized Cost of Energy

ME   Morison Equation

NREL   National Renewable Energy Laboratory

PF   Potential Flow

QS   Quasi-Static method

QTFs   Quadratic Transfer Functions

RB   Rigid Body

RAOs   Response Amplitude Operators

RNA   Rotor Nacelle Assembly

RPM   Rounds Per Minute

RWT   Reference Wind Turbine

SB   Spar Buoy

SSP   Semi-Submersible Platform

SWOT   Strength, Weaknesses, Opportunities and Threats

TLP   Tension-Leg Platform

TRL   Technology Readiness Level

TSR   Tip Speed Ratio

VS-VP   Variable-Speed, Variable-Pitch

1 INTRODUCTION

1.1 Offshore Wind

In the current context of volatile energy markets characterised by concerns over energy supply and the imperative to reduce greenhouse gas emissions, the electricity sector is undergoing a transition towards more sustainable and independent power generation. Expanding offshore wind energy represents a viable solution to address these challenges. The International Energy Agency (IEA) conducted an extensive analysis, as documented in their 2019 report [IEA19], revealing a global technical potential for offshore wind power generation that exceeds 420,000 TWh per year. This estimate surpasses the current global power demand by over 18 times, indicating the immense untapped potential of offshore wind resources. Despite being a relatively young technology, with more than 90% of the EU's capacity installed within the past decade, offshore wind projects are rapidly emerging worldwide. Europe, in particular, stands out as a key player in the sector, with targets to increase the North Sea offshore capacity to 76 GW by 2030 and 260 GW by 2050 ([Rab23]).

Offshore wind offers numerous benefits, as highlighted in [Ørs23]. Firstly, it is a renewable and clean energy source that reduces dependence on foreign fossil fuel supplies. In addition, offshore wind has distinct advantages over onshore wind. It minimises visual and acoustic pollution, which often poses acceptance issues for onshore wind parks. Moreover, the vast available space offshore does not interfere with other forms of land use. Furthermore, wind conditions at sea are more favourable for energy generation. Offshore wind experiences stronger, more consistent winds with less turbulence compared to onshore locations. This translates into higher and more reliable power generation. Offshore wind also facilitates the scalability of wind turbines. The transportation of larger towers and blades by ships enables the construction of bigger wind turbines, leading to increased power generation capacity. Another significant advantage is the proximity of many major cities and densely populated areas to the sea. This geographical advantage ensures that offshore wind energy sources are conveniently located close to the areas with high electricity demand, reducing transmission losses and improving energy availability.

1.2 Potential of Floating Offshore Wind Turbines

According to [Ørs22], realising the full potential of offshore wind energy requires the implementation of floating foundations for offshore wind turbines. This approach has the potential to

exploit up to 80% of the world's offshore wind resources by deploying turbines in deeper waters with more favourable wind conditions. Findings from [LKC18] indicate that a significant proportion of European seas (80%), US oceans (60%), and Japanese oceans (80%) have considerable depths exceeding 60 meters, making them unsuitable for bottom-fixed turbines. Figure 2 visually represents the prospective expansion of offshore wind energy to regions such as the Spanish Atlantic coast and the Mediterranean Sea through the deployment of floating offshore wind turbines (FOWTs).
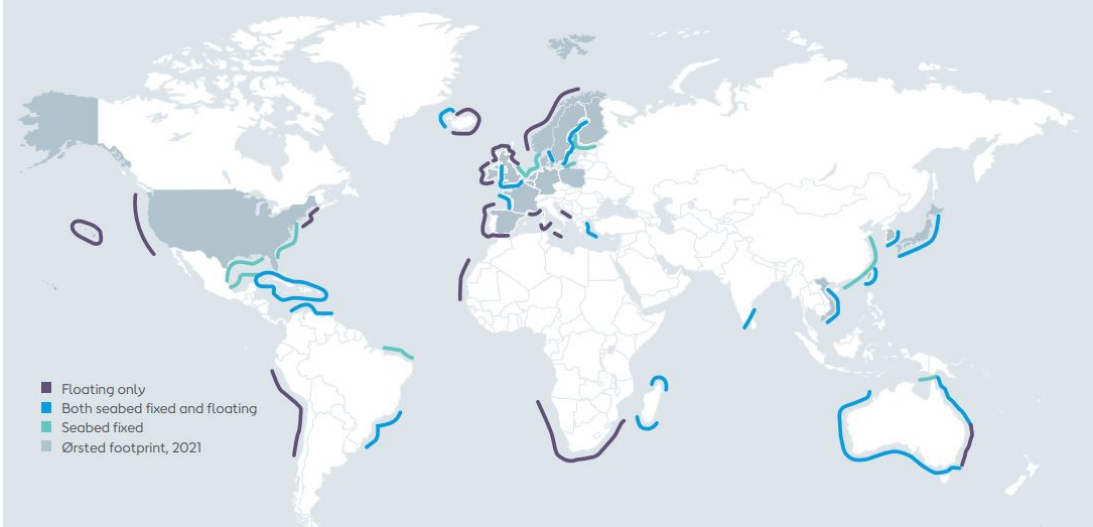
Figure 2: Sites suitable for bottom fixed and floating offshore wind turbines [Ørs22]

Equinor's Hywind projects serve as a notable example highlighting the potential of floating wind turbines. In 2009, Equinor launched the world's first floating wind turbine, the Hywind Demo, with a capacity of 2.3 MW. Subsequently, in 2017, they established the world's first floating wind farm, Hywind Scotland, consisting of five 6 MW turbines [Equ23a]. Completed in 2022, the Hywind Tampen project is now the world's largest floating wind farm, featuring 11 turbines with a capacity of 8 MW each [Equ23b]. The performance of Hywind Scotland underscores the superiority of floating wind turbines compared to their fixed-bottom counterparts by using the capacity factor, which is the ratio of the actual energy output to the maximum potential output. According to [Equ21], Hywind Scotland achieved the highest average capacity factor of any wind farm in the UK in each of the three years after its initial operation. Over this period, the average capacity factor was 54%, surpassing the average offshore wind capacity factor in the UK, which stands at around 40%.

[Ørs22] highlights the significant advancements made in the cost competitiveness of seabed-fixed offshore wind turbines over the past decade. Initially, this technology had a higher levelized

cost of energy (LCOE) compared to the average market rates, making it economically non-competitive. However, through standardisation, optimisation, and industrialisation, economies of scale have been achieved, resulting in a remarkable cost reduction of over 65%. According to [Equ21], a similar cost reduction trend is observed in the Hywind project, as illustrated in figure 3, showing the evolution and future predictions of the LCOE. From the Demo stage to Hywind Scotland, there was a 70% reduction in capital expenditure (CAPEX) per MW. Subsequently, the next stage, Hywind Tampen, witnessed a further 40% decrease.
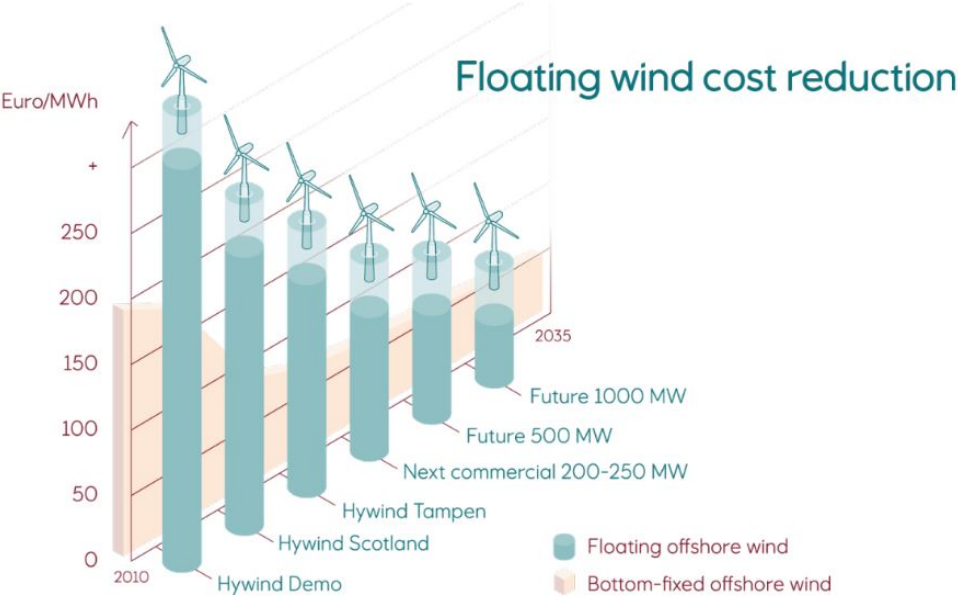
Figure 3: Levelized cost of energy for floating and bottom-fixed offshore wind turbines [Equ21]

According to [Equ21], despite the consistent cost improvements in floating offshore wind technology, Equinor predicts that this technology will only become economically competitive when wind farms larger than 500 MW are introduced. This perspective is supported by [Ørs22], which emphasises the importance of standardisation and supply chain investments to enable economies of scale and cost reduction in the industry. The study predicts that with these advancements, the technology could become cost-competitive by the early 2030s.

1.3 Challenges for Floating Offshore Wind

The growth of floating offshore wind technology is characterised by numerous challenges, which, according to [Goa23], are dominated by bottlenecks in the supply chain. As explained in [Rab23], infrastructure investments are essential for meeting governmental targets for the expansion of floating offshore wind. As mentioned in [LKC18] and illustrated in [Que23], there is a wide

range of available concepts, with over 40 prototypes currently in the market; a summary of which is provided in appendix C.1. The existence of numerous concepts and the uncertainty surrounding which technology will dominate in the coming years present a significant challenge for industry and shipyards. This uncertainty creates difficulty in determining the necessary preparations and investments required for future development, which would be so desperately needed according to [Ørs22].

To achieve the desired scale-up, choices need to be made about the type of floating foundations to target, so that decisions can be made about which facilities to invest in. In [Goa23] it is stated that besides the economic aspect, a fundamental factor that will strongly influence the selection of the foundation is its motion performance in relation to the environmental conditions. It will be of importance to compare the dynamics of different layouts and to perform optimisation in order to obtain the floater that is best adapted to the specific configuration. However, performing dynamic analyses poses major challenges. On one hand, according to [Far+22], simulations are complex and time-consuming due to the high complexity of the aero-hydro-servo-elastic model, which is discussed in the literature review in section 3. On the other hand, class society requires an important number of load cases to be investigated (see appendix C.4), making the process even more demanding in terms of time.

1.4 Objective and Structure of the Paper

Given the above-mentioned challenges posed by the time-intensive nature of the dynamic simulations, this study seeks possibilities to reduce computational time while retaining sufficient accuracy for comparison between distinct concepts and layouts. It is important to notice that the aim is not to develop the most accurate model, but one that allows for rapid and reasonably accurate outcomes.

The study starts with the selection of a specific floater type in section 2, grounded in a comprehensive literature review, which serves as a foundational point for the following analyses. Subsequently, section 3 conducts a literature review, exploring different methods for numerically modelling FOWTs, with special emphasis on design parameters influential to the chosen floating substructure. The study progresses with a software selection in section 4, followed by outlining the simulation procedure's structure in section 5. Delving into operational principles, control mechanisms, and dynamic effects encountered in wind turbines, section 6 lays the groundwork for constructing the simplified models. Section 7 deals with diverse model enhancements and

examines the significance of various modelling parameters on turbine dynamics. The main focus of the study is reached in section 8, where the primary goal of creating a simplified model with a significant reduction in computational time is realised. Finally, section 9 provides a summary of key findings and section 10 presents the main conclusions. Subsequently, section 11 suggests future avenues of research. Supporting the main content, three appendices provide theoretical background (appendix A), supplementary information reinforcing decisions (appendix B), and a database (appendix C).

In addition to its primary aim of developing a simplified model for computational efficiency, this research carries a secondary objective of yielding valuable insights for the technical department of Allseas, the offshore company at which the study is performed. The research enhances the company's understanding about floating wind in general, providing detailed explanations about the different concepts and exploring upcoming projects. Furthermore, investigations are performed into how the turbine's dynamics can be modelled, which theorems are used and which particularities are encountered. Moreover, detailed theoretical insights into various concepts are provided, particularly in appendix A, including discussions on topics like wind spectra or the *Blade Element Momentum Theory*. Additionally, exploration extends to the integration of external *Python* functions within *OrcaFlex* software, as well as developing strategies for the automation of both, simulations and analyses.

2 CHOICE OF FLOATER TYPE

2.1 Introduction

In order to streamline the study, it is necessary to select a specific floater type among the various concepts available. This selection process involves a detailed explanation of the different concepts and a comprehensive literature review to determine the most promising floater for future development. The chosen substructure will then serve as the basis for the subsequent analysis of modelling parameters and model simplifications.

2.2 The Different Concepts

Floating support structures for offshore wind turbines can be classified based on their primary mechanism for achieving static stability, as outlined in [LKC18]. These include ballast stabilised, waterplane (or buoyancy) stabilised, and mooring stabilised mechanisms. Ballast stabilised concepts utilise a large weight located deep within the floating system to lower the centre of gravity below the centre of buoyancy, creating a stabilising righting moment that counters rotational displacements. In contrast, waterplane stabilised concepts utilise the waterplane's shape and geometry to achieve stability by generating a substantial second moment of area. On the other hand, mooring stabilised concepts rely on high-tensioned mooring lines to generate the restoring moment, stabilising the platform and preventing excessive rotation.

According to [Día+22], both ballast and waterplane stabilised concepts typically employ catenary mooring lines, which utilise their significant weight to keep the floaters in position. The catenary shape of the lines, combined with their inherent flexibility, enables them to effectively absorb dynamic loads and movements, providing elasticity and reducing the stress exerted on the moored object. Furthermore, the flexibility of the lines allows them to accommodate fluctuations in water level and tidal variations without excessive tension.

In addition, [LKC18] highlights that floating support structures are not limited to steel-based concepts only. Concrete-based designs and steel-concrete hybrid structures are also viable options commonly seen in the industry. The utilisation of concrete enables an increase in the amount of local content, enhancing flexibility and typically reducing material cost. Nonetheless, it's important to bear in mind that concrete structures tend to be heavier, which leads to challenges during manufacturing and transportation.

2.2.1 The Spar Concept

Representing the purest form of a ballast stabilised concept, the typical design of a spar consists of a long cylindrical structure weighted at its bottom. The deep ballast creates a substantial righting moment and provides significant inertial resistance against pitch and roll motions, as detailed in [LKC18]. Figure 4 illustrates the typical layout of such a spar, highlighting its immense draft. According to [Eld17], even the relatively small 6MW turbines employed in the Hywind Scotland project are placed on spar floaters with a draft of approximately 80 meters. For next-generation turbines, [BKS15] indicates that drafts are expected to exceed 120 meters.
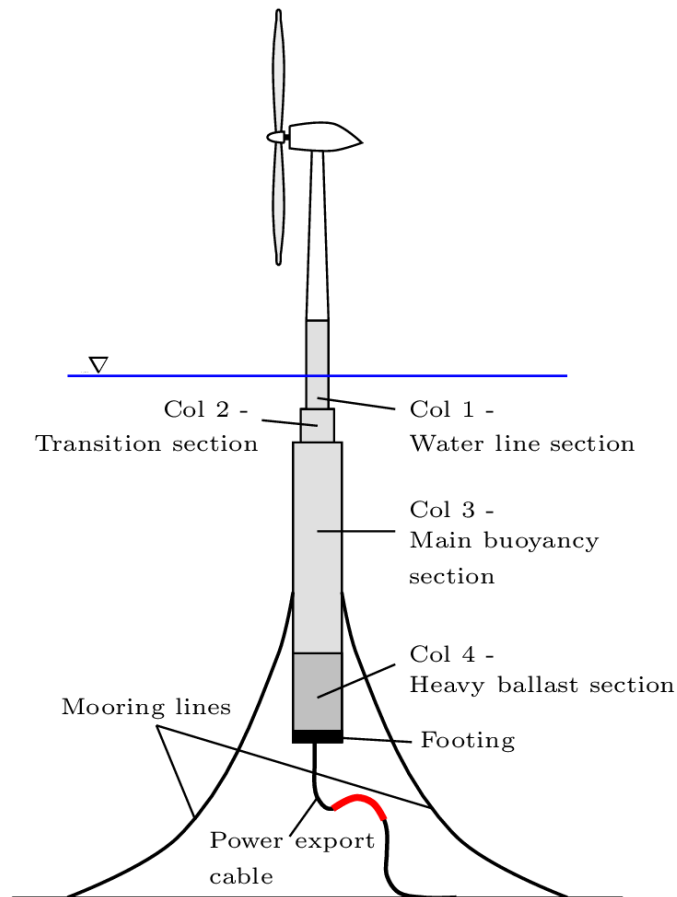
Figure 4: Typical layout of a spar-type FOWT [BF11]

According to [BKS15], the main strength of the spar technology lies in the simple physical principles on which it relies, expressing through its easy geometry and inherent stability. The high *Technology Readiness Level* (TRL), shown by the existence of already operating wind farms and techniques such as horizontal transport, indicates the concept's maturity. Moreover, there exist more advanced technological options such as the addition of stabilising fins or mooring lines with delta connections, which allow for further development of this technology. In [BKS15], it

is demonstrated that under identical environmental conditions, the motion of a turbine mounted on a semi-submersible floater surpasses that of a spar-type floater, indicating the spar's superior dynamic performance.

There are, however, significant disadvantages associated with this technology. Due to the greater draft and the requirement for sufficient clearance between keel and seabed, the spar-type floater is only suitable for deeper water. Moreover, as highlighted in [Día+22], relatively sheltered deep waters and heavy lift vessels are needed to erect the substructure and install the turbines, which not only leads to further environmental requirements but also has a significant impact on costs. Data presented in figures 72, 73, and 74 in appendix C.1 reveals that the spar technology is not favoured for upcoming projects, partly attributed to its unsuitability for many sites due to its requirements on water depth. Additionally, [Día+22] underscores the existence of numerous challenges associated with logistics in both manufacturing and installation.

Table 1: Summary and SWOT analysis for the spar concept ([Día+22], [LKC18], [BKS15])

Strengths	Weaknesses
• Inherent stability • Suitable for high sea states (Tendency for lower critical wave-induced motions) • Simple geometry and design • Cheap and simple mooring and anchoring • Low operational risk • Little susceptible to corrosion • Simple structure; easy manufacturing and maintenance	• Unsuitable for shallow water • Challenging, time-consuming and costly float-out and installation • Offshore operations require heavy-lift vessels and currently can be done only in relatively sheltered, deep water • Large seabed footprint • Long mooring lines (costs) • Long and heavy structure (costs)
Opportunities	Threats
• High TRL • Horizontal transportation • Delta-connection for yaw stabilisation • Stabilising fins for sway and heave movements • Serial fabrication; synergies with tower manufacturing	• Logistical challenges in the domain of production and installation • No global market

2.2.2 The Semi-Submersible Concept

As stated in [Ibe23], semi-submersible floaters are composed of vertical cylinders interconnected by beams and braces. As stability primarily relies on the waterplane area of those cylinders, their size and spacing play a crucial role. According to [BKS15], the most prevalent layout consists of three columns positioned at the corners of a triangular arrangement. The wind turbine

can be mounted either on one of these columns or be supported by a fourth column located at the centre of the triangle, the first option being used for the 'WindFloat' concept illustrated in figure 5 below. This design is employed in both, the 25MW wind park situated off the coast of Portugal and the 50MW wind park off Scotland, as described in [Ene21].

Figure 5: Configuration of the semi-submersible floater used in the 'WindFloat' design [Ene21]

As detailed in [LKC18], the semi-submersible floater offers several advantages that contribute to its popularity in offshore wind projects. Firstly, its float-out and installation procedures are relatively simple and cost-effective. Additionally, its depth independence allows for deployment in a wide range of water depths, from 40 to 400 meters, making it a versatile technology. The shallow draft of the floater provides flexibility for manufacturing and turbine installation, as the entire system can be assembled in a harbour or dry dock and then towed to its final location. One of the key factors driving its widespread adoption is its cost efficiency, as demonstrated in [Mai+20] and [Cas+20]. Both studies reach the same conclusion that the semi-submersible floater has the lowest lifecycle cost within the range of concepts. Combined with the high compatibility for any specific water depth, this has made this technology the favourite for upcoming projects all around the world, as demonstrated in [Día+22] and shown in appendix C.1. The research presented in [LKC18] highlights ongoing advancements in the field, such as modified

geometries for wave cancellation and stabilising active ballast systems. These advancements aim to address some of its disadvantages, such as its lower stability and tendency to have higher critical wave-induced motions, as specified in [BKS15]. The technology's high TRL and the existence of operational offshore wind farms demonstrate its feasibility and progress. While it is acknowledged that the semi-submersible floater is larger and more complex compared to other concepts, resulting in relatively high manufacturing costs, its overall cost remains lower than alternative types, as mentioned in [LKC18].

Table 2: Summary and SWOT analysis for the semi-submersible concept ([Día+22], [LKC18], [BKS15])

Strengths	Weaknesses
• Broad weather window for float-out and installation • Depth independence • Cheap and simple mooring and anchoring system • Low overall risk • Onshore or dry dock assembly and transport to site using conventional tugs • Full system transportation • Simple installation and decommissioning	• Lower stability, higher motions (Tendency for higher critical wave-induced motions) • Large seabed footprint • Long mooring lines (costs) • Subject to corrosion and ice-loads • Large and complex structure; challenging manufacturing and maintenance • Large and heavy structure; higher material use • Larger impact on turbine due to motions
Opportunities	**Threats**
• High TRL • Heave plates for reducing heave response • Large global market • Several turbines on one foundation • Cost reduction through mass production and braceless design • Geometry for wave-cancellation • Stabilising active ballast system	• Internal forces dependent on geometries (large internal forces if geometry designed for wave-cancellation) • Expensive (active) ballast system • High competition between developers

2.2.3 The Barge Concept

A barge floater, similar to a semi-submersible one, is a waterplane stabilised structure. According to [LKC18], the primary distinction between these concepts lies in their configuration. While a semi-submersible features distributed buoyancy and consists of columns, a barge is typically flat in shape and consists of a single buoyancy volume. As mentioned in [Ibe23], the dimensions of a barge floating substructure are similar to those of a ship, with the width and length being significantly larger than the draft. This can be observed in figure 6, showing Ideol's 'Damping Pool' design. To mitigate excessive movements, barge platforms often incorporate heave plates, which are horizontal plates positioned below the waterline, enhancing both added mass

and viscous damping. According to [BKS15], due to its shallow draft, its stability is almost completely reliant on the waterplane's restoring moment, making it particularly sensitive to the natural frequencies of the waves.

Figure 6: The Floatgen project using BW Ideol's 'Damping Pool' floating foundation [Ide23]

According to [LKC18], the barge floater shares similar advantages with the semi-submersible concept. One advantage is the possible onshore assembly of the turbine, followed by a tow-out to the deployment site. This approach offers flexibility and cost-effective load-out and installation operations. Additionally, the barge is suitable for similar water depths as the semi-submersible. However, compared to the semi-submersible, the barge exhibits significant drawbacks, as highlighted in [BKS15]. One major disadvantage is its natural periods generally being closer to the wave periods, which can lead to important wave-induced motions. Furthermore, as specified in [Día+22], the TRL of the barge is relatively low, and there are currently no operational wind farms employing this technology. Only prototypes of barge floaters have been realised so far. To date, the utilisation of the barge in future projects has been decided for one project only, as evidenced in appendix C.1. This restricted dedication for the concept diminishes the prospects for the development of mass-production techniques and cost reductions through the implementation of learning curves and standardisation processes.

Table 3: Summary and SWOT analysis for the barge concept ([Día+22], [LKC18])

Strengths	Weaknesses
• Easy geometry and low-cost production • Depth independence • Cheap and simple mooring and anchoring system • Full system easy transportation • Simple installation and decommissioning • Onshore or dry dock assembly and transport to site using conventional tugs	• Lower stability, higher motions (Tendency for higher critical wave-induced motions) • Large seabed footprint • Long mooring lines (costs) • Large and heavy structure, uses more material • Natural periods close to the wave period • Larger impact on turbine due to motions
Opportunities	Threats
• Innovative designs to change natural periods	• Low TRL • No global market position

2.2.4 The Tension-Leg Platform Concept

As described in [Str16], the TLP concept employs tensioned tendons to secure the floaters in place, which are typically composed of metallic or synthetic wires and are connected to the seabed using gravity- or suction-based anchors or steel-driven piles. In contrast to semi-submersible systems with interconnected columns, TLPs feature a single central stilt and three to six submerged arms to which the tendons are attached. In the event of a heel condition, the weight of the structure, combined with the tension in the tendons, generates a righting moment to ensure stability. Moreover, the structure is designed to mitigate roll, pitch, and heave moments acting on the system, resulting in reduced dynamic loads on the turbine, decreased wave resonance, and minimised sway and yaw motions. Additionally, the vertical oscillation of the cable is significantly reduced. Figure 7 shows the layout of Iberdrola's 'TLPWind' concept.

As specified in [LKC18], the main advantage of the TLP is its high stability and low movement, combined with the lower manufacturing and load-out expenses, attributed to the relatively simple, compact, and light nature of the structure. In some TLP concepts, the tension in the mooring lines is designed to submerge the platform, resulting in reduced wave sensitivity and lower susceptibility to corrosion. Furthermore, much shorter mooring lines are required, reducing costs. In addition, this type of mooring drastically reduces the seabed footprint compared to a catenary mooring configuration. As discussed in [Día+22], the TLP design is particularly suitable for intermediate water depths, typically up to 100 meters, making it a favourable choice for the moderate depths commonly found in the northern European seas. Although the use in much greater water depths is possible, as has been shown repeatedly in the oil and gas industry, economic viability becomes a constraint. Consequently, TLPs may not be a viable option for numerous
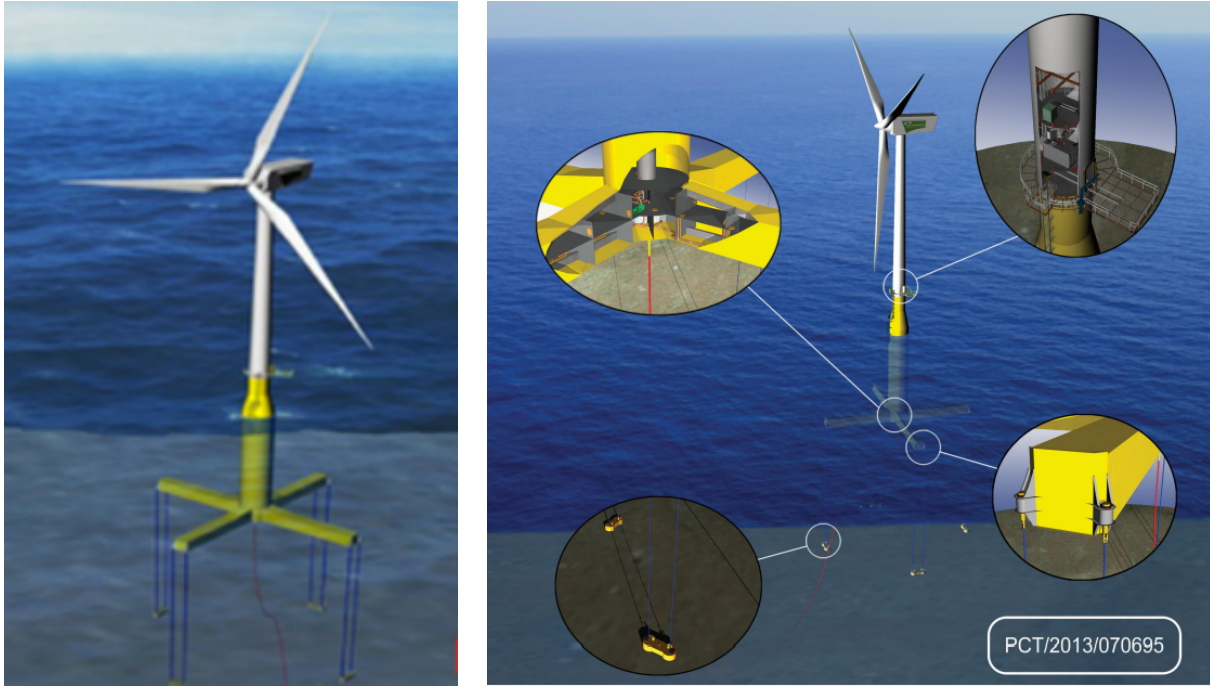
Figure 7: The tension-leg concept 'TLPWind' by Iberdrola [Reo22]

offshore sites with deeper waters.

The main disadvantage of the TLP concept is its high cost. Both, [Mai+20] and [Cas+20] conclude that the semi-submersible floater has the highest lifecycle cost within the range of concepts. According to [LKC18], this is partly due to the complex and costly installation of the mooring and anchoring system, requiring expensive equipment and vessels. Furthermore, the platform is not inherently stable, causing significant difficulties during the transport and installation phase. Additional installation barges or temporary reusable floats attached to the platform are required to tow it to the deployment site, further increasing the costs. In addition, although this type of foundation needs comparatively less material for construction, it requires a much higher quality of steel than the other concepts, significantly increasing material costs. Furthermore, the anchoring and mooring makes the system unsuitable for difficult soil conditions, and the lack of inherent stability leads to a great risk in the event of a tender or anchor failure. To reduce this risk, redundant moorings would be required, further increasing the cost of the system. Another disadvantage is the relatively low TRL of the system, as evidenced by the absence of operational wind farms. Additionally, as pointed out in [Día+22], there is just one upcoming project that plans to utilise TLPs for a wind farm.

Table 4: Summary and SWOT analysis for the TLP concept ([Día+22], [LKC18])

Strengths	Weaknesses
• Excellent stability, low motions • Simple, small and light structure, easy maintenance • Onshore or dry dock assembly • Little wave sensitivity (in case of submerged platform) • Suitable for even high sea states (in case of submerged platform) • Small seabed footprint • Suitable for intermediate depths • Relatively short mooring lines • Little susceptible to corrosion (in case of submerged platform)	• Hard to keep stable during transport and installation • Unsuitable for challenging soil conditions • Complex and costly installation of mooring and anchoring system • High risk if tender or anchor fails • Complex and risky installation (as well as disconnection for onshore maintenance) • Large stresses in structure • Economically unsuitable for deep waters • Special purpose installation ships required • Unsuitable for strong tidal currents or storm surges
Opportunities	Threats
• Redundant moorings reduce risk • Less soil dependent gravity anchors • Low competition	• Low TRLs • High cost of redundant mooring • No global market positions • Some uncertainty about impact of possible high-frequency dynamic effects on turbine

2.2.5 Hybrid Concepts and Stability Triangle

As discussed earlier in this section, floaters can be classified based on their primary mechanism for achieving static stability: ballast stabilisation, waterplane stabilisation, or mooring stabilisation. However, many floaters employ a combination of these mechanisms, as outlined in [LKC18]. Figure 8 illustrates the stability triangle, which includes different floater layouts and their corresponding stabilisation mechanisms. Floaters located at the corners of the triangle rely solely on a single mechanism, while hybrid concepts can be found in the intermediate regions. The combination of mechanisms allows for the integration of advantages from different systems, tailoring the floating structure to specific criteria. One example of a hybrid floater is the Gicon concept, which functions as a waterplane-stabilised semi-submersible during the transport phase. It achieves righting moment through a large second moment of area, enabling onshore assembly and towage to the deployment site. Once on site, the gravity anchor is lowered to the seafloor and weighted, and the mooring lines are tensioned by ballasting and deballasting the floater. During operation, the Gicon structure benefits from the excellent stability of a TLP. However, as mentioned in [Día+22], these hybrid structures inherit not only the benefits but also the disadvantages of the different concepts. For instance, the Gicon floater has a higher weight compared

to a TLP due to its semi-submersible layout. Additionally, it experiences higher stresses and requires higher grade steel due to the tensioned mooring lines.
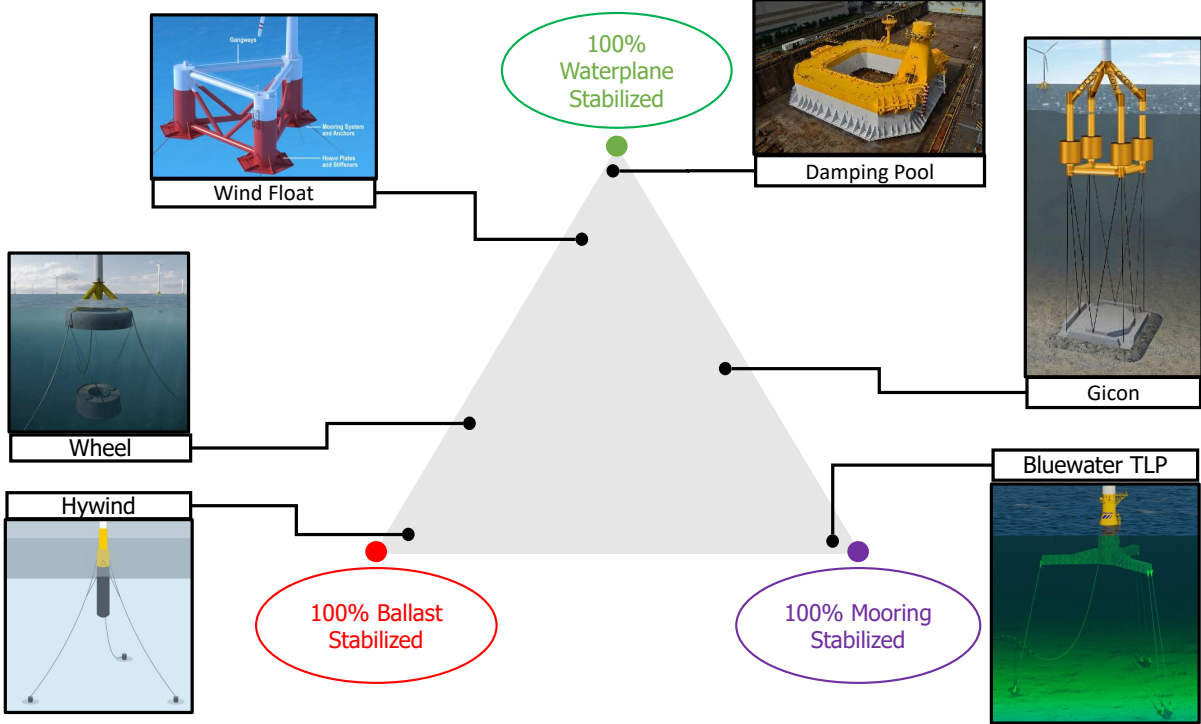
Figure 8: The stability triangle with different floater layouts

2.3 Qualitative Comparison

To facilitate comparison between SSP, spar and TLP, table 5 provides an overview of key decision drivers and evaluates the performance of each floater type in respective domains.

The turbine weight of spar foundations and semi-submersible platforms is compared in more detail. Based on information from [Equ17], the spar foundations supporting 6MW wind turbines in the Hywind Scotland wind farm have a steel weight of 2300 tonnes, resulting in a weight-to-capacity ratio of 383 tonnes/MW. In contrast, as mentioned in [Off21], the semi-submersible platforms utilised at the Kincardine wind farm in Scotland accommodate 9.5MW wind turbines and have a steel weight of approximately 3000 tonnes each, resulting in a weight-to-capacity ratio of 315 tonnes/MW. Assuming that weight per capacity can be compared, it is observed that the semi-submersible platform exhibits a lighter weight in comparison to the spar foundation. Further analysis on floater manufacturing reveals that the semi-submersible type demonstrates lower manufacturing costs compared to the spar concepts, which can partly be attributed to its lower weight, as discussed above. In addition, according to [Pri22], the semi-submersible

structure can be manufactured in a modular manner by dividing it into columns, truss elements, and damping plates. This modular design, coupled with the relatively low assembly requirements, allows for individual modules to be manufactured separately. This approach enhances cost-efficiency and offers a high degree of flexibility in the manufacturing process.

Table 5: Qualitative comparison between SSP, Spar and TLP

DECISION DRIVERS	SSP	Spar	TLP	Impact
Structure				
Horizontal Dimensions [Mai+20]	High	Small	Medium	$(-)$
Steel Weight [Día+22]	Medium	High	Low	$(-)$
Draft [LKC18]	Low	High	Low	$(-)$
Complexity [LKC18]	High	Low	Medium	$(-)$
Stresses in Structure [LKC18]	Low	Low	High	$(-)$
Performance				
Stability [LKC18]	Low	Medium	High	$(+)$
Seakeeping [LKC18]	Low	Medium	High	$(+)$
Risk [LKC18]	Low	Low	High	$(-)$
Seabed Footprint [LKC18]	High	High	Low	$(-)$
Complexity of Operations				
Floater Manufacturing [LKC18]	Medium	Low	Medium	$(-)$
Turbine Installation [Mai+20]	Low	Medium	High	$(-)$
Anchor Installation [LKC18]	Low	Low	High	$(-)$
Investment Cost				
Mooring Lines [LKC18]	High	High	Low	$(-)$
Anchors [Mai+20]	Low	Low	High	$(-)$
Floating Platform [Mai+20]	Medium	High	Medium	$(-)$
Operational Cost				
Mooring and Anchoring [Mai+20]	Low	Low	High	$(-)$
Float-Out and Installation [Mai+20]	Low	Medium	High	$(-)$
Technology				
Technology Readiness Level [LKC18]	High	High	Low	$(+)$
Global Market Opportunity [LKC18]	High	Low	Low	$(+)$

2.4   Conclusion - Choice of the Semi-Submersible Floater Concept

Based on the comprehensive literature review and detailed analysis of the strengths and weaknesses of different floating systems, the semi-submersible platform emerges as the preferred choice for this study, due to its significant potential in the coming years. The selection of the semi-submersible platform is supported by several factors. Firstly, it demonstrates low life cycle costs, as evidenced in studies such as [Mai+20] and [Cas+20]. Secondly, it offers simple and cost-effective float-out and installation procedures, which is evidenced in [Mai+20]. Additionally, the semi-submersible platform proves to be suitable for a wide range of water depths, as highlighted in [LKC18]. Deployment is feasible in water depths ranging from 40 to 400 meters. Moreover, the prominence of the semi-submersible platform in future projects is evident, as demonstrated in [Día+22], which showcases its superiority in the European, American, and Asian markets. Coupling this growing prominence with insights from [Equ21], which reveal that greater experience and larger project scales will naturally drive standardisation and trigger a learning curve, it becomes apparent that further cost reductions in semi-submersible floater technology can be anticipated. Although there is a tendency towards higher critical wave-induced motions, as indicated in [BKS15], it is important to note that ongoing technical advancements, such as wave cancellation geometries and stabilising active ballast systems, are being developed to mitigate these drawbacks, as highlighted in [LKC18]. These advancements are expected to reduce the severity of the mentioned limitations and enhance the performance of the semi-submersible platform.

3   LITERATURE REVIEW

3.1   Introduction

A literature review is conducted to investigate the appropriate methods for the numerical modelling of semi-submersible floating offshore wind turbines. The review starts with an examination of the floater's design parameters to gain insight into its geometric properties and their impact on system dynamics. Additionally, an overview of the available modelling software and techniques is provided, giving insights into the current state of the art.

3.2   Design Parameters

In article [Zho+21], an assessment is conducted to evaluate the impact of floater dimensions on manufacturing cost, structural characteristics, and hydrodynamics. Within the selected design space, which corresponds to a four-column semi-submersible FOWT, the study illustrates that first-order hydrodynamics are mainly reliant on three platform parameters: draft, column radius, and column spacing. These parameters play a significant role in determining the mass, hydrostatic stiffness, and wave excitation loads for the platform. More specifically, the study demonstrates that column spacing has the most significant impact on first-order horizontal platform motion, particularly in the surge degree of freedom. This phenomenon occurs because changes in column spacing affect their interaction within the wave field and lead to significant variations in hydrodynamic loads. Additionally, [Zho+21] illustrates that draft plays a crucial role in the pitch degree of freedom. A greater draft results in increased moment of inertia, added mass, and hydrostatic stiffness, which improves the floater's stability. However, it is noteworthy that increasing the draft generally results in larger hulls, which can lead to greater wave excitation loads. Overall, increasing the platform draft can help to mitigate the first-order pitch motion. Concerning column radius, it is found that an increase in size is generally accompanied by an increase in platform and nacelle motion. Consequently, limiting the column radius not only can lead to cost reduction, but also to improved hydrodynamic performances. Further investigation reveals that certain mooring parameters, such as chain diameter and weight, have a substantial impact on the surge natural frequency. However, the pitch natural frequency is relatively insensitive to these mooring parameters.

The significance of mitigating out-of-phase surge and pitch responses is underscored by insights from [Lem+20]. Through the adjustment of both hull shape and turbine controller, the reduc-

tion of these influences contributes to diminished fore-aft motions at the hub. These findings are supported by results in [Zho+21], which reveal that deep-draft platforms tend to exhibit in-phase surge and pitch responses to waves, resulting in considerable motions at the tower top. In contrast, platforms with shallow draft tend to experience reduced wave-induced fore-aft motion at hub height, attributed to the counter-phase surge and pitch impacts they encounter. Furthermore, both articles [Lem+20] and [Zho+21] highlight the significance of the control system in the dynamics of floating wind turbines. It is found that while the controller cannot mitigate the first-order wave loads, it can potentially enhance the low-frequency response behaviour of the structure, thereby greatly impacting its overall dynamics.

3.3 Numerical Modelling Approaches

This subsection aims to acquire comprehensive knowledge regarding the various numerical tools, optimisation techniques, and modelling approaches that can be applied for FOWT design. As per [Far+22], the design procedure for the floating support structures is categorised into three stages, namely conceptual, basic, and detailed design, as depicted in figure 9. The conceptual design utilises dimensioning along with a frequency domain analysis to assess the layout's efficiency. At this stage, the wind turbine is considered a rigid body and system complexity is largely simplified. The basic design involves fully-coupled time-domain simulations, where the system's details are further specified. Numerical modelling is the central focus during these first two stages; however, experimental validation becomes essential during detailed design to assess the reliability of the theoretical model.
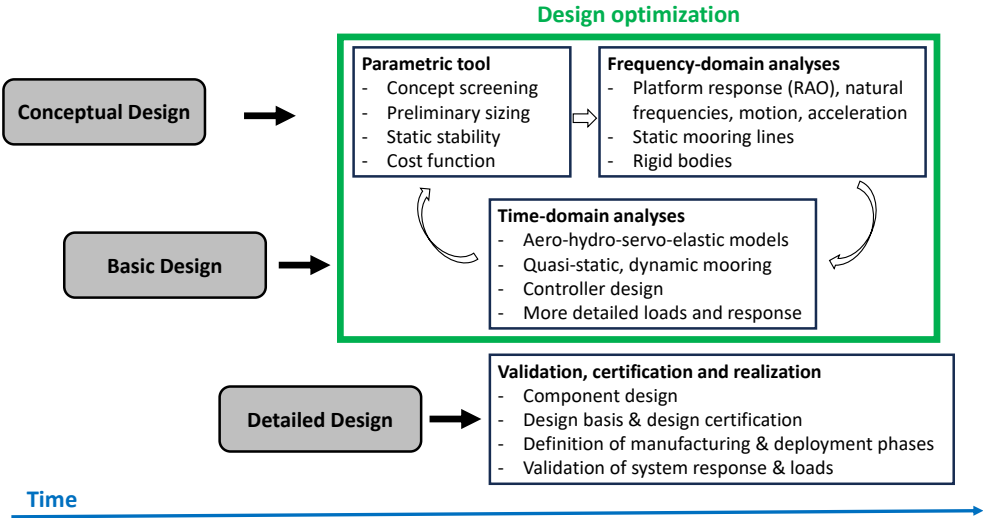
Figure 9: Design stages for support structures of floating offshore wind turbines [Far+22]

In the optimisation process of conceptual design, the frequency-domain approach is preferred over time-domain analyses, owing to its faster computational speed. Nevertheless, [Ott+21] specifies that detailed estimates of the system response, which are affected by the interdependence between aerodynamics, hydrodynamics, structural dynamics, and system control, are better provided by extensive time-domain simulations, despite being computationally expensive. According to [Far+22], frequency-domain analyses are insufficient in capturing nonlinear dynamics that significantly impact the device's response. Consequently, time-domain simulations are indispensable for the basic design stage.
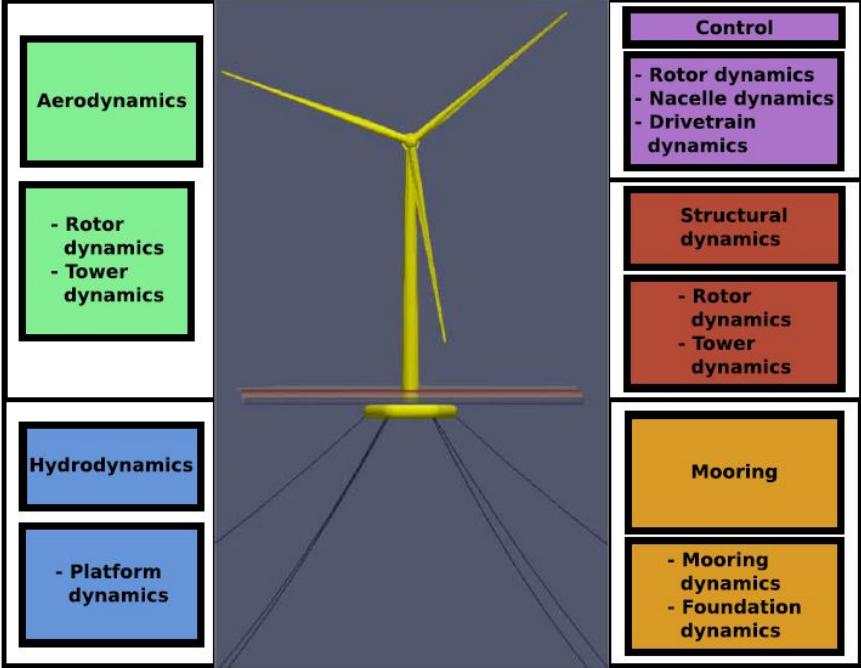
Figure 10: Main modelling sections and their influence on FOWT components [Far+22]

Figure 10 facilitates comprehension regarding the intricate nature of the numeric modelling of FOWTs and assists in identifying the components that necessitate inclusion. The numerical modelling of a FOWT is significantly more complicated than that of a bottom-fixed or on-shore wind turbine, primarily due to the complex interplay among various domains. Both references, [Far+22] and [Ott+21], emphasise the importance of incorporating a model for system control into the overall model due to the substantial influence of blade pitch and rotor speed control on the global dynamics of the system. Moreover, [Far+22] asserts that accurate modelling must incorporate the structural response of key components, namely the rotor and tower. Their flexible behaviour can be critical, particularly when excitation frequencies approach the lower natural frequency of the structure.

A range of modelling techniques exists, each offering a different level of accuracy, making them suitable for distinct phases of the design process depicted in figure 9. Figure 11 gives an overview over the main modelling techniques, used for the different domains illustrated in figure 10. The selection of an appropriate model at each stage of the design process is essential to achieve optimal design outcomes and meaningful results.
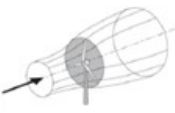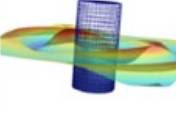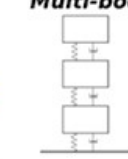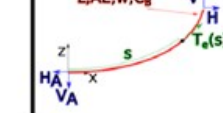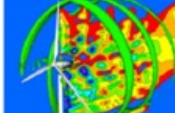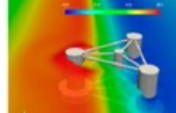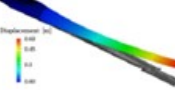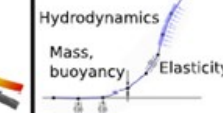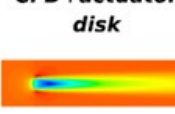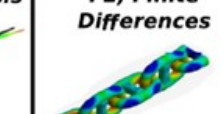
Aerodynamics	Hydrodynamics	Structural dynamics	Mooring	Control
BEM	Morrison equation $F_{me} = \rho V \dot{v} + \rho V C_a (\dot{v} - \ddot{X}) + \frac{C_d \rho A_d}{2}(v - \dot{X})\|v - \dot{X}\|$	Stiffness matrix $\epsilon = B_L q_e$ $K_{eL} = \int B_L^T E B_L dV$	Stiffness matrix $\begin{bmatrix} \frac{F}{L} & \frac{F}{rad} \\ \frac{FL}{L} & \frac{FL}{rad} \end{bmatrix}$	Torque control $\tau = K \cdot \omega^2$ $K = 0.5 \rho \pi R^5 \frac{C_{p,opt}}{\lambda_{opt}^3}$
Free wake vortex	Potential flow	Multi-body	Quasi-static	Pitch control $\Delta\theta(s) = (K_P + \frac{K_I}{s} + \frac{K_D \cdot s}{s \cdot \tau + 1})\Delta\omega$
CFD	CFD	FE	Lumped mass	Yaw control
CFD+actuator disk		Modal analysis	FE, Finite Differences	Advanced control models • Linear quadratic regulator (LQR) • Feed-forward • Model Predictive Control (MPC) • ...

Figure 11: Existing modelling techniques for different parts of FOWTs [Far+22]

Appendix C.2, containing figures 75 and 76, offers a comprehensive overview of the primary numerical tools employed for the modelling of floating offshore wind turbines. As detailed in [Ott+21], a comparative framework categorises the computational methods into distinct fidelity levels. Low-fidelity models are commonly applied during the conceptual design phase, while mid- and high-fidelity models find their utility in the basic and detailed design stages, respectively. Figure 12 briefly summarises these computational methods and their associated fidelity levels. Additionally, figure 13 shows the prevalent mid-fidelity software, known as engineering tools, utilised for comprehensive global dynamics analysis under both linear and nonlinear loads. Since the focus of this research is on developing a simplified model for the basic design stage, the selection of an appropriate engineering tool will be of importance in section 4.

Acronym	Category	Fidelity
BEM: Boundary Element Method	Hydrodynamic	Mid
BEMT: Blade Element Momentum Theory	Aerodynamic	Mid
CFD: Computational Fluid Dynamics	Aero-/hydrodynamic	High
Dyn: Dynamic method	Structural	Mid
FEM: Finite Element Method	Structural	High
FVW: Free Vortex Wake method	Aerodynamic	Mid
GDW: Generalized Dynamic Wake method	Aerodynamic	Mid
ME: Morison Equation	Hydrodynamic	Mid
PF: Potential Flow	Aero-/hydrodynamic	Mid
QS: Quasi-Static method	Structural	Low

Figure 12: Fidelity level of various computational methods [Ott+21]

Software	Hydrodynamics	Aerodynamics	Structure
FAST	PF + ME	BEMT + GDW/FVW	RB + Modal/FEM + Dyn/QS
HAWC2	PF + ME	BEMT + GDW	FEM + Dyn
SIMA	PF + ME	BEMT	FEM + Dyn
Bladed	With SIMA	BEMT + GDW	Modal
SIMPACK	With HydroDyn	AeroDyn/AeroModule	FEM
Orcaflex	PF + ME	With FAST	RB + FEM + Dyn
Flexcom	PF + ME	With FAST	RB + FEM + Dyn

Figure 13: Engineering tools used for basic design FOWT modelling [Ott+21]

3.4 Summary - Modelling of FOWTs

The literature review provides valuable insights into dynamic analyses of FOWTs and highlights crucial factors for consideration. Design of these offshore structures begins with the conceptual stage, focusing on the hydrodynamic response of the floating substructure, which, for semi-submersible floaters, is primarily influenced by three factors: floater draft, column radius, and column spacing. Owing to its high computational speed, this phase involves a frequency domain analysis utilising low-fidelity software. This analysis excludes the consideration of aerodynamics, mooring line dynamics, structural dynamics, and the turbine's control system, as well as their complex interactions. The hydrodynamic properties obtained from the conceptual design stage are subsequently utilised for basic design, where a time-domain dynamic analysis is performed. Employing mid-fidelity engineering tools, the complex interplay between different domains is studied, adding to the hydrodynamics the domains of aerodynamics and structural dynamics. Furthermore, the control system is included in the analysis, whose influence on the system dynamics is perceived as tremendous.

4 SOFTWARE SELECTION

4.1 Introduction

The literature review in section 3 reveals that the dynamic analysis of FOWTs involves two essential steps. The first step, the conceptual stage, focuses on the floater's hydrodynamics, excluding aerodynamics, mooring lines, structural dynamics, and the turbine's control system, along with their complex interactions. This stage utilises frequency-domain diffraction and radiation software. The second step involves a time-domain dynamic analysis, enabling the comprehensive assessment of the complex behaviour of the aero-hydro-servo-elastic structure, as illustrated in figure 10. This section provides insights into the selection of software for both stages and the theoretical concepts behind them. This section provides insights into the selection of software for both stages, as well as the theoretical concepts behind them.

4.2 Diffraction and Radiation Software

OrcaWave is selected based on its widespread use and accessibility at Allseas, as well as its compatibility with the *OrcaFlex* software, which is utilised for the dynamic analyses in this study. As by [Orc23d], *OrcaWave* is a diffraction and radiation software that uses potential flow theory to calculate the loading and response of wet bodies subjected to surface water waves.

4.2.1 Underlying Equations

The software assumes that the fluid flow is incompressible, inviscid, and irrotational and while the fluid velocity is given by $\nabla\Phi$, the velocity potential, Φ, is supposed to satisfy Laplace's equation in the fluid domain:

$$\nabla^2\Phi(\boldsymbol{X}, t) = 0 . \tag{1}$$

By substituting into the Navier-Stokes equation and integrating, the Bernoulli equation for the pressure is obtained, which is used by the software to calculate forces:

$$p(\boldsymbol{X}, t) = -\rho \left(\frac{\partial\Phi}{\partial t} + \frac{1}{2}(\nabla\Phi)^2 + gZ \right) . \tag{2}$$

The governing equations for fluid-structure interaction can be obtained by applying the boundary equations at the seabed, rigid bodies, and free surface, and taking into account the radiation

23

of waves generated by the presence of moving bodies. These equations cannot be solved analytically due to the nonlinear boundary conditions on the free surface and moving body surfaces. According to [Orc23d], to avoid the use of computational fluid dynamics, *OrcaWave* linearises its governing equations obtaining a general boundary value problem that is solved using Green's theorem. By solving this first-order problem for the velocity potential, *Response Amplitude Operators* (RAOs) and added mass and damping coefficients are obtained. Further expansion to second order leads to *Quadratic Transfer Functions* (QTFs).

4.2.2 Simulation Setup and Outputs

To conduct the diffraction and radiation analysis, a mesh file is imported into *OrcaWave* that defines the geometry of the structure. Additionally, it is necessary to define the inertial properties, as well as the wave periods and headings for which the analysis should be performed. The results obtained from this software encompass various parameters and are defined for each wave period and heading. These include the added mass and damping matrices, as well as load and displacement RAOs and wave drift QTFs. For the reference wind turbine specified in section 6.3, the diffraction analysis is conducted for wave periods ranging from 0 to 600 seconds, considering a total of 9 wave headings spanning from 0 to 180 degrees. The obtained results serve as input for the dynamic analysis software and define the hydrodynamic aspect of the structure.

4.3 Time-Domain Dynamic Analysis Software

The selection of *OrcaFlex* software for this research is based on its established reputation as a dependable and efficient tool for modelling FOWTs, as reported in [Far+22]. This choice is furthermore supported by the extensive validation reports, not only for the floater and mooring lines, but specifically for the integrated turbine object, which are available on the *OrcaFlex* website [Orc23c]. Within this database, report [Ros18] is of particular interest, as it investigates *OrcaFlex*' capability of modelling FOWTs by comparing it against alternative software solutions and research outcomes derived from FOWT prototypes. The findings confirm that *OrcaFlex* is a suitable software for this purpose, demonstrating the effective use of the *OrcaFlex* turbine object in modelling the generator, gearbox, hub, blades and associated control systems.

4.3.1 Choice for Time-Domain Analyses

As stated in [Orc23b], *OrcaFlex* offers two types of dynamic analysis: frequency-domain and time-domain. The former employs a linear analysis, while the latter is fully nonlinear and provides more accurate results, albeit with higher computational costs. According to [Far+22], the use of a time-domain analysis is crucial in accurately simulating the complex interactions of various components of a floating wind turbine in the basic design stage. While it may be of interest to explore the accuracy and sensitivity of results obtained through a frequency analysis in future investigations, such an inquiry is beyond the scope of this current study.

4.3.2 Choice of the Implicit Integration Scheme

As by [Orc23b], throughout the time domain analysis, the dynamics of the offshore system are simulated by breaking it down into interconnected elements. *OrcaFlex* adopts a time-stepping approach, whereby the system's behaviour is calculated at discrete time intervals. At each time step, the software calculates the forces acting on each segment of the system, including the effects of wave, current and wind, and solves the equation of motion (3) for the acceleration by using either an explicit or an implicit dynamic integration scheme.

$$\boldsymbol{M}(\boldsymbol{p})\boldsymbol{a} = \boldsymbol{F}(\boldsymbol{p}, \boldsymbol{v}, t) - \boldsymbol{C_l}(\boldsymbol{p}, \boldsymbol{v}) - \boldsymbol{K_l}(\boldsymbol{p}) \tag{3}$$

In this equation, $\boldsymbol{C_l}(\boldsymbol{p}, \boldsymbol{v})$ represents the damping load, $\boldsymbol{K_l}(\boldsymbol{p})$ the stiffness load, $\boldsymbol{F}(\boldsymbol{p}, \boldsymbol{v}, t)$ the external load, and $\boldsymbol{M}(\boldsymbol{p})$ the mass matrix. The vectors $\boldsymbol{p}$, $\boldsymbol{v}$, and $\boldsymbol{a}$ correspond to the position, velocity, and acceleration, respectively. For the explicit integration scheme, the equation of motion is solved locally for each free body and line node to obtain the acceleration vector at the start of each time step. Subsequently, the velocity and position vectors are determined at the end of each time step using a semi-implicit Euler integration method, expressing as:

$$\begin{cases} \boldsymbol{v}_{t+dt} = \boldsymbol{v}_t + dt\ \boldsymbol{a}_t \\ \\ \boldsymbol{p}_{t+dt} = \boldsymbol{p}_t + dt\ \boldsymbol{v}_{t+dt} \end{cases} \tag{4}$$

The generalised-α integration method is employed for the implicit integration scheme. Unlike the explicit scheme, the system's global equation of motion is solved at the end of each time step. Due to the lack of knowledge regarding the acceleration vector at the start of each time step, direct updates as seen in explicit solvers are not possible. Therefore, an iterative solution method is required. The implicit scheme requires more computational time per time step due

to its iterative approach. However, it offers greater stability for longer time steps. After careful examination of the documentation provided in [Orc23b], the decision was made to utilise the implicit integration scheme for the dynamic analysis. Considering the complexity of the system, which comprises a large number of nodes, employing the explicit integration scheme might necessitate a very small time step, thereby substantially increasing computational time. A schematic representation of the implicit solver is given in following figure 14.
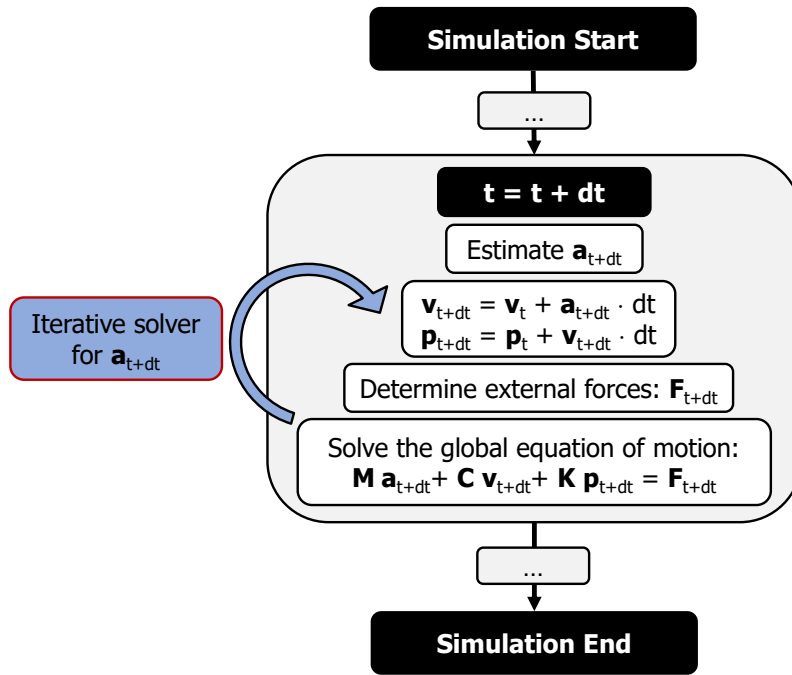
Figure 14: Schematic representation of the implicit solver employed in the time-domain dynamic analysis

4.3.3   Hydrodynamic Loads

The hydrodynamic loads in the system primarily affect two components: the floating substructure and the mooring lines. Due to the significant size of the floating substructure and the influence of wave diffraction, it is represented as a 'vessel' type in the *OrcaFlex* software. As detailed in section 4.2, *OrcaWave* is utilised to conduct a diffraction and radiation analysis on the floating substructure. The obtained results, including added mass and damping matrices, as well as load and displacement RAOs and wave drift QTFs, are imported into *OrcaFlex*. By incorporating these results along with the loads acting on interconnected objects, the motions of the floater are determined. On the other hand, the hydrodynamic loads on the mooring lines, represented by 'line' elements, are calculated using an extended version of the Morison equation. The basic Morison equation includes two force components: the fluid inertia force related

to particle acceleration $\boldsymbol{a}_{\mathrm{f}}$ and the drag force associated with particle velocity $\boldsymbol{v}_{\mathrm{f}}$, expressing as:

$$\boldsymbol{f} = \underbrace{C_{\mathrm{m}}\Delta\boldsymbol{a}_{\mathrm{f}}}_{\text{inertia}} + \underbrace{\frac{1}{2}\rho C_{\mathrm{d}}A\left|\boldsymbol{v}_{\mathrm{f}}\right|\boldsymbol{v}_{\mathrm{f}}}_{\text{drag}}, \tag{5}$$

with Δ the displaced mass, A the drag area and C_{m} and C_{d} the inertia and drag coefficients respectively. The more advanced version of the Morison equation used in *OrcaFlex* expands the principles to a moving body with acceleration $\boldsymbol{a}_{\mathrm{b}}$ and added mass coefficient C_{a} as:

$$\boldsymbol{f} = (C_{\mathrm{m}}\Delta\boldsymbol{a}_{\mathrm{f}} - C_{\mathrm{a}}\Delta\boldsymbol{a}_{\mathrm{b}}) + \frac{1}{2}\rho C_{\mathrm{d}}A\left|\boldsymbol{v}_{\mathrm{r}}\right|\boldsymbol{v}_{\mathrm{r}}. \tag{6}$$

4.3.4 *Wind Turbine Simulation Tool*

As specified in [Orc23b], *OrcaFlex* utilises the FAST software to simulate the behaviour of the turbine. This includes calculating the aerodynamic loads exerted on the turbine's blades and implementing its control system. FAST, as described in [NRE23], is a software that facilitates the simulation of coupled nonlinear aero-hydro-servo-elastic phenomena in the time domain by integrating models for aerodynamics, hydrodynamics, control, and structural dynamics.

The aerodynamic models implemented in FAST utilise wind-inflow data to compute blade-element aerodynamic loads using the *Blade Element Momentum Theory* (BEMT). BEMT, as described in [Mou14], is a combination of two theories: the *Blade Element Theory* and the *Momentum Theory*. The *Momentum Theory* involves applying conservation principles to a control volume encompassing the rotor. On the other hand, the *Blade Element Theory* focuses on analysing the forces acting on a blade section in relation to the incoming flow and the geometry of the blade. A comprehensive explanation of the theory underlying BEMT and the derivation of its governing equations can be found in appendix A.5. As by [Orc23b], the BEMT model in *OrcaFlex* undergoes slight modifications, and the methodology for calculating aerodynamic turbine loads is thoroughly explained in appendix A.6. Additionally, *OrcaFlex* improves these calculations by incorporating supplementary correction factors. These factors allow for the inclusion of complex phenomena like dynamic inflow, tip losses, and skewed wake effects.

4.4 Summary - Selected Software and Particularities

This section concludes by referring to figure 10, which highlights the high complexity of the system. From this perspective, the particularities involved in the modelling of FOWTs are de-

scribed. For the dynamic analysis, *OrcaFlex* is chosen due to its strong capability and proven validity in modelling such systems. Time-domain analysis is preferred over frequency-domain analysis because of its ability to capture non-linear behaviour and provide higher accuracy in results. Although explicit integration schemes are generally faster, their efficiency decreases significantly for systems with high complexity and a large number of nodes. Therefore, an implicit integration scheme is applied in this case. To incorporate the hydrodynamics of the floater, a diffraction and radiation analysis is performed using *OrcaWave* software prior to the dynamic analysis. The resulting load and displacement RAOs and wave drift QTFs are used as input for the dynamic model. The hydrodynamics of the mooring lines are accounted for using the Morison equation within *OrcaFlex*. The aerodynamics of the blades are considered by employing *Blade Element Momentum Theory* (BEMT) with the integration of the FAST software into *OrcaFlex*. This integration further enables modelling of the turbine control system. The consideration of the structural dynamics of the blades and the tower is ensured by the system's finite element approach.

5 SIMULATION PROCEDURE

5.1 Introduction

This section establishes the layout of the simulation procedure and outlines the choices made regarding software parameters. It begins with the selection of load cases as environmental inputs and the choice of output parameters. Subsequently, it delves into aspects like simulation duration, time step length, and initialisation time. Figure 15 provides an overview of the general procedure followed for each model simplification. Notably, the utilisation of a reference model is depicted, which is further detailed in section 6.3. Model simplifications are directly applied to this reference model, where the distinctive characteristics of each simplification necessitate manual model adaptations. To perform the simulation process, a *Python* code is employed. It is used not only to automate the simulations, but also to analyse and compare the results.
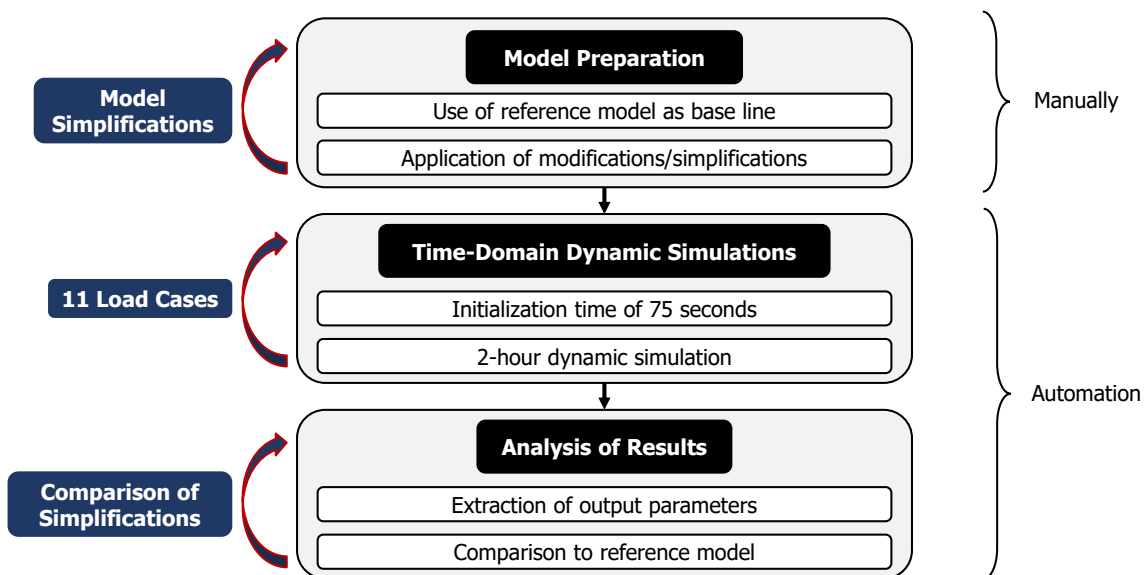
Figure 15: Simulation procedure employed throughout the entire research

5.2 Environmental Load Cases

The floating wind turbine model experiences a combination of environmental loads, including wind, wave, and currents. To evaluate the performance of the model, the DNV-ST-0437 standard [DNV21c] provides a set of design load cases (DLCs). These DLCs encompass a range of 'normal' and 'extreme' environmental configurations, offering a comprehensive representation of the diverse scenarios that floating structures may encounter and must withstand. The complete

list of DLCs can be found in appendix C.4, serving as a foundation for selecting appropriate environmental conditions in this study. Although a three-dimensional model is employed and multi-directional DLCs are available, this analysis primarily focuses on one-directional loads. The study concentrates on evaluating the turbine's performance under normal operational conditions, with extreme events being disregarded for the purpose of this analysis.

5.2.1 Wind

According to the classification standard [DNV21a], many of the load cases are dominated by wind loads. Additionally, as mentioned in [DNV21c], normal wind conditions hold great importance in the design process of FOWTs. They are not only important for determining fatigue loads but they also lead to more severe loads, as aerodynamic thrust forces are highest around rated wind speeds as shown in figure 68 (b). While extreme wind conditions, including peak wind speeds during storms and rapid changes in wind speed and direction, are typically used to assess the extreme loads on wind turbines, this study focuses on operational wind speeds ranging from 3 to 25 m/s (see figure 21 for the reference turbine).

According to [DNV21a] wind conditions can be considered stationary over a 10-minute duration, with deviations within this timeframe referred to as turbulence. To model these turbulence effects, the NPD spectrum is employed based on its refined representation of wind turbulence in the low-frequency range, as mentioned in [DNV21b]. Additionally, the NPD spectrum is suitable for modelling one-dimensional wind flows, as stated in [DNV21a]. Further details on turbulence modelling and the NPD spectrum can be found in appendix A.4.

5.2.2 Waves

Appendix A.3 provides an overview of wave spectral representation methods and their applicability. For this study, the JONSWAP spectrum is utilised to model waves due to its widespread use and its ability to represent developing seas, as discussed in [PK17]. As expressed in equation (16), the spectrum is characterised by a peak frequency, a peak enhancement factor, and a reference wave height, typically the significant wave height. In this research, the peak enhancement factor is set as one since the exact sea configuration is unknown, and both the peak frequency and significant wave height are defined for each specific load case.

5.2.3   Current

Consulting the class society standard [DNV21c] highlights the significance of including the effect of current. The standard suggests modelling the current as a combination of wind-generated currents and tidal currents, which exhibit variations along the vertical direction. According to [Wik22], tidal currents are strongest in large water depths, far away from the coastline and straits, with typical maximum current speeds in tidal inlets being around 1 m/s, reaching up to 3 m/s in more severe locations. In this study, as no site-specific data is available, the tidal current speed at still water level $U_{tide,0}$ is assumed to be 1 m/s. [DNV21c] provides analytical formulas for vertical variation of currents, along with the relationship between wind-generated current and the 10-minute mean wind speed V_{10}, as depicted in equation (7). Here, z represents the vertical coordinate measured from the still water level, positive upwards, d denotes the water depth measured from the still water level, and d_0 represents the reference depth for wind-generated current, which is set to 50 meters for this research.

$$U(z) = U_{tide,0} \left(\frac{d+z}{d} \right)^{\frac{1}{7}} + kV_{10} \left(\frac{d_0+z}{d_0} \right) \tag{7}$$

5.2.4   Combined Load Cases

The environmental loads in this study are determined based on the design load cases (DLCs) presented in appendix C.4, with particular emphasis on DLC 1.1. These DLCs specify the environmental conditions to be considered; however, their magnitudes are contingent upon site-specific data. As this research does not focus on a specific site, data from a generic U.S. East Coast site is adopted. In [Ste+16], the construction of the generic site is achieved by observing the correlation between wind speed, wave height, and wave period at various offshore sites along the coast. Through an averaging process, the data obtained from these observations are utilised to create the representation of the generic site. Mean wind speeds ranging from 3 to 25 m/s, along with the associated wave heights and peak spectral periods, are obtained from [Gae+20]. These data serve as the foundation for establishing the 11 load cases outlined in table 6. These load cases will be employed in the simulations conducted throughout this study.

Table 6: Load cases for this research; based on environmental conditions for a generic site [Gae+20]

Load Case	Wind Speed	Significant Wave Height	Peak Spectral Period
	[m/s]	[m]	[s]
1	4	1.1	8.5
2	6	1.2	8.3
3	8	1.3	8.0
4	10	1.5	7.6
5	12	1.8	7.4
6	14	2.2	7.5
7	16	2.6	7.6
8	18	3.1	8.0
9	20	3.6	8.5
10	22	4.0	9.0
11	24	4.5	9.5

5.3 Choice of Output Parameters

Based on the literature review discussed in section 3, the present study identifies the output parameters that will be extracted and analysed for each simulation. As stated in article [Zho+21], the platform tilting angle and absolute nacelle acceleration are crucial outputs for dynamic analyses, as they indicate whether the movements are within acceptable limits for wind turbine operations. Additionally, the article emphasises the importance of assessing fatigue damage at the tower base and fairlead. Therefore, the absolute tower base bending moment and mooring line tension at the fairlead are selected as further outputs. Furthermore, absolute nacelle velocity is chosen since the movements of the nacelle are critical in the design of FOWTs. Finally, simulation length is selected, as it reflects computational expenses. It refers to the duration of time between the initiation of the simulation and its final completion, encompassing all ongoing processes and computations. To ensure meaningful results, all simulations are conducted under the same conditions. Specifically, the simulations are performed overnight when the machine is dedicated solely to this task, thereby allowing optimal allocation of system and hardware resources.

5.4 Simulation Length

The selection of the simulation length involves several considerations. The necessary duration to account for wind turbulence is investigated, followed by an assessment of industry standards. Finally, a study-specific analyse is performed to get a simulation length tailored to requirements.

5.4.1 Simulation Length for Wind Dynamics

According to [DNV21c], a minimum simulation length of 10 minutes is necessary to account for the transient behaviour of the wind and its effects on turbine performance. Consulting appendix A.4.5, figure 16 illustrates that variations in wind speed can be attributed to either short-term turbulence or long-term diurnal and synoptic effects, arising from changes between day and night and the movement of weather systems, respectively. Modelling wind speed over a 10-minute duration allows to capture the short-term variations caused by turbulence, as spectral density is minimal for wind periods between 10 minutes and 2 hours. Low-frequency variations resulting from long-term effects are incorporated utilising wind speed distributions.
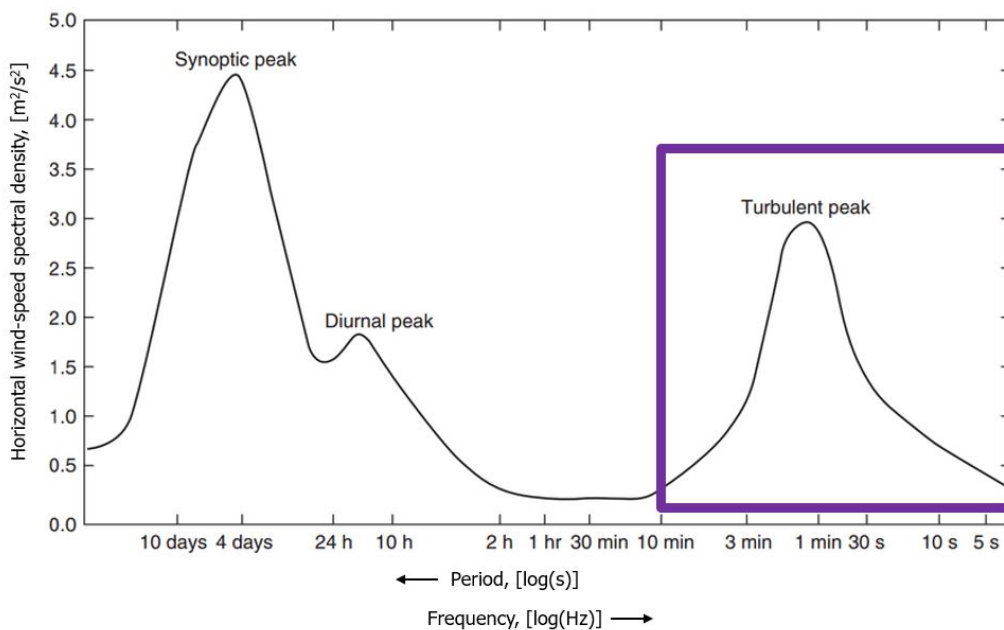
Figure 16: Horizontal wind speed spectral density as a function of the wind frequency [Sia+21]

5.4.2 Simulation Length for Turbine Design

The class document DNV-ST-0437 [DNV21c] provides guidance on how simulation length is chosen for the design of FOWTs. Ensuring statistical reliability requires a sufficient total length of load data. However, the recommended approach differs from that for offshore oil and gas applications, where simulations over 3 hours or more are typically employed. For FOWTs, it is preferable to conduct a number of 10-minute simulations using different environmental seeds. The number of simulations depends on the load cases involved. For DLCs with turbulent wind fields, a minimum of six 10-minute stochastic realisations with different turbulent seeds are

required for each mean wind speed. Turbine loads and dynamics are determined by stochastically combining results obtained from different seeds. Certain DLCs may necessitate a higher number of 10-minute simulations, such as DLC 2.1, which requires a minimum of twelve simulations. Article [Hai+13] deals with concerns about the suitability of the 10-minute simulation length for modelling combined loading, given that floating platforms have lower natural frequencies than fixed-bottom ones, leading to fewer load cycles over a given period of time. It is found that the simulation length does not significantly impact ultimate loads. Furthermore, concerning fatigue loads, it is demonstrated that the procedure used for counting half cycles is more important than the simulation length itself. To sum up, it is concluded that conducting a larger number of 10-minute simulations produces the same results as longer simulations.

5.4.3 Simulation Length for this Study

Above results show that achieving statistical reliability in the design of FOWTs involves conducting a large number of simulations with different environmental seeds, each of relatively short duration. However, the objective of this study is not to design a FOWT but to compare simulations with different models under the exact same loads, using the same environmental seed. Therefore, a simulation length is chosen that requires only one simulation per load case for stochastic reliability. To determine the necessary simulation length, simulations with increasing duration are conducted for the reference model and the average and standard deviation of output parameters are computed. Figure 17 illustrates results for absolute nacelle acceleration, tower base bending moment and mooring line tension for load case 6. It can be observed that after surpassing a simulation length of 2 hours, the output parameters exhibit minimal variations. Therefore, to ensure statistically reliable comparisons between results, 2-hour simulations are employed. The environmental seed number is selected randomly.

5.4.4 Initialisation Time

According to [Hai+13], appropriate initial conditions and the removal of start-up transients are critical for accurate simulation results. The paper suggests that the initial simulation time that needs to be disregarded should be extended to at least 60 seconds to eliminate the effects of start-up transients. Observing the high complexity of the model, an initialisation time of 75 seconds is incorporated into the dynamic analyses, allowing the system to settle into a stable state before the start of the actual simulation.

34
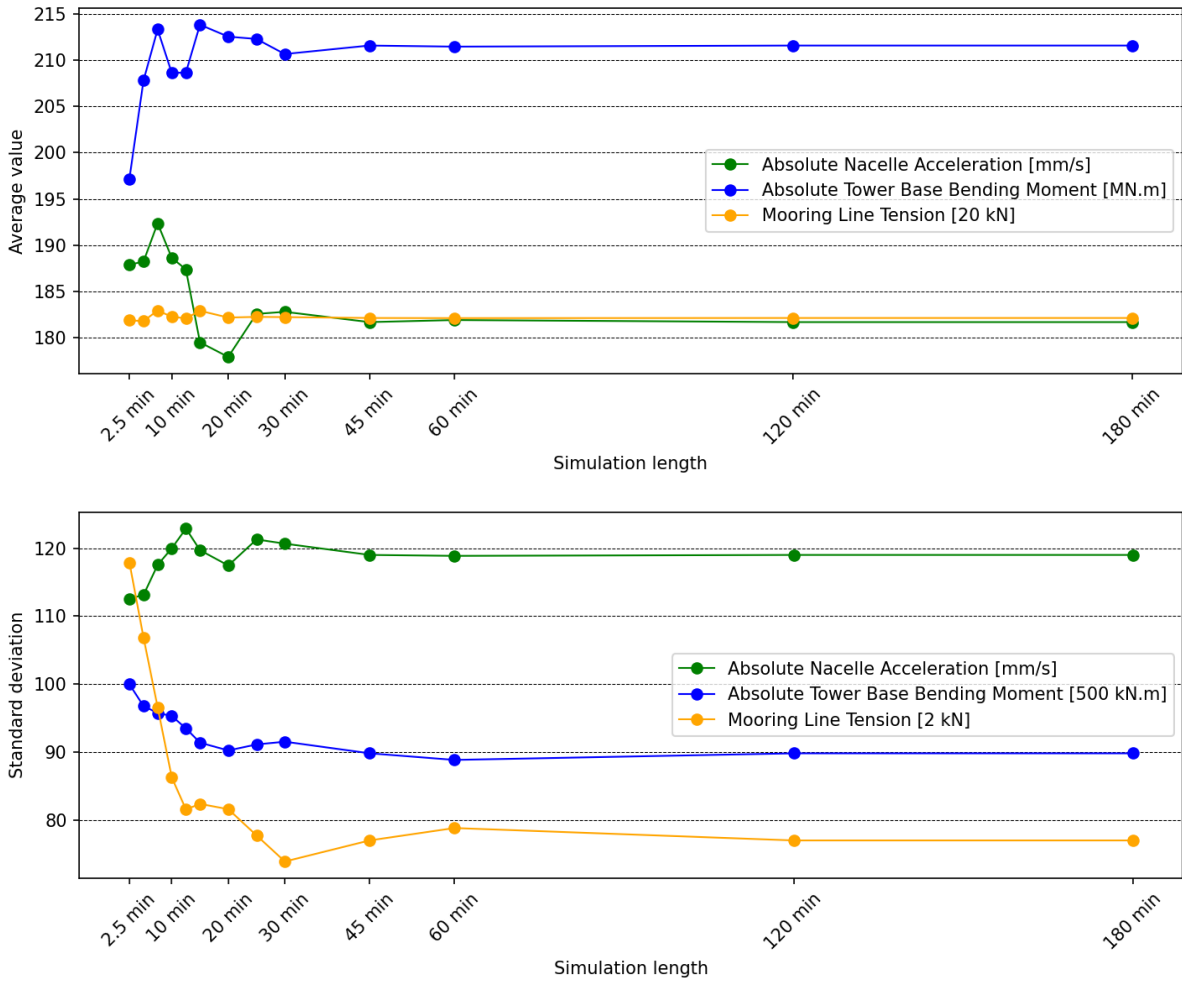
Figure 17: Average and standard deviation of the time-variation of absolute nacelle acceleration, absolute tower base bending moment and mooring line tension as a function of simulation length for load case 6

5.5 Time Step

A constant time step is employed throughout all simulations. According to [Orc23b], the value of this time step must be chosen carefully, as even for stable simulations, inaccurate results can be produced if the time step is too large. A sensitivity study is conducted, and a time step of 0.025 seconds is chosen, ensuring a reasonable number of iterations for a time step that is not overly small. More specifically, for all load cases for the reference turbine model, the number of iterations per time step does not exceed 5, which is within recommendation according to [Orc23b]. In contrast, selecting *OrcaFlex'* default time step of 0.1 seconds results in an iteration count of up to 72 iterations per time step, which is significantly too high.

5.6   Automation of Simulations

The simulation procedure, as depicted in figure 15, is automated using a *Python* code. The code takes *OrcaFlex* '.dat' files as input, containing the turbine model and software specifications. It defines the environmental loads, runs the simulations, extracts results and saves them in *Excel* files. Another *Python* code then utilises these result files for different model simplifications and performs a comprehensive comparison, including both visual and numerical analyses.

5.7   Summary - Simulation Set-up and Output Parameters

In summary, this section provides an overview of the input and output parameters used in the simulations. The environmental loads, considering joint probabilities between wind and waves, focus on the operational region of the wind turbine, prioritising normal operation over extreme conditions. For output parameters, the absolute nacelle acceleration and velocity, platform pitch, absolute tower base bending moment, and tension at the front-end mooring line fairlead are extracted. These parameters are crucial in understanding the turbine's operational limits and fatigue behaviour. Additionally, the extraction of simulation time enables the analysis of the benefits of model simplifications. To ensure statistical reliability, simulations length is set to 2 hours with an additional 75 seconds of initialisation time. A time step of 0.025 seconds is selected to limit the number of iterations per time step. A *Python* code is developed to perform the dynamic simulations and automate the analysis of the results.

6 TURBINE CONTROL AND DYNAMICS

6.1 Introduction

This section aims to provide a comprehensive overview of the operational principles and control mechanisms employed in wind turbines, with a particular emphasis on floating offshore wind turbines. The reference wind turbine is introduced and a detailed examination of the rotor ramp-up and shut-down sequences is performed. Additionally, resonance behaviour is investigated and the influence of wind and wave loads on output parameters from section 5.3 is explored.

6.2 Principle of Power Extraction and Turbine Control

Based on the detailed description of the main components of a wind turbine, given in appendix A.1, the principle of power production is investigated. As described in [AO20], the control of a wind turbine is primarily influenced by two factors, the rotational speed and the extracted power, which mathematically expresses as:

$$P_w = 0.5\rho A C_p V^3 \ . \tag{8}$$

ρ is the density of air, A the rotor area, V the wind speed, and C_p the power coefficient. As stated in appendix A.2, the power coefficient is determined by two factors: the blade pitch angle β and the tip speed ratio λ. According to Betz's law, the power coefficient is theoretically limited to a maximum value of 0.593. The tip speed ratio represents the ratio of the rotor's angular velocity ω and its radius R to the velocity of the incoming wind V, and is mathematically defined as:

$$\lambda = \frac{\omega R}{V} \ . \tag{9}$$

6.2.1 Main Operational Regions

Figure 18 illustrates the increase of wind power with wind speed, as well as the optimal theoretical power that the turbine aims to extract. According to [Lóp+22], the power generation of a wind turbine can be categorised into four main regions. In region I, which is below the cut-in wind speed, the wind speed is insufficient for the turbine to operate effectively. The turbine remains idle, resulting in no power production. Region II, known as the *partial load operation region*, spans from the cut-in wind speed to the rated wind speed. The primary objective in this

region is to maximise the extracted power, which is why the turbine operates at its maximum power coefficient $C_p(\lambda^*, \beta^*)$. This is accomplished by keeping the blade pitch angle constant at its optimal value β^* (typically found to be $0°$), as illustrated in figures 52 and 53 in appendix A.2. Simultaneously, the rotational speed is adjusted to maintain a constant tip speed ratio λ^* that corresponds to the maximum power coefficient. Region III, also referred to as the *full load operation region*, occurs when the wind speed exceeds the rated wind speed. In this region, the extracted power is limited to the turbine's rated value to prevent structural and electrical damage. A constant generator torque is imposed on the turbine and by implementing an active pitch control, blade pitch is constantly adapted to keep the rotor speed constant. When wind speed increases, the blade pitch angle is increased, reducing the angle of attack and thus limiting the aerodynamic forces exerted on the blades. Finally, when the wind speed surpasses the cut-out wind speed, the turbine is shut down to prevent potential structural damage. Despite the presence of a mechanical brake in the turbine, its usage is primarily reserved for emergency situations. For a turbine shutdown, *blade feathering* is employed, as explained in [Sam+20]. The process involves increasing the blade pitch angle, thereby orienting the leading edge of the blades into the wind. This action leads to a reduction in the aerodynamic forces acting on the blades. To achieve a complete shutdown, the blade pitch angle is increased to its maximum value of $90°$.
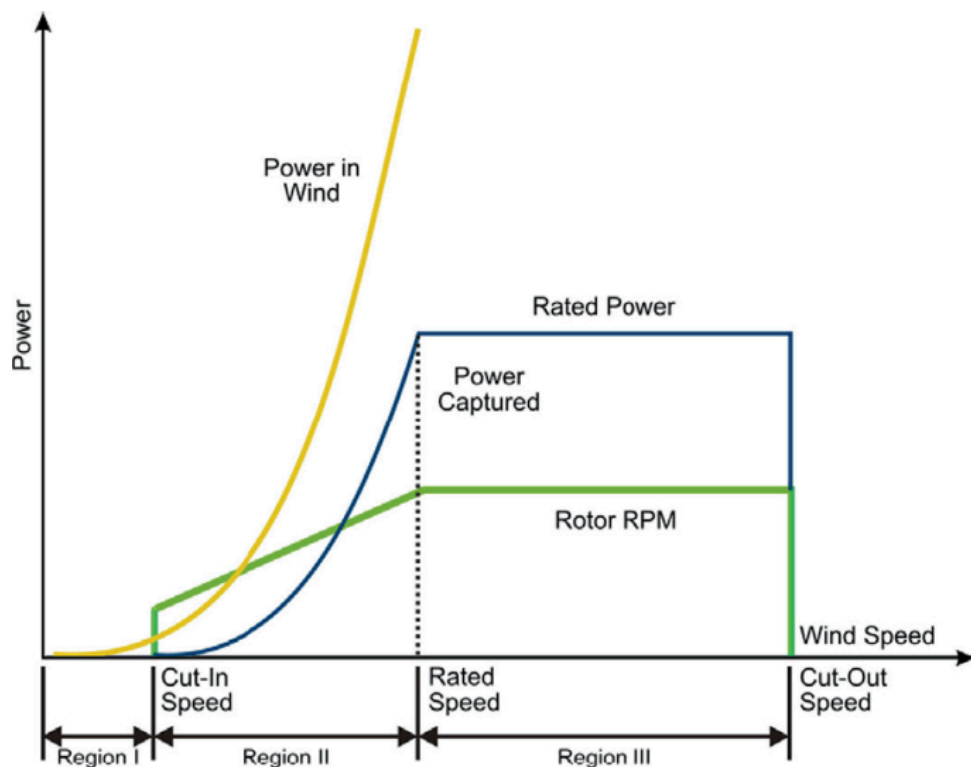
Figure 18: Ideal power curve and the different operational regions [EAA22]

6.2.2   Transition Regions

According to [Lóp+22], the transition zone between regions 2 and 3 of the power curve is designed to provide a smooth switch from partial load control to full load control. The specific control strategy employed in this region varies among turbine manufacturers and involves adjusting both the tip speed ratio and the blade pitch. The goal is to ensure a seamless transition without abrupt changes in power output, as can be observed in figure 19 below.
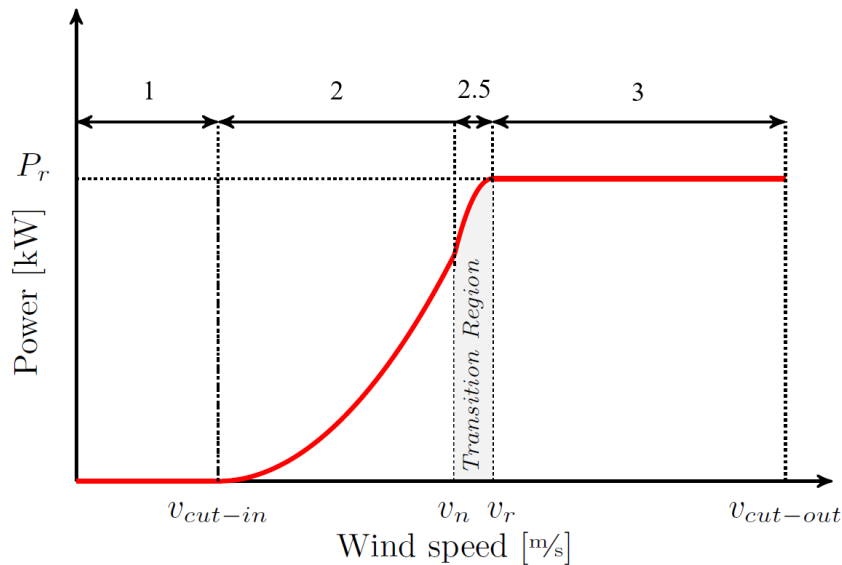
Figure 19: Power curve with transition region [Sam+20]

Similarly, wind turbines commonly incorporate a transitional region, known as region 1.5, which facilitates the transition between standstill and operational configurations. Again, specific characteristics of this region vary, depending on turbine manufacturers' choices.

6.2.3   Floating Offshore Wind Turbine Control

As highlighted in [Far+22], the dynamics of floating wind turbines are significantly more complex compared to their bottom-fixed counterparts. In the context of floating wind turbines, as discussed in [Lóp+22], the combined influences of aerodynamic and hydrodynamic loads together with the turbine control system can significantly contribute to the dynamic motion of the floating platform. This might lead to increased fatigue damage and reduced operational lifespan of the structure. Figure 20 illustrates the impact of negative damping, which serves to demonstrate the strong coupling between platform motions and turbine control. When operating in region 3 above rated wind speed and an increase in wind speed occurs, the turbine responds

by adjusting the blade pitch angle to reduce aerodynamic loads. This reduction in aerodynamic forces can cause the floating platform to pitch forward. This forward pitch, in turn, alters the relative velocity experienced by the blades, further influencing the aerodynamic forces acting on them. The dynamic effects and fore-aft oscillations resulting from these interactions depend on the specific characteristics and properties of the FOWT. The control system plays a crucial role in mitigating these dynamic effects and controlling the behaviour of the turbine. In Appendix A.2.6, various approaches are presented on how the turbine controller can be adapted to counter these dynamic effects.
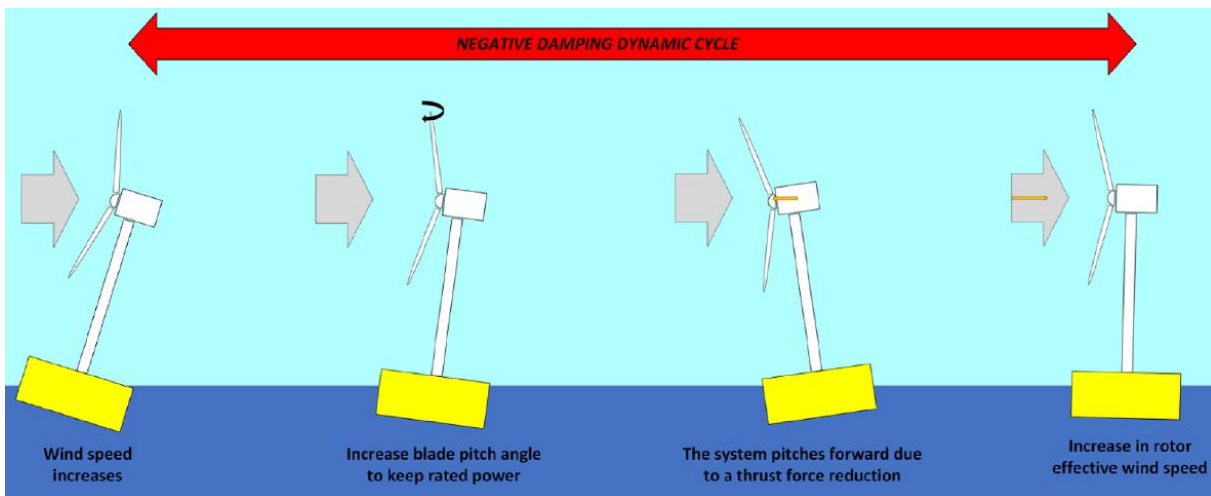
Figure 20: Negative damping dynamic cycle experienced by a FOWT [Lóp+22]

6.3   Reference Wind Turbine

The chosen reference for this study is the 15 MW floating offshore wind turbine shown in figure 21, with its selection justified in appendix B.1. Additionally, appendix B.1.1 provides insight into its control system, emphasising that the thrust force reaches its peak at the rated wind speed of 10.6 m/s, resulting in the highest aerodynamic forces. This information holds significance for subsequent analyses. A comprehensive description of the turbine's layout and main parameters can be found in appendix C.3. Moreover, an *OrcaFlex* model of this turbine, available at [Orc23a], will serve as the reference for the simulations, as described in appendix B.1.2. It is important to note that the model's complexity, as highlighted in appendix B.1.3, may lead to considerable computational efforts and high simulation time.

Parameter	Value	Unit
Rated power	15	MW
Rated wind speed	10.59	m/s
Cut-in wind speed	3	m/s
Cut-off wind speed	25	m/s
Hub height	150	m
Total height	290	m
Rotor diameter	240	m
Length	90	m
Width	102	m
Platform type	semi-submersible	-
Freeboard	15	m
Draft	20	m
Total mass	20,093	tons
Platform mass	17,839	tons
Tower mass	1,263	tons
RNA mass	991	tons
Mooring system	catenary	-

Figure 21: Key parameters and layout of the 15-MW reference floating offshore wind turbine [All+20]

6.4 System Dynamics During Turbine Start-Up and Shut-Down

Further explanation is required for system dynamics observed during rotor start-up and shut-down. They are of particular importance for constructing the simplified model in section 8.

6.4.1 Rotor Start-Up

The dynamic simulations for the FOWT all begin with the turbine in a standstill configuration. To initiate rotation and enter power-production mode, the rotor requires torque exerted by the wind. It is observed that higher wind speeds result in higher torque, leading to faster start-up procedures. Figure 22 illustrates the rotor thrust and rotor angular velocity for the first 250 seconds of the second load case, which corresponds to a relatively low mean wind speed of 6 m/s. The applied torque on the rotor is small, resulting in a longer start-up time. The aerodynamic forces acting on the blades depend not only on wind velocity but also on the blade rotational speed, as depicted in figure 51 in appendix A.2. This dependence directly affects the forces experienced by the turbine, and can be seen in figure 22. The Pearson correlation coefficient between angular velocity and thrust is 0.97 for the first 150 seconds of the simulation, indicating the linearity of their relationship. For higher load cases, a similar dependency is observed. However, ramp-up times are shorter since higher wind speeds lead to higher rotor torque and greater rotational ac-

celeration. In section 8.4.3, the dependency of thrust and torque on rotational speed will be used for the construction of the simplified model. It is worth noting that these variations in aerodynamic loads during turbine start-up strongly influence the system dynamics. For example, the platform pitch, which is considered positive when the structure leans forward into the wind, undergoes significant changes. In the absence of wind and wave loads, the turbine is in static equilibrium at a positive pitch angle of 1.3 degrees, leaning forward. However, as the turbine starts rotating and the aerodynamic thrust force increases, the pitch angle changes sign, causing the turbine to lean backward. This example illustrates the system's high complexity, since changes in pitch on their part have profound effects on turbine aerodynamics.
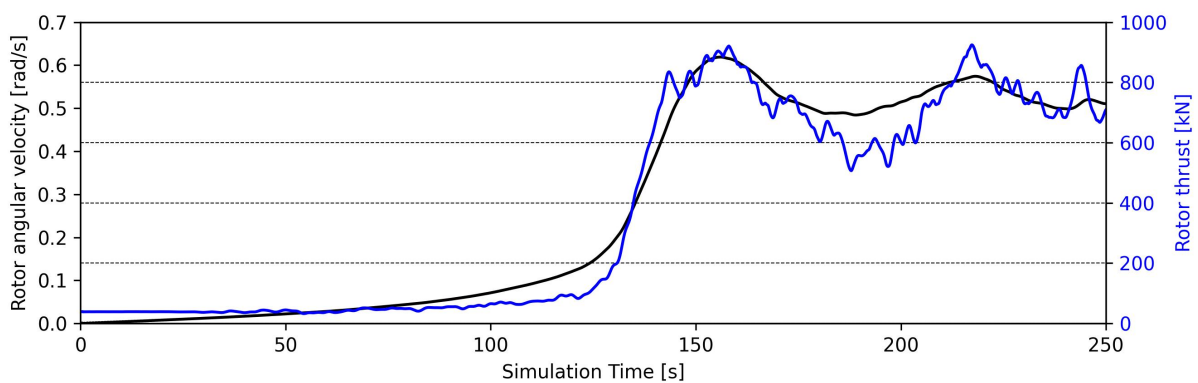
Figure 22: Rotor thrust and rotor angular velocity for the reference wind turbine in load case number 2

6.4.2   Rotor Shut-Down and Blade Pitch

As described in section 6.3, the operational region of the reference wind turbine is defined by a cut-off wind speed of 25 m/s, marking the end of region 3 where turbine performance is controlled using a blade pitch system. The blade pitch angle is continuously adjusted, with a maximum rate of 2 degrees per second, to accommodate the incident wind speed. When blade pitch exceeds 20 degrees, the shut-down procedure is initiated, utilising blade feathering to stop the turbine by orienting the leading edge of the blades into the incident wind. Figure 23 illustrates the adaptation of the blade pitch angle during the shut-down procedure of load case 10, resulting in a significant decrease not only in rotor torque, but also in aerodynamic thrust force. Rotor shut-down is observed only for load cases 10 and 11, as the lower wind speeds associated with lower load cases do not cause the blade pitch angle to exceed the critical limit of 20 degrees. Results are used for modelling rotor shut-down of the simplified model in section 8.4.4.
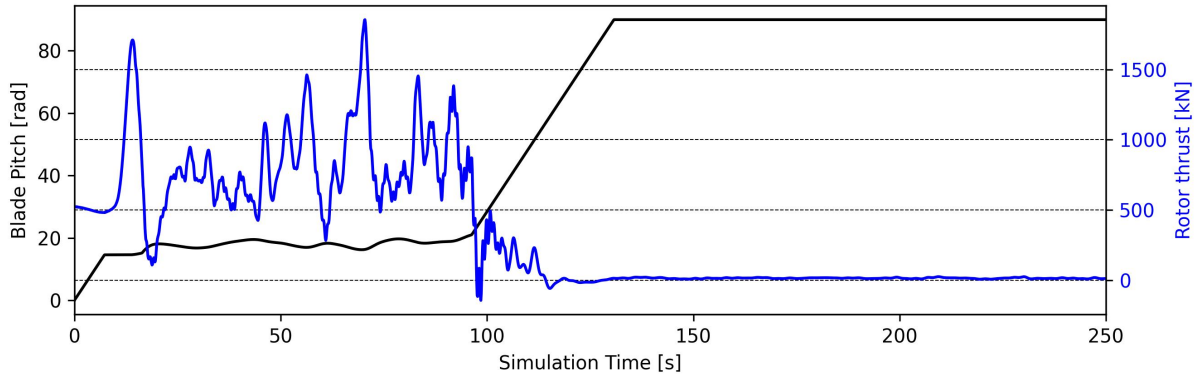
Figure 23: Blade pitch and rotor thrust for the reference wind turbine in load case number 10

6.5 Resonance Behaviour

Resonance is a critical phenomenon to explore as it can result in amplified responses and potential structural damage. When the natural frequency of the structure aligns with the frequency of external forces, even relatively small forces can induce large amplitude vibrations, leading to elevated stresses and strains on the structure. As demonstrated in appendix A.4.6 and supported by [Vel+19], waves with their well-defined oscillations at lower periods present a higher risk for resonance phenomena in offshore structures compared to wind. Consequently, for this resonance analysis, only wave loads are taken into consideration. As the focus of this research is on one-directional loads (section 5.3), waves with a heading of 0 degrees are investigated.

The RAOs obtained from the diffraction and radiation analysis conducted using *OrcaWave* (section 4.2) are utilised for this analysis. First observations focusing on the displacement RAOs show that none of the Degrees of Freedom (DOF) exhibit peaks for wave periods below 20 seconds. The heave displacement RAO reaches its maximum at 21 seconds, while the pitch displacement RAO peaks at 30 seconds. As indicated in table 7, peak spectral periods between 7.4 and 9.5 seconds are employed in this study. Thus, it can be concluded that, from a displacement perspective, the risk for resonance phenomena is minor, as the displacement resonance periods are far from the observed wave periods. On the other hand, when examining the load RAOs, values of significant amplitude are observed in the range of wave periods of interest. Specifically, load RAOs for surge, heave, and pitch show important amplitudes, while amplitudes for sway, roll, and yaw are relatively negligible. Figure 24 illustrates the amplitude of load RAOs, revealing that the main peak for surge is obtained at a wave period of 7.5 seconds, for heave at 11 seconds, and for pitch at 9 seconds.

43
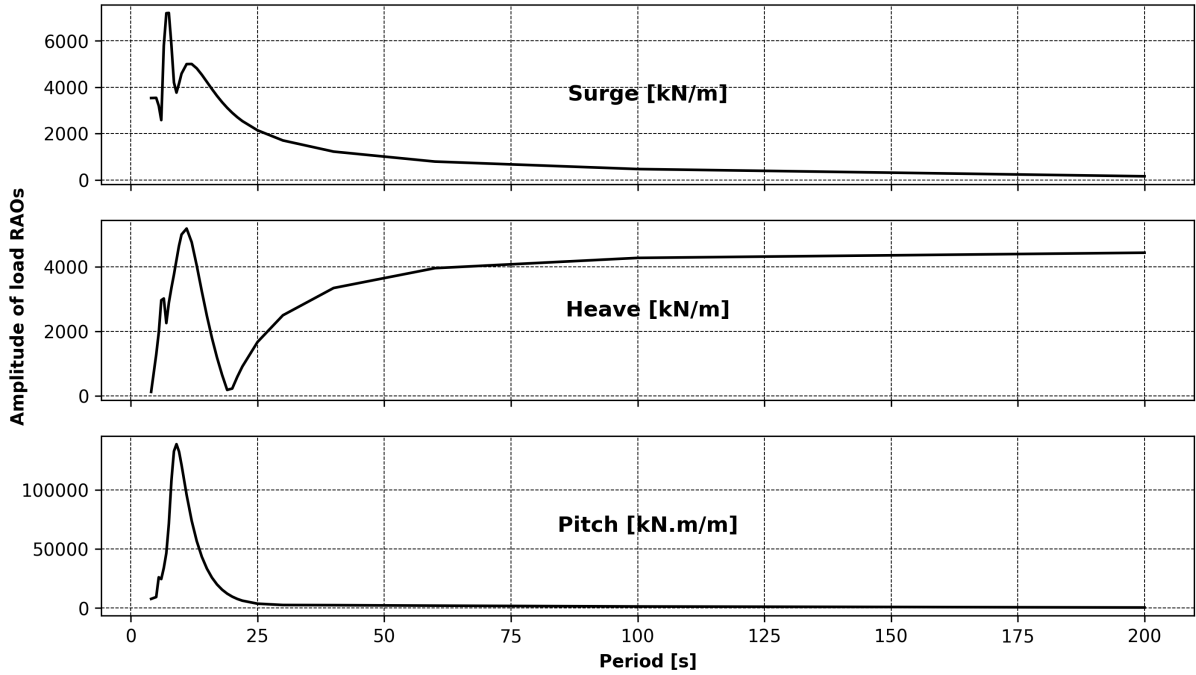
Figure 24: Amplitude of surge, heave and pitch load RAOs for a zero degree wave heading

6.5.1 *Influence of Wave Resonance on Output Parameters*

The influence of wave resonance effects on the output parameters is investigated. Simulations are conducted with regular waves of 3 metres height and periods ranging from 5 to 14 seconds, covering the peak spectral periods of the irregular waves used for the load cases in table 7. No wind or current loads are applied and the rotor is in standstill position. The results are presented in figures 25, displaying the maximum values of the output parameters for the different wave periods. It is observed that absolute nacelle acceleration, velocity, and tower base bending moment exhibit clear peaks at a wave period of 8 seconds. These resonance peaks can be correlated with the load RAOs shown in figure 24, where surge and pitch show resonance peaks at 7.5 and 9 seconds, respectively. On the other hand, observing the maximum values of mooring line tension, no clear resonance phenomena are evident. In contrast, floater pitch exhibits a peak at 9.5 seconds, which can be attributed to the pitch displacement RAO. As established above, this displacement RAO shows a primary peak at a wave period of 30 seconds, representing the main resonance phenomenon. However, a smaller peak emerges at a wave period of 9.5 seconds, with an amplitude of 19% compared to the primary peak. This secondary peak is responsible for the resonance behaviour depicted in figure 25, and its limited magnitude explains the relatively shallow shape of the pitch resonance curve.

44
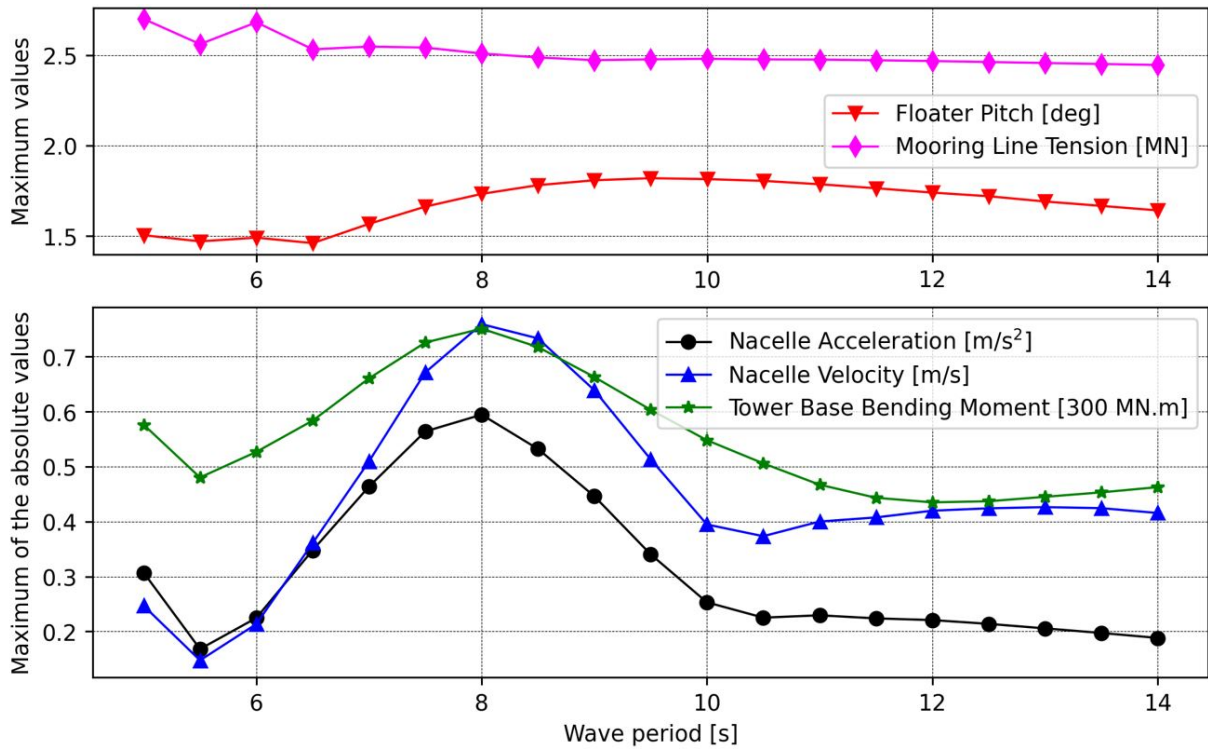
Figure 25: Maximum of the output parameters for different wave periods

6.6 Influence of Waves and Wind

This subsection aims to investigate how wind and wave environmental conditions impact the in section 5.3 selected output parameters. Two approaches are used: first, by analysing simulations with only wind or wave loads applied to the FOWT, and second, by establishing correlations between aerodynamic loads, wave height and output parameters.

6.6.1 Wind and Wave Loads Only

Two-hour simulations are conducted for each of the 11 environmental load cases. Besides applying the loads described in table 6, additional simulations are conducted where only wind or wave loads are applied to the FOWT. This has the purpose of understanding their respective influences on the system dynamics. Figure 26 shows the average and standard deviations of platform pitch for these load cases. It is important to note that platform pitch is negative when the structure leans away from the wind and positive when it leans into the wind. In simulations with waves only, the platform exhibits a forward lean. Despite the mean wave height increasing with the load cases, the average platform pitch only changes slightly. The standard deviation observed for these simulations with wave-only loads is on average just about 21% of the standard deviation observed for the combined load cases. However, this standard deviation increases

with the load cases. For simulations with wind loads only, results are very similar to those with combined loads. The average relative difference is less than 6%, and the standard deviation is also highly similar, with an average relative difference below 5%. This allows to conclude that the platform pitch in combined load cases is mainly dependent on wind loads.
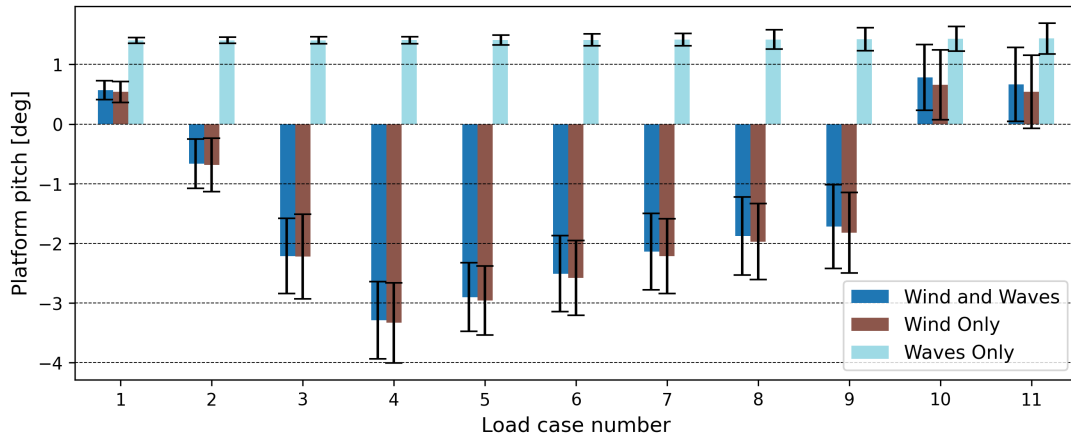
Figure 26: Average and standard deviations of platform pitch for wind loads only, wave loads only and combined load cases

The absolute tower base bending moment exhibits similar trends. Neglecting wind loads results in nearly constant average values across the load cases. From further analysis, it is seen that two main factors contribute to this bending moment: aerodynamic thrust forces and gravitational loads acting on the rotor, nacelle and tower. In simulations with wave loads only and no wind loads, the turbine leans forward, and the bending moments in the tower base are mainly due to gravitational loads. As the load case number increases, the variation of platform pitch also increases, leading to greater variation in the bending moment. As influence of wind loads on platform pitch has already been demonstrated, the same conclusion can be drawn for the tower base bending moment. Further, it is found that wind loads dominate the mooring line tension.

The impact of wind and wave loads on absolute nacelle acceleration and velocity is more complex. Figure 27 shows that both load sources influence the average values, as nacelle accelerations remain significant for most cases even when one load source is disregarded. For load cases at rated wind speed and above (load case 4-6), wind loads show a strong influence. However, the significant increase in average acceleration beyond the 6th load case for combined loading, in contrast to the rather slow increase for wind loading only, indicates that wave loading plays a greater role. This becomes even more evident in load cases 10 and 11, where average absolute nacelle accelerations are considerably lower for simulations with wind loads only, while remaining high for both combined loading and wave loads only. The subsequent section 6.6.2

will provide a more in-depth analysis to shed further light on this observation.
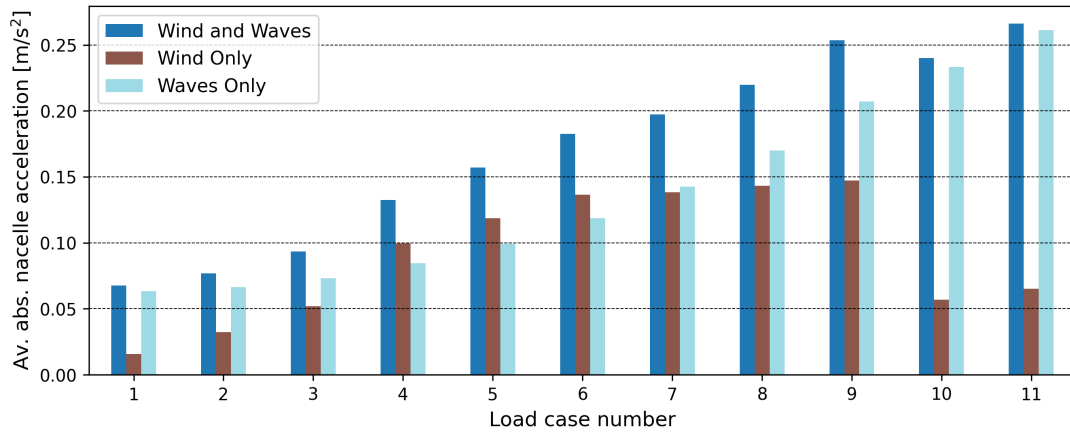
Figure 27: Average absolute nacelle acceleration for wind or wave loads only and combined load cases

6.6.2 Correlation Between Environmental Loads and Output Parameters

This subsection focuses on establishing correlation coefficients between environmental loads, represented by average aerodynamic thrust force and significant wave height, and the output parameters' average or maximum values. Figure 28 presents the average values for rotor thrust and absolute tower base bending moment from the two-hour simulations with combined loading. By observing the similarity in the shape of the curves, the strong connection between the two variables is highlighted. This finding reinforces the conclusions drawn in the previous subsection 6.6.1, stating that the tower base bending moment is mainly influenced by wind loads.
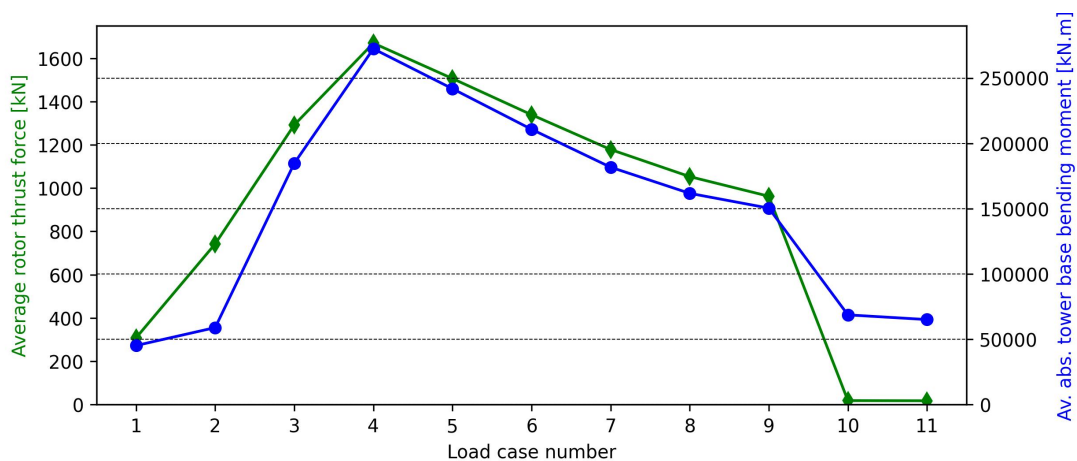
Figure 28: Average rotor thrust force and average absolute tower base bending moment for each load case

To quantify the relationship, the Pearson correlation coefficient is used, a detailed description of which is available in appendix A.9. For the average absolute tower base bending moment and

47

the average thrust force, the coefficient is found to be 0.93. This indicates a strong positive correlation, suggesting that when a load case presents a high average thrust force, chances are that the average absolute tower base bending moment is also high. Expanding this analysis to other output parameters, the Pearson correlation coefficients are calculated between the maximum and average values of the output parameters and the average rotor thrust force and significant wave height. The results are presented in table 7.

Table 7: Pearson correlation coefficient between the average thrust force or the significant wave height and the average or maximum of output parameters

		Average Thrust	Significant Wave Height
Abs. Nacelle Acceleration	Av.	-0.27	0.96
	Max.	-0.11	0.89
Mooring Line Tension	Av.	0.89	-0.09
	Max.	0.68	0.23
Abs. Tower Base Bending Moment	Av.	0.93	-0.27
	Max.	0.69	0.21
Abs. Nacelle Velocity	Av.	0.08	0.80
	Max.	0.15	0.75
Platform Pitch	Av.	-0.99	0.40
	Max.	-0.86	0.44

The results support the findings from subsection 6.6.1, showing high absolute values of correlation coefficients between the average thrust force and mooring line tension, absolute tower base bending moment, and platform pitch. This indicates a strong dependence of these parameters on wind loads and a weaker influence of wave loads. The negative correlation coefficient for platform pitch implies the inverse relationship, suggesting that when wind loads increase, the platform turns further away from the wind. In contrast, for absolute nacelle acceleration and velocity, clear positive correlations are observed with significant wave height for both the average and maximum values. The low correlation with the average thrust forces indicates that these parameters are more dependent on wave loads than on wind loads.

6.7 Summary - Complex System Control

This section provides an overview of the complex control system implemented to not only regulate power extraction but also suppress excessive system movements. Analyses of the ramp-up and shut-down stages reveal the high dependency of rotor thrust on both, rotor angular velocity and blade pitch. Furthermore, the analysis of wave resonance phenomena suggests that load RAOs have a greater influence than displacement RAOs under the considered environmental conditions, as the former peak at wave periods of interest while the latter do not. Overall, resonance phenomena significantly affect absolute nacelle acceleration, velocity, tower base bending moment, and floater pitch. However, resonance effects on mooring line tension are of lesser significance. Additionally, it is observed that local parameters like absolute nacelle acceleration and velocity are more dependent on wave loads, while global parameters such as platform pitch, absolute tower base bending moment, and mooring line tension are mainly influenced by wind loads. Moreover, wind loads primarily manifest through thrust force rather than the wind speed. Notably, around the rated wind speed, the importance of wind loads for absolute nacelle acceleration and velocity increases. This suggests that the control system plays a role in influencing how output parameters are affected by environmental loads.

7 MODELLING SENSITIVITY ANALYSIS

7.1 Introduction

This section is dedicated to model enhancements available within *OrcaFlex* for the modelling of FOWTs. Figure 29 displays the various fields of interest explored in the research. The primary objective is to establish a foundation of knowledge to develop a simplified model in section 8. Therefore, simplified aerodynamics and rotor structural dynamics are the main focus. Results for mooring line dynamics and structural tower dynamics are not included in this paper, but available upon request from the author.
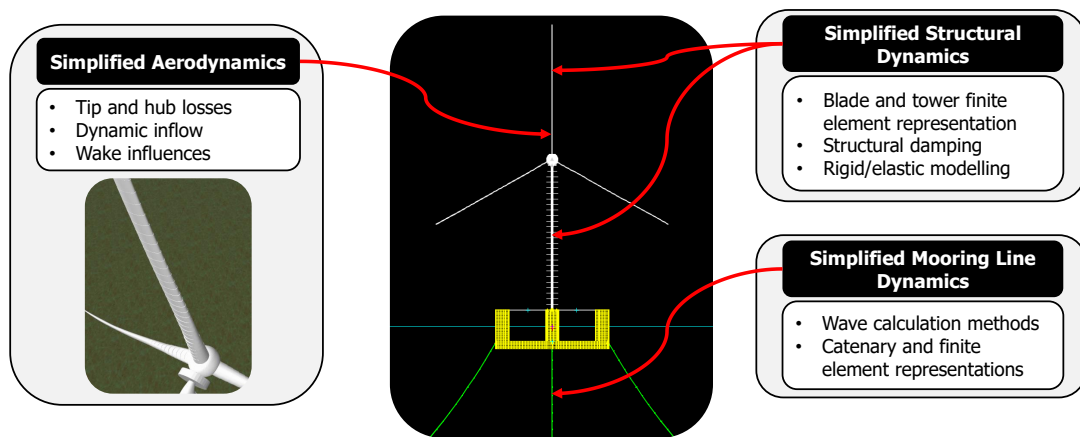
Figure 29: Domains of interest for the modelling sensitivity analysis of FOWTs

The objective is not an exhaustive quantitative analysis but rather a qualitative understanding of the enhancements' impact on simulation time and result accuracy. The reference model, while validated against prototypes and similar software, provides a global representation of the wind turbine's dynamics, lacking the intricacies of specific expertise areas. For instance, the BEMT method used for rotor aerodynamics offers reasonable estimations but may not fully account for complex aspects like wake effects. To conduct a quantitative assessment, detailed local approaches such as CFD would be required. However, this level of analysis is beyond the scope of this thesis. Therefore, this study focuses on introducing the model enhancements and providing a qualitative analysis of their influence on simulation outcomes.

7.2 Turbine Aerodynamic Model Enhancements

As explained in section 4.3.4, *Blade Element Momentum Theory* is used to calculate aerodynamic loads applied to the turbine. A comprehensive explanation of the theory underlying BEMT

and the derivation of its governing equations is given in appendix A.5. Furthermore, its implementation within *OrcaFlex* is explained in appendix A.6. The impact of integrating aerodynamic model enhancements on the dynamics of the FOWT is investigated. The theoretical background of these enhancements is provided in appendix A.7.

7.2.1 Numerical Modifications

A total of six turbine models are compared in this analysis. The first model represents the base case, including all aerodynamic model enhancements. The subsequent four models exclude one of the specific aerodynamic model enhancements discussed in appendix A.7, namely tip loss, hub loss, dynamic inflow, and skewed wake corrections. Lastly, the sixth set of simulations modifies the BEMT model approach by neglecting the tangential induction factor ($a' = 0$), which is defined in appendix A.6.

7.2.2 Results

Results show that the inclusion or exclusion of most aerodynamic model enhancements does not significantly impact the simulation time or the output parameters defined in section 5.3. However, the exclusion of the dynamic inflow enhancement leads to more noticeable differences, particularly for absolute nacelle acceleration and velocity. For load cases 4, which correspond to wind speeds around the rated wind speed, the average values of absolute nacelle acceleration are underestimated by almost 5%. Additionally, the standard deviation and maximum values are underestimated by 7.5% and 11.7%, respectively. These discrepancies suggest that the dynamic inflow model enhancement plays a crucial role in accurately predicting local effects, such as nacelle acceleration and velocity, especially in critical operating conditions. Simulation time and output parameters related to more global effects, such as platform pitch and mooring line tension, remain relatively unaffected by the exclusion of the dynamic inflow model enhancement.

7.3 Rotor Structural Dynamics

In *OrcaFlex*, the rotor is modelled using a finite element representation, the complexity of which is shown in appendix B.1.3. In preparation for further simplifications in section 8, this subsection aims to understand the potential deviations that may arise from using a simplified model. Theoretical background is available in appendix A.8

7.3.1 Numerical Modifications

To simplify modelling of the blades, two approaches are taken. In the first simplification, the structural damping of the blades is neglected. In the second simplification, both the structural damping and blade deformations are disregarded by treating the blades as rigid beams. This is accomplished by excluding the degrees of freedom associated with the blade nodes from the dynamic calculations.

7.3.2 Results

The analysis begins with an examination of simulation time. By modelling the blades as rigid, an average simulation time reduction of almost 25% is achieved, and excluding the effects of blade damping results in an average reduction of 22.5%. Whereas for the simulations with rigid blades, simulation time is almost independent of the environmental load cases, strong fluctuations are observed for the simulations excluding the effects of structural blade damping. Special attention should be paid to load case 9, where the duration of the simulation without the effects of blade damping even exceeds the simulation duration of the reference model.

The impact of excluding structural blade damping on output parameters selected in section 5.3 is examined. It is found that most of the selected parameters show no significant differences compared to the reference model. The relative differences in their averages, maximum values, and standard deviations are all below 0.2% on average. However, notable discrepancies are observed in the case of absolute nacelle acceleration, particularly for load cases 9 and 10, as illustrated in figure 30.
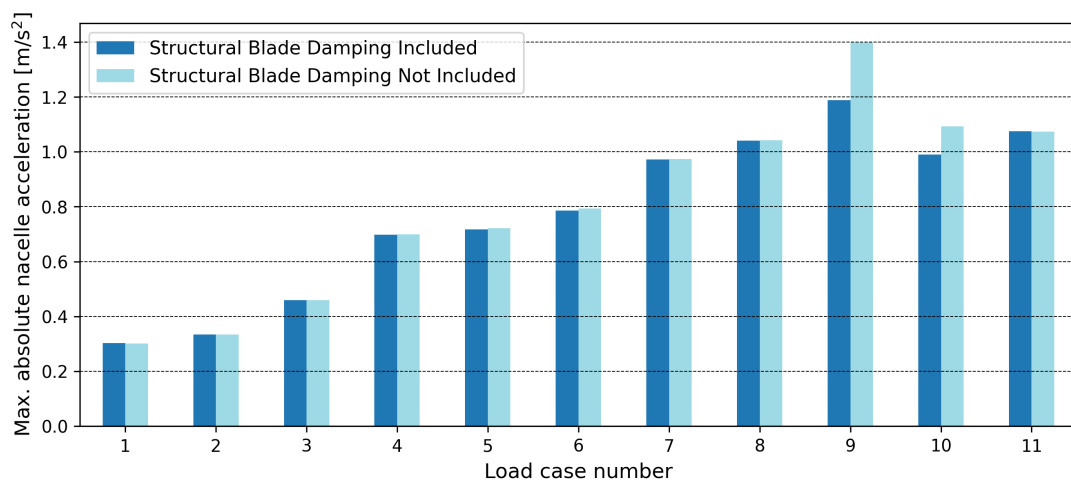
Figure 30: Maximum absolute nacelle acceleration with and without structural blade damping

For load case 9, an overestimation by almost 18% is observed. It can be explained by examining the rotor's absolute angular acceleration, as shown in figure 31. The appearance of peaks is explained through the theoretical background given in appendix A.8.1, which highlights that structural damping is utilised to dampen out spurious oscillations that arise in the high-frequency domain. The exclusion of structural damping in the simplified model leads to computational instabilities at certain frequencies in the blades, resulting in peaks in the angular acceleration. These peaks directly translate into nacelle acceleration and account for the observed overestimations of maximum values.
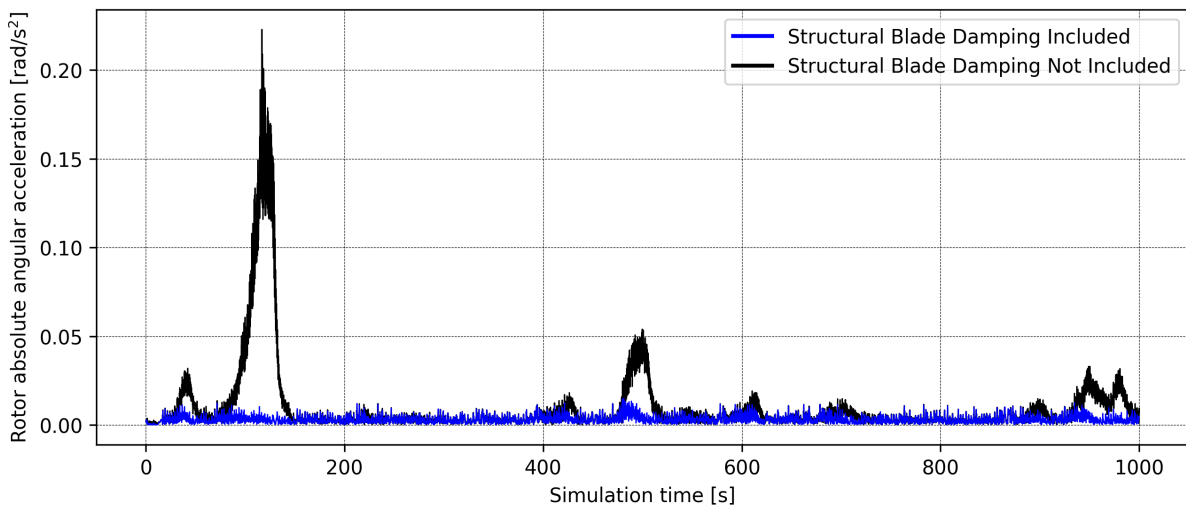
Figure 31: Rotor absolute angular acceleration with and without structural blade damping for the first 1000 seconds of load case 9

Modelling blades as rigid bodies leads to significant differences compared to the reference model, particularly for the absolute tower base bending moment. Comparing the average and standard deviation determined for the different load cases with those of the reference model, the average relative differences are 13% and 14%. As defined in section 6.6, the tower base bending moment is highly dependent on wind loads and, specifically, the rotor thrust force. Further analysis of the thrust force reveals that the aerodynamic load estimations differ significantly between the two models. In Figure 32, it is evident that the simplified model exhibits an average thrust force overestimation, especially for lower load cases, with a peak overestimation of 14% observed in load case 4. Additionally, for higher load cases, the simplified model predicts significantly higher blade pitch angles than the reference model. Consequently, this overestimation of blade pitch leads to an underestimation of thrust forces. Load case 9 is of particular interest. The simplified model overestimates the blade pitch angle to an extent that simulates a rotor shut-down, an event not observed in the reference model.

53
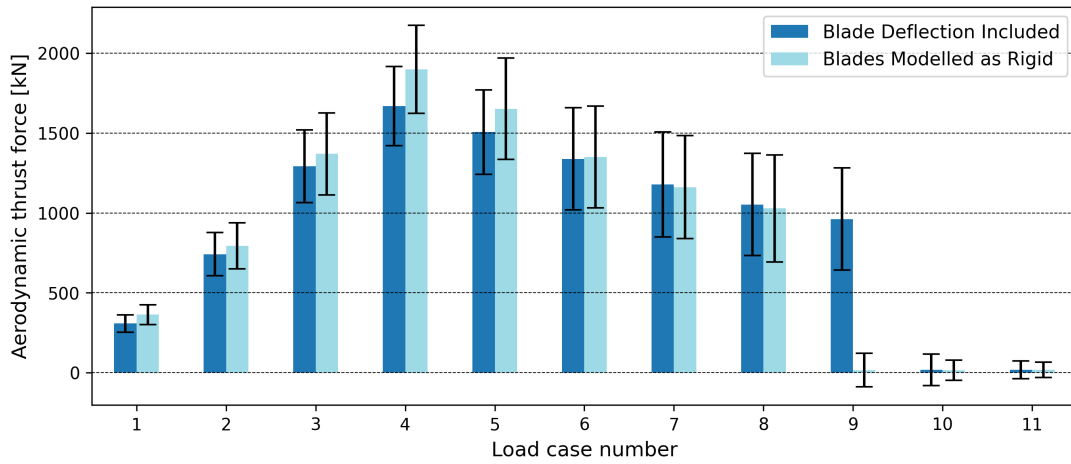
Figure 32: Average and standard deviation of aerodynamic thrust for rigid and deflectable blades

The impact of changing structural dynamics on wave resonance effects is examined. Regular waves with varying periods are applied onto the simplified model and the maximum values of output parameters are compared to results from the reference model, given in section 6.5. It is found that, except for the absolute nacelle acceleration, no significant differences are observed. In figure 33 the peak in absolute nacelle acceleration is still visible for the same wave period, but with an amplitude almost 10% higher. Combining results from figure 32 and 33 demonstrates the intricate relationship between structural properties of the blades, aerodynamic forces, and hydrodynamic resonance phenomena, highlighting the overall complexity of the system.
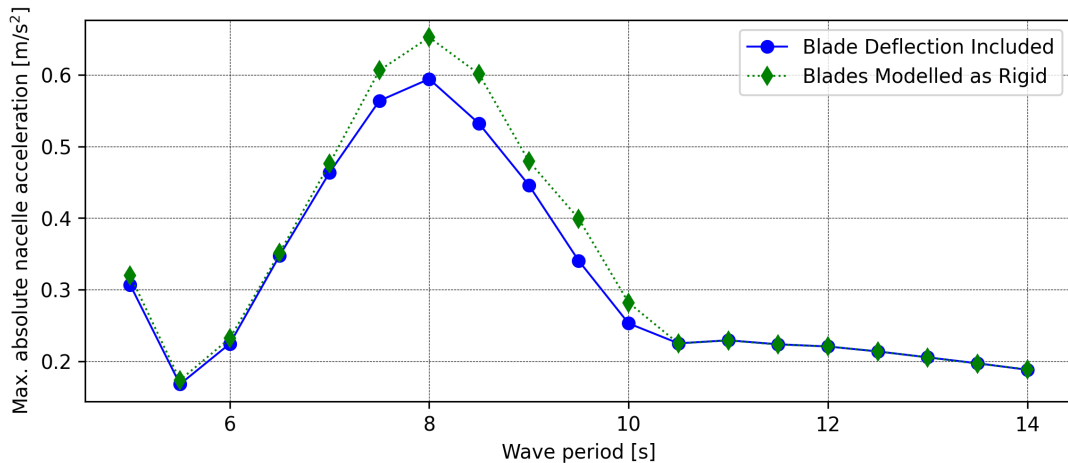
Figure 33: Maximum absolute nacelle acceleration for models with rigid and deflectable blades for different wave periods

7.4 Conclusion - High Interconnectivity of Domains

In conclusion, this section demonstrates that even the exclusion of minor parameters can significantly influence system dynamics. The impact of aerodynamic model enhancements is relatively small, with the highest influence observed around the rated wind speed. Analysing structural blade damping reveals its impact during loading conditions where computational instabilities lead to high-frequency oscillations. The inclusion of structural damping effectively mitigates instabilities, resulting in notable effects on average and maximum nacelle acceleration. Care must be taken when performing simplifications to avoid overlooking such local effects, exhibiting considerable impacts solely under specific excitation, notably load cases 9 and 10 in this study. The exclusion of blade damping leads to a considerable reduction in calculation time for the load cases in which it does not induce oscillations. Modelling blades as rigid beams further enhance computational efficiency. However, these simplifications come at the cost of reduced accuracy, illustrating the trade-off between computational speed and precision. This compromise is reflected in the disparities observed not only in the average values but also in the standard deviations of the selected output parameters.

The key finding of this section underscores the profound interconnection among various domains. Modifying the structural modelling of blades and representing them as rigid beams directly affects the aerodynamic forces acting on the rotor. Moreover, the interplay between hydrodynamics and structural dynamics is shown, as illustrated by the changes in resonance effects when structural modelling is altered. These insights indicate that future simplifications in the rotor representation are likely to have broad-ranging effects, impacting not only local dynamics but also influencing the overall behaviour of the entire structure.

8 SIMPLIFIED ROTOR REPRESENTATION

8.1 Introduction

To optimise computational resources and reduce simulation time, a significantly simplified model of the floating offshore wind turbine is developed. This section investigates the model's ability to capture the turbine's dynamic behaviour. The simplified model involves substituting the turbine rotor with a three-dimensional mass element possessing the appropriate inertial characteristic, in terms of the position of the centre of gravity, the mass and the second moment of inertia. A force is then applied to this mass element to represent the thrust generated by wind forces. Figure 34 illustrates the conceptual representation of this simplified model.
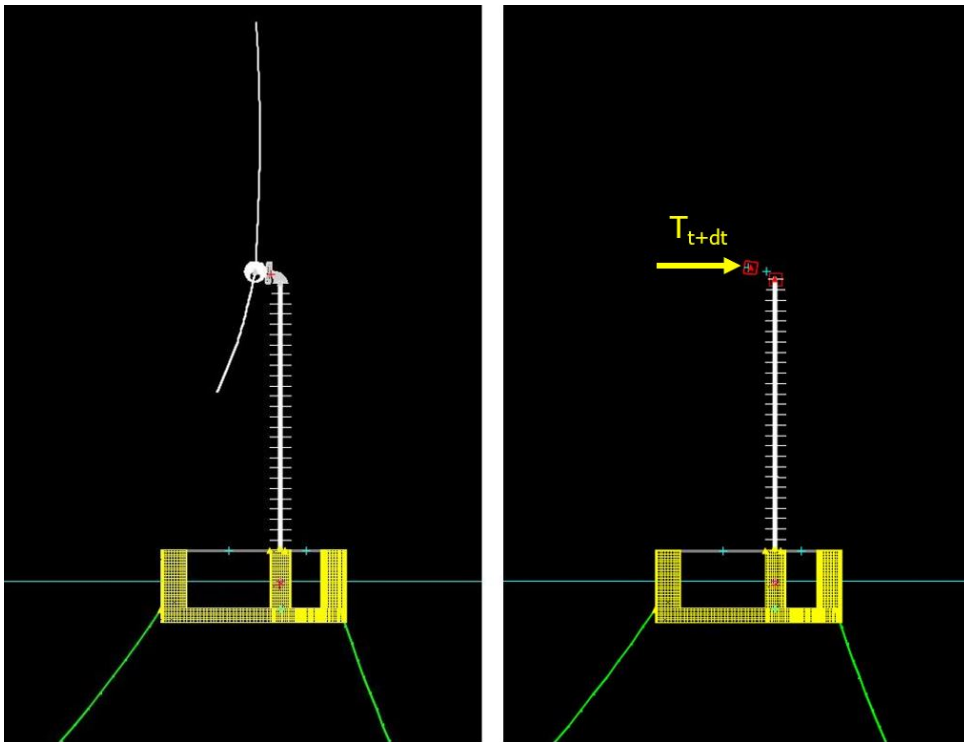
Figure 34: Representation of the reference and simplified FOWT in *OrcaFlex*

The floating substructure, mooring lines, tower, and nacelle properties in the simplified model remain identical to those of the reference model. The buoy representing the rotor incorporates the mass and mass moments of inertia of both the hub and blades, with its centre of gravity located at the same position. The assumption is made that the gyroscopic effect resulting from the combination of blade rotation and pitch or yaw movements of the structure can be disregarded. The surface area of the 3D element representing the rotor and the nacelle is considered negligible, as it is assumed that all wind loads are already accounted for within the thrust force.

8.2 The General Principle for Thrust Calculation

The fundamental principle underlying the estimation of thrust loads can be comprehended by referring to figure 35. The approach involves extracting the wind velocity at the hub height from the dynamic simulation and using a predefined relation between thrust and incident wind speed to determine the aerodynamic forces. Since this relationship is established based on discrete data points, a linear interpolation is employed. To account for effects such as rotor ramp-up or shut-down, modifications must be applied to this thrust force. The *Python* code used to perform this conversion can therefore be seen as a transfer function that converts a wind speed into a force.
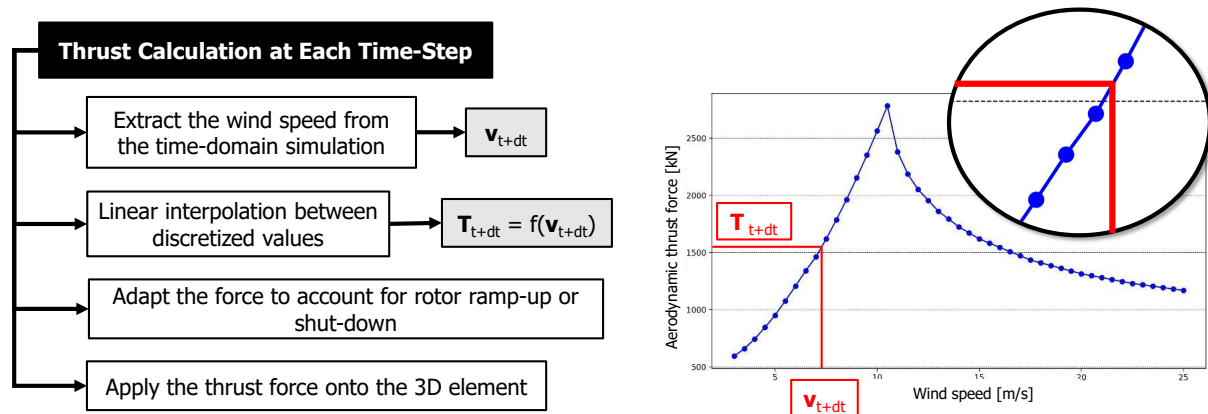
Figure 35: The fundamental concept behind determining the magnitude of thrust loads at each time step

8.3 Databases with Discrete Values

The importance of having databases containing discrete values for rotor thrust becomes apparent when examining the concept presented in figure 35. For the advanced model, databases are necessary not only for aerodynamic thrust but also for blade pitch and aerodynamic torque, as discussed in section 8.4.

8.3.1 Creation of a Database for the Rotor Thrust

A database for rotor thrust is created through a 30-minute simulation of the reference FOWT. The simulation involves a gradual increase in wind speed, while no current or wave loads are applied. The resulting aerodynamic thrust force experienced by the rotor is shown as the blue line in figure 36. Utilising the complete FOWT model allows for the consideration of complex dynamic phenomena. Notably, at both low and high wind speeds, the thrust force approaches

57

zero due to rotor start-up and shut-down, as explained in section 6.4. Additionally, in region 3 above the rated wind speed, the thrust force exhibits important oscillations around a trendline.
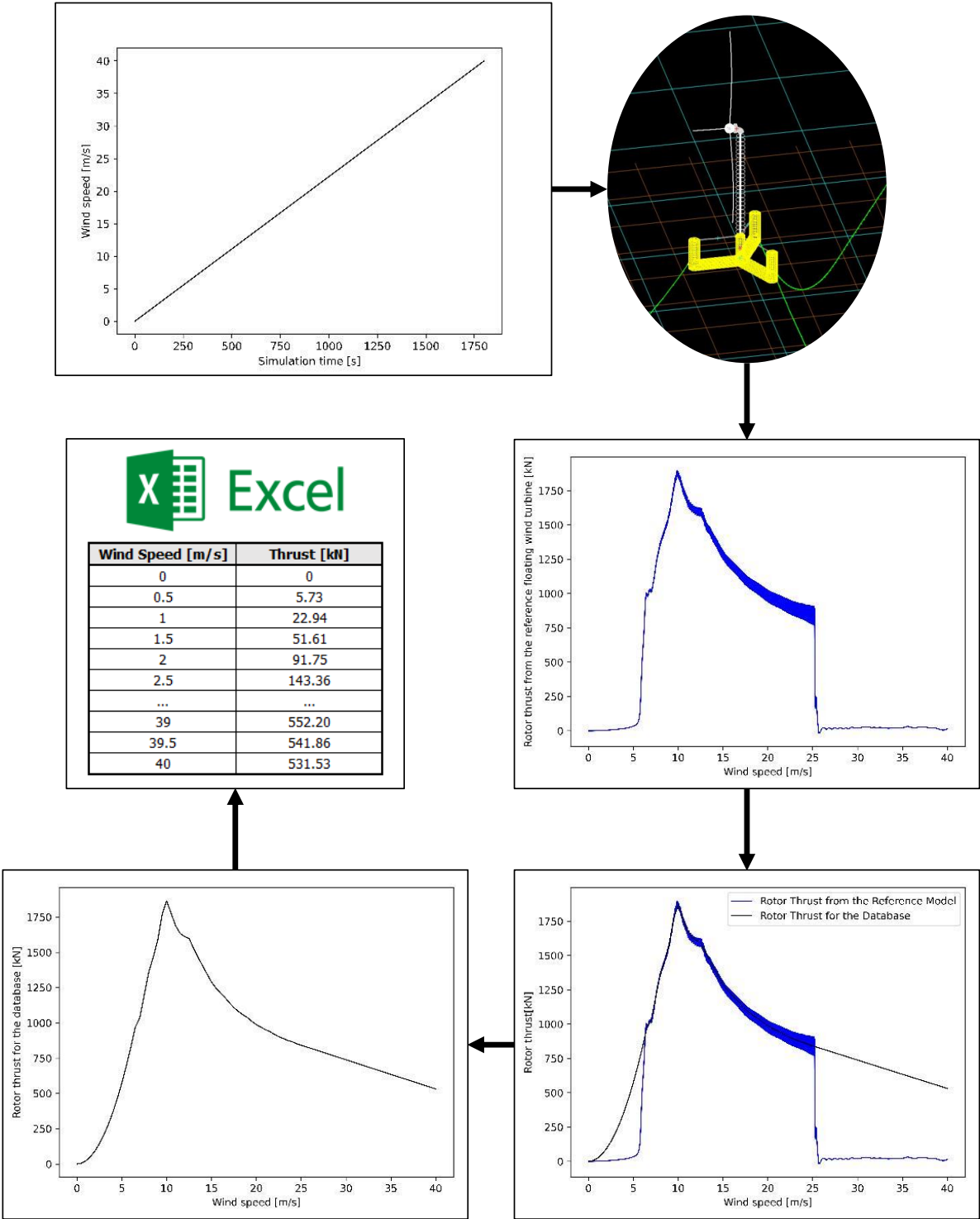
Figure 36: Creation of a database for the rotor thrust

The observed oscillations in the rotor thrust can be attributed to the rotation of the blades, as

extensively discussed in section 8.5.3, with a particular focus on figure 44. It is shown that maximum thrust forces occur when one of the blades is pointing upwards, while the configuration with one blade pointing downwards is associated with the lowest thrust forces. The frequency of these oscillations is therefore three times higher than the rotational frequency of the rotor. The values extracted for the rotor thrust database are represented by the black line in figure 36 and are provided in table 12 in appendix C.5.1. The thrust is discretised for wind speeds ranging from 0 to 40 m/s in steps of 0.5 m/s. For wind speeds v_w between 6.5 and 25 m/s, the discretised values are obtained by averaging the thrust within the interval $[v_\mathrm{w} - 0.25, v_\mathrm{w} + 0.25]$. For wind speeds below 6.5 m/s, the thrust is approximated assuming a second-order relation with the wind speed, inspired by results presented in equation (21). Above the cut-off wind speed of 25 m/s, the thrust is simply approximated linearly with the same slope as at 25 m/s. However, it should be noted that values above this rated wind speed are of minimal significance since operation in this region occurs only for brief periods. If wind speeds remain too high for an extended duration, the blade pitch exceeds its maximum value, triggering a rotor shutdown.

8.3.2 Creation of a Database for the Blade Pitch and Aerodynamic Torque

The aerodynamic torque and blade pitch are utilised for modelling the ramp-up and shut-down of the wind turbine, respectively, as explained in section 8.4. Unlike the thrust force, they are not directly applied as inputs to the model but are used to adjust the thrust in these two regions. When constructing the thrust force database, the dynamic behaviour of the floater is taken into account. Conversely, for the torque and pitch databases, a focus on the internal turbine control is desired, disregarding global system dynamics. Therefore, wind loads are applied to the wind turbine model with a fixed hub position. During the simulation, wind speeds are linearly increased from 0 to 40 m/s. From this simulation, values for blade pitch and aerodynamic torque are extracted. Plotting rotor torque as a function of wind speed in figure 37 exhibits a distinct trend. Initially, the torque increases steadily and reaches a plateau around 12.5 m/s, where significant oscillations occur. Beyond the cut-off wind speed, torque rapidly decreases and eventually reaches zero.

As for rotor thrust, these oscillations result from rotor rotation. The torque database is formed using a similar averaging process as for rotor thrust for wind speeds above 12 m/s. However, for lower wind speeds, this approach yields unsatisfactory results. Therefore, an alternative method is employed, which involves conducting additional simulations. These simulations involve applying a constant wind for a duration of 600 seconds. Each wind speed ranging from 0 to 12

Figure 37: Aerodynamic torque as a function of the wind speed

m/s is simulated with a step size of 0.5 m/s. The simulations converge to a steady value around which oscillations occur. The resulting torque database is provided in table 14 in appendix C.5.3. In the "plateau" region, the torque is approximated as a constant value. Above the cut-off wind speed, the torque is assumed to be zero. While this assumption may not perfectly align with the physical behaviour, it is considered acceptable since the aerodynamic torque is solely used for the ramp-up procedure. If the cut-off wind speed is exceeded, the turbine will not be ramped up, making the aerodynamic torque irrelevant. For the blade pitch, a similar approach is utilised with the results provided in table 13 in appendix C.5.2.

8.4 External Python Code for Thrust Calculation

In the subsequent section, the *Python* code called upon by the dynamic model is examined in detail. It includes an initialisation step that is executed only once at the start of each simulation, and a core section that is invoked at the beginning of every new time step.

8.4.1 Initialisation

Figure 38 below provides a schematic view of the initialisation step, which is only utilised once at the start of the simulation. The code reads the Excel files containing the database of thrust, pitch, and torque values. These values are then stored in the system memory in matrix form for

the entire duration of the simulation. Furthermore, during this initialisation step, the blade pitch (β) and rotor speed (ω) are set to zero. Additionally, a stage variable is initialised to 0, indicating the current stage of the thrust calculation being the rotor ramp-up.
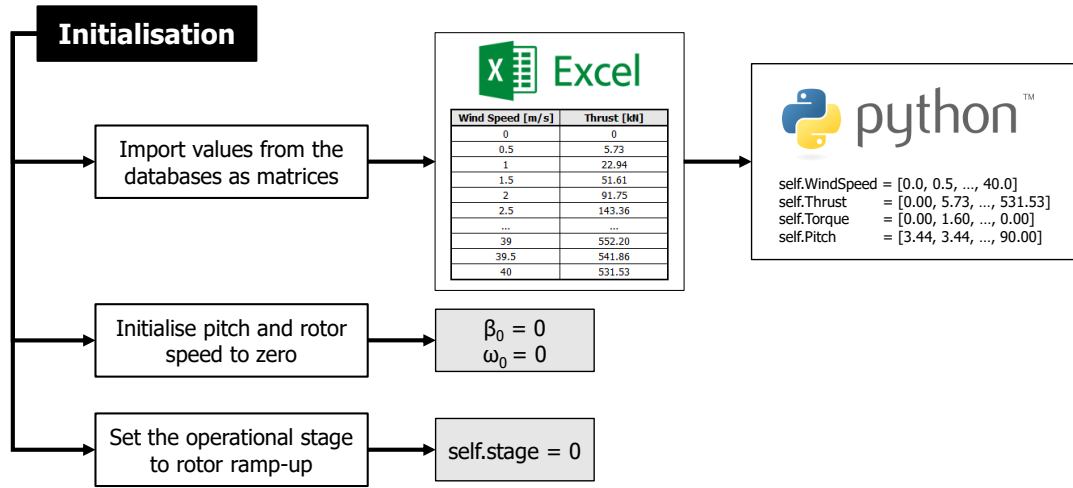
Figure 38: Initialisation step for the thrust calculation code

8.4.2 *Thrust Calculation at each Time-Step*

At each time-step, *OrcaFlex* calls upon an external *Python* code, described in figure 39, to compute the aerodynamic thrust force. At the beginning of each time-step, the wind speed experienced by the rotor is extracted from the dynamic time-domain model. Using the database imported during the initialisation phase and employing linear interpolation, the reference values for blade pitch and aerodynamic thrust, denoted as β_{ref} and T_{ref} respectively, are computed based on the corresponding wind speed. Subsequently, the blade pitch is adjusted by updating its value. The adjustment is based on the difference between the reference pitch β_{ref} and the pitch value from the previous iteration β_t. This difference, denoted as Δ_β, is compared to a maximum increment value defined in the turbine properties Δ_{max} to ensure that the pitch variations remain within a feasible range. If the blade pitch surpasses a specified threshold β_{max}, the stage variable is updated to indicate the turbine's transition into the shutdown mode. Simulations for different thresholds are compared to determine the one that achieves rotor shutdown at wind speeds comparable to the reference model. In normal operation (stage variable = 1), the thrust force is simply set to the reference thrust T_{ref}, previously extracted from the database. In ramp-up or shut-down stages, additional modifications are made to the reference thrust force to accommodate changing operational conditions during these transitions.
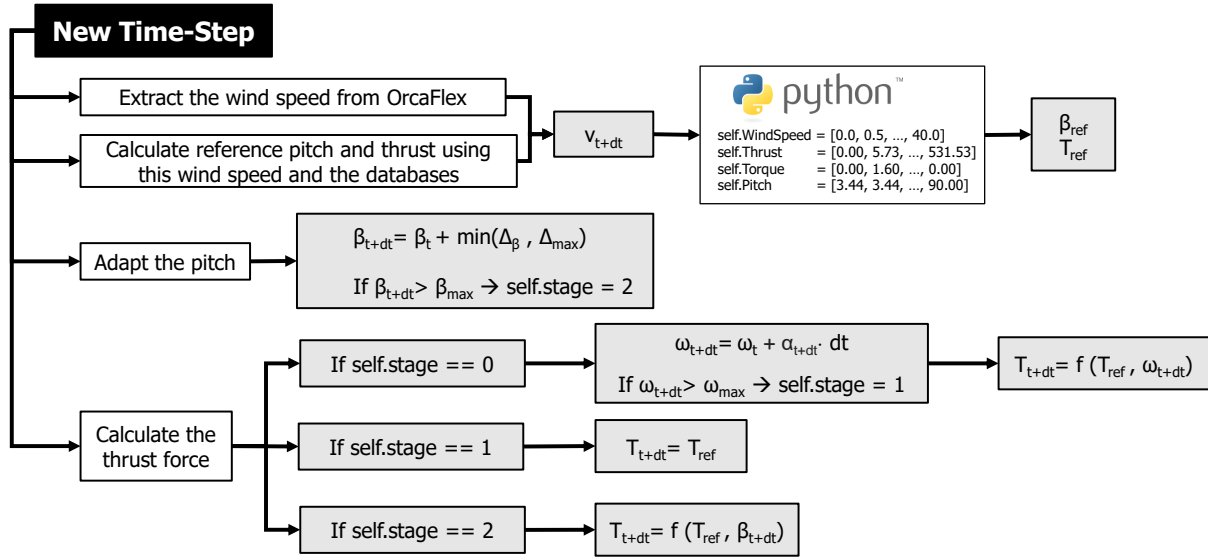
Figure 39: Algorithm for the calculation of the aerodynamic thrust force at each time-step

8.4.3 The Ramp-Up Stage

The stage variable, when equal to zero, indicates that the rotor is being accelerated from a stand-still to an operational configuration. As explained in 8.4.1, all simulations start from such an idle configuration with the initial angular velocity ω_0 set to zero. Following figure 40 illustrates the sequential steps involved in this ramp-up stage.
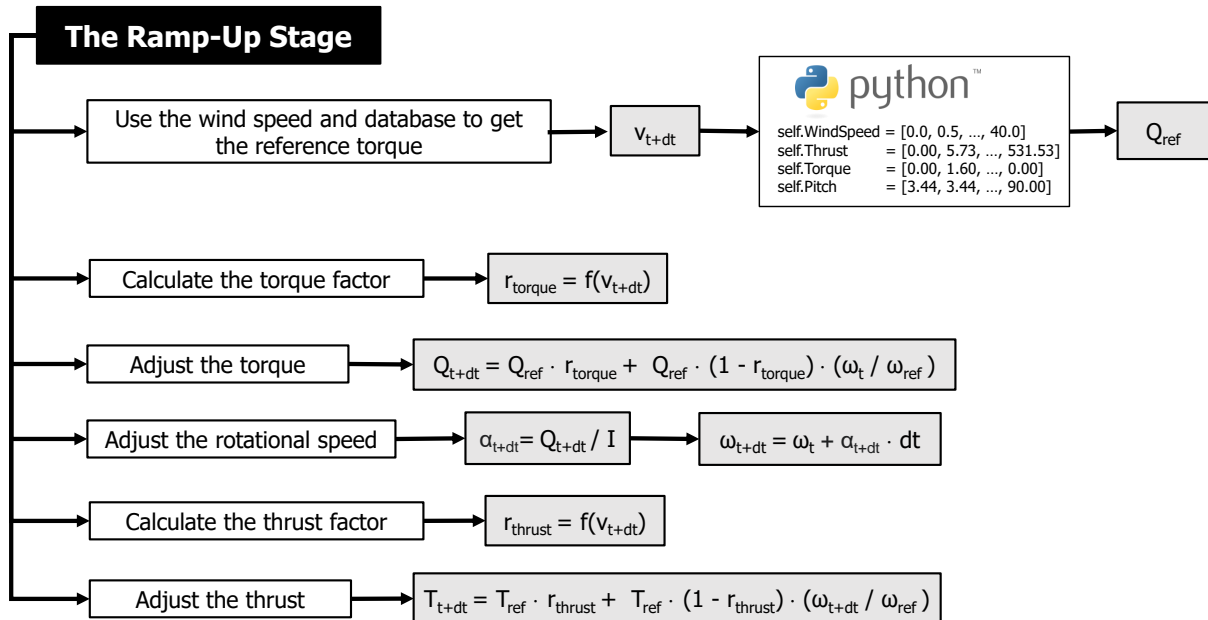
Figure 40: Algorithm for the calculation of the thrust force in the ramp-up stage

In a first step, the torque database and the wind speed are utilised to calculate the torque reference value, represented as Q_{ref}. Subsequently, a torque factor denoted as r_{torque} is determined,

the analytical expression and physical interpretation of which can be found in appendix B.2. Furthermore, appendix B.2.1 explains the relationship between the aerodynamic torque and the rotor rotational speed ω_t. This relationship is assumed to be linear, based on the expression given in equation (28). Consequently, the torque Q_{t+dt} is calculated using equation (10) below, where ω_{ref} represents the rotational speed at which the rotor enters into operational mode.

$$Q_{t+dt} = r_{\text{torque}} \, Q_{\text{ref}} \; + \; (1 - r_{\text{torque}}) \, Q_{\text{ref}} \, \left(\frac{\omega_t}{\omega_{\text{ref}}} \right) . \tag{10}$$

Next, the rotor speed ω is updated using the rotor angular acceleration α, which is determined by dividing the rotor torque Q by the rotor moment of inertia I. (dt represents the time-step utilised in the implicit solver of the dynamic model.)

$$\begin{cases} \alpha_{t+dt} = \frac{Q_{t+dt}}{I} \\ \\ \omega_{t+dt} = \omega_t + \alpha_{t+dt} \, dt \end{cases} \tag{11}$$

In a final step, rotor thrust is calculated. The expression shown in equation (12) is chosen based on observations from the reference model, which reveals a predominant linear relationship between the thrust and rotor speed, as determined in section 6.4.1. For instance, in the rotor ramp-up stage for the simulation with the second load case, a high Pearson correlation coefficient of 0.97 is observed between these two variables, indicating strong linearity. Similar to the torque, a thrust coefficient denoted as r_{thrust} is introduced to account for the portion of thrust that remains independent of rotor speed. Further explanation about this factor is given in appendix B.2.2 and it is used in the final expression of the rotor thrust as:

$$T_{d+dt} = r_{\text{thrust}} \, T_{\text{ref}} \; + \; (1 - r_{\text{thrust}}) \, T_{\text{ref}} \, \left(\frac{\omega_{t+dt}}{\omega_{\text{ref}}} \right) . \tag{12}$$

8.4.4   The Shut-Down Stage

When the wind turbine surpasses a predefined threshold β_{max}, it enters the shut-down stage, as described in section 6.4.2 and implemented in figure 39. The thrust value T_{sd} at which this transition is observed is retained. At each iteration, the estimated thrust after shut-down, denoted as T_{IV}, is calculated using the relationship:

$$\begin{cases} r_{\text{IV}} = 0.003 \cdot \text{v}_{t+dt} - 0.048 \\ \\ T_{\text{IV}} = T_{\text{ref}} \cdot r_{\text{IV}} \end{cases} \tag{13}$$

Here r_{IV} is a coefficient indicating the percentage of thrust experienced after the turbine shutdown. Through observation of results from simulations using the reference turbine, a linear relation between this coefficient and the wind speed v_{t+dt} is assumed and the analytical formula given in equation (13) is obtained. The thrust value at the next time step, denoted as T_{d+dt}, is then determined using the following expression based on the current blade pitch angle β_{d+dt}:

$$T_{d+dt} = T_{\text{sd}} + (T_{\text{IV}} - T_{\text{sd}}) \cdot \left(\frac{\beta_{d+dt} - \beta_{\text{max}}}{\beta_{\text{IV}} - \beta_{\text{max}}} \right) . \tag{14}$$

β_{IV} corresponds to the blade pitch angle after complete shutdown. Since the turbine is stopped applying blade feathering, as described in section 6.4.2, β_{IV} equals 90 degrees.

8.4.5 Application of Loads

OrcaFlex provides two options for applying the load to the three-dimensional element that replaces the rotor: global load and local load. The global load is aligned with the global axes of the model, while the local load is aligned with the local axes of the element. If the 3D element undergoes rotation, the local loads will rotate accordingly, whereas the global loads will maintain their fixed orientations. Although the magnitude of the applied force is the same for both local and global loads, the use of global loads leads to significant differences compared to the reference model and to an underestimation of the dynamic effects. On the other hand, applying local loads yields much better results and is therefore used to apply the calculated force.

8.5 Results

In accordance with the discussion in section 5.4.3, simulations with a length of 2 hours are performed to ensure statistically reliable comparisons.

8.5.1 Simulation Time

It is found that the simplified model offers an 82.7% reduction in average simulation time compared to the reference model, decreasing it from 3 hours and 50 minutes to just 37 minutes. This significant reduction in simulation time allows for more simulations to be performed in less time, improving work efficiency.

Furthermore, when observing the required iteration per time step, it is seen that the simplified model requires no more than one iteration, while the reference model necessitates up to five

iterations. These findings suggest that the simplified model's time step may be unnecessarily small, and further reductions in simulation time can be achieved by increasing it. Indeed, increasing the time step from 0.025 to 0.05 results in an additional 48.43% reduction in average simulation time. However, beyond a time step of 0.1, the reduction in simulation time becomes less significant, as can be seen in figure 41. Using a time step of 0.1 seconds leads to an average simulation time of 10 minutes, which is a 95.4% decrease in computational time compared to the reference model's 3 hours and 50 minutes. Despite the relatively large time step, the simplified model requires no more than two iterations per time step for any simulation, whereas the reference model with a time step of 0.1 seconds already exceed 70 iterations per time step for some load cases. In the following, results for both time steps, 0.025 seconds and 0.1 seconds, are compared to investigate whether or not increasing the time step influences the system dynamics.
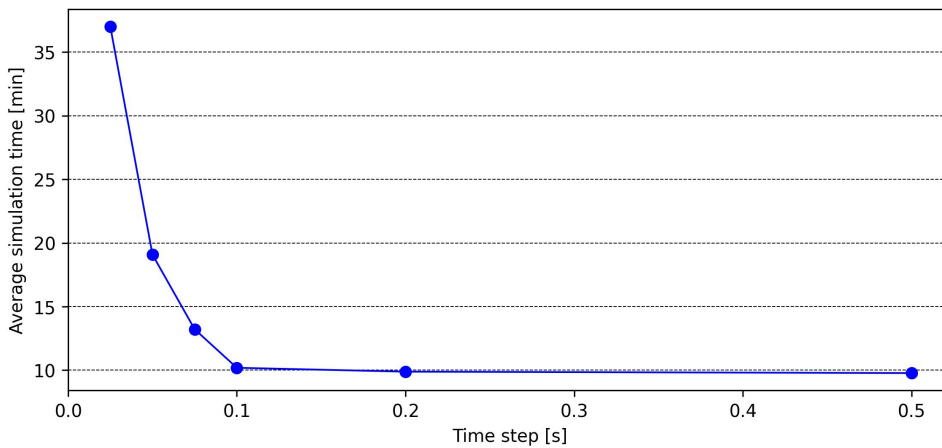
Figure 41: Variation of the average simulation time as a function of the time step of the implicit solver

8.5.2 Thrust Force

The estimation of the rotor thrust is examined for two different simplifications, utilising time steps of 0.025 and 0.1 seconds, respectively. The average and standard deviation of this force is compared to the aerodynamic thrust force calculated using *Blade Element Momentum Theory* (BEMT) for the reference turbine. Figure 42 presents the results for each load case, identified by its corresponding reference wind speed.

When examining the average rotor thrust, it becomes evident that the simplified model tends to overestimate the thrust for each load case. Table 8 presents the relative differences in average thrust values, denoted as Δ_{average}, between the reference model and the simplified model with a time step of 0.025 seconds. Notably, these relative differences are highest for smaller load cases,

65
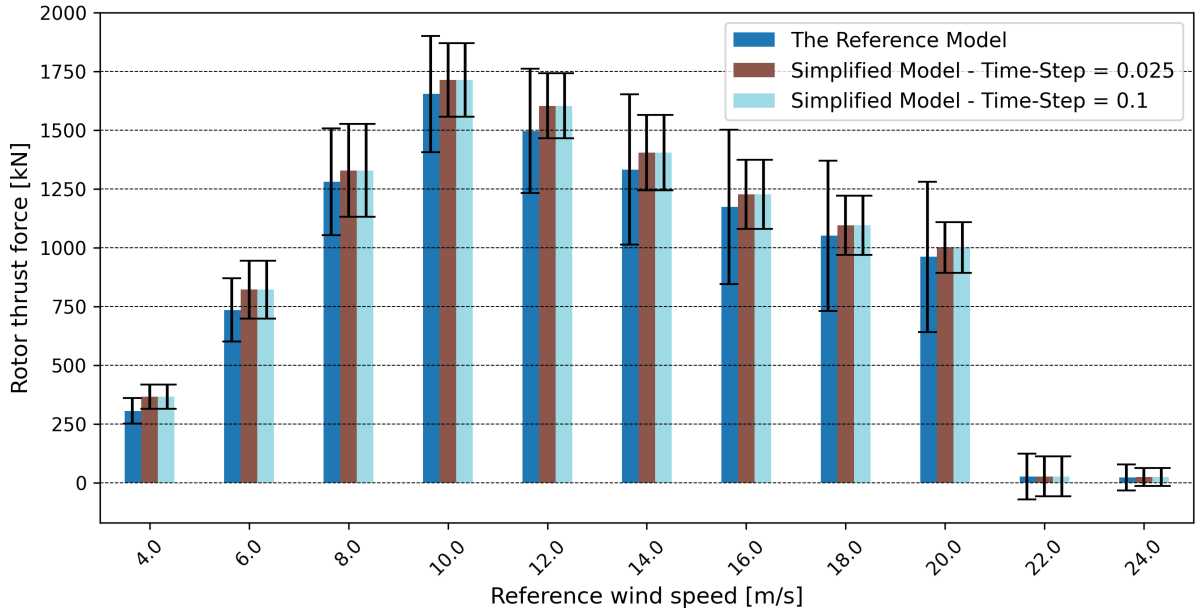
Figure 42: Average and standard deviation of the time-history of rotor thrust for all 11 load cases

indicating that the estimation of thrust forces for low wind speeds is less accurate. On average, the simplified model overestimates the thrust force by approximately 7%. Furthermore, figure 42 illustrates that there is no significant difference in average values between simulations with time steps of 0.025 and 0.1 seconds. This observation is further supported by quantifying the relative difference between these averages, which does not surpass 0.03% for any load case.

Table 8: Relative difference between the average rotor thrust (reference model) and applied force (simplified model with time step 0.025) for each load case

Load Case	1	2	3	4	5	6	7	8	9	10	11
v_{ref} [m/s]	4	6	8	10	12	14	16	18	20	22	24
$\Delta_{average}$ [%]	19.7	11.7	3.8	3.6	7.1	5.4	4.5	4.3	4.2	1.3	11.1

When examining the standard deviation, represented by the black error bars in figure 42, it is noteworthy that despite higher average values, the simplified model exhibits lower standard deviations and, consequently, reduced variations. To further investigate those disparities, the relative difference is calculated between the standard deviation of the rotor thrust for the reference model and the simplified model with a time step of 0.025, as presented in table 9. Notably, the underestimation of the standard deviation is most pronounced for higher load cases. Upon examining the absolute values, it is observed that variations for the reference model are highest above rated wind speed, while for the simplified model they peak below rated wind speed. Differences

66

for standard deviations between simplifications with different time steps are insignificant.

Table 9: Relative difference between the standard deviation of the rotor thrust (reference model) and the applied force (simplified model with time step 0.025) for each load case

Load Case	1	2	3	4	5	6	7	8	9	10	11
v_{ref} [m/s]	4	6	8	10	12	14	16	18	20	22	24
Δ_{SD} [%]	-3.8	-9.2	-12.8	-36.6	-47.6	-50.1	-55.1	-60.4	-66.1	-12.6	-30.1

To compare time-evolution of thrust forces between the reference and simplified models, Pearson correlation coefficients are computed. The results of the correlation analysis are presented in table 10, providing a direct comparison between the time histories of thrust values for the two models. Referring to the explanations provided in appendix A.9, it is observed that for lower load cases and cases where turbine shut down occurs (load cases 10 and 11), the correlation coefficients, denoted as $r_{ref-sim}$, are relatively high. This finding suggests that when one model exhibits a high (respectively low) thrust force, it is frequently observed that the other model also experiences a high (respectively low) thrust force. This aligns with expectations since both models encounter the same time-variations in wind speed. In contrast, load cases characterised by moderate wind speeds above the rated wind speed of 10.6 m/s exhibit coefficients with small absolute values, indicating the absence of correlation. In these cases, although the reference model and simplified model experience identical time-variations of wind speeds, the thrust forces exhibit different behaviour. The negative correlation coefficients observed for many higher load cases suggest that when one model experiences a high thrust force above the average, the other model most frequently exhibits a low thrust force below the average.

Table 10: Pearson correlation coefficient between rotor thrust (reference model) and applied force (simplified model with time step 0.025) for each load case

Load Case	1	2	3	4	5	6	7	8	9	10	11
v_{ref} [m/s]	4	6	8	10	12	14	16	18	20	22	24
$r_{ref-sim}$ [-]	0.80	0.71	0.67	0.47	0.10	-0.01	-0.08	-0.18	-0.24	0.87	0.67

In addition to comparing the two thrust forces, a correlation analysis between rotor thrust and wind speed is conducted and presented in terms of correlation coefficients in table 11. For the simplified model, a strong correlation between rotor thrust and wind speed is observed. Wind speeds below the rated wind speed (10.6 m/s) exhibit a positive correlation, while wind speeds above the rated value show a negative correlation, indicating an inverse relationship. For load

cases at which a shut-down occurs, correlation is positive again. These observations aligns with theoretical expectations, as thrust force is expected to peak at the rated wind speed and subsequently decrease if wind speeds further increase. After shut-down, blade pitch cannot further be adapted, therefore thrust forces increase again with wind speed. Two outliers are observed; at load case 4, which is close to the reference wind speed, and at load case 10, the first case where a shut-down occurs. They can be explained by the switch in configuration, changing from positive to negative correlation and vice versa.

When increasing wind speeds gradually in an incremental manner, allowing the turbine sufficient time to adapt to changes, this trend is also observed in the reference model, as depicted in figure 36. In reality, the turbine often lacks sufficient time to fully adapt to rapid fluctuations in wind speed due to system limitations, such as the response time of the blade pitch actuator. This delay in the turbine's response leads to a more complex adjustment of the aerodynamic thrust force. As a result, the correlation coefficients between wind speed and thrust force for the reference model are relatively low. Even for higher wind speeds, positive correlation coefficients are observed, indicating that wind speeds above the average are often accompanied by thrust forces above the average. This discrepancy in the correlation coefficient contradicts theoretical expectations, as thrust force is expected to decrease with increasing wind speed above the rated wind speed. The deviation from this theoretical expectation is attributed to the slower system adaptation, particularly the delayed adjustment of the blade pitch angle.

Table 11: Pearson correlation coefficient between rotor thrust and wind speed for each load case; for both the reference model (r_{ws-ref}) and simplified model with time step 0.025 (r_{ws-sim})

Load Case	1	2	3	4	5	6	7	8	9	10	11
v_{ref} [m/s]	4	6	8	10	12	14	16	18	20	22	24
r_{ws-ref} [-]	0.58	0.64	0.59	0.33	0.23	0.14	0.16	0.24	0.31	0.16	0.72
r_{ws-sim} [-]	0.96	1.00	1.00	0.35	-0.94	-0.99	-0.98	-0.98	-0.97	0.23	0.99

In summary, the average thrust forces calculated for both the simplified and reference models are very close, with a slight overestimation observed for the simplified model. However, it is observed that fluctuations are much higher for the reference model. The correlation analysis presented in table 10 reveals that correlation between the two thrust forces is only high for low load cases or load cases where rotor shut-down has occurred. Considering the turbine's operational regions discussed in section 6.2.1, it becomes apparent that when the turbine is controlled through blade pitch, significant discrepancies exist between the two thrust forces. However, for

lower load cases where the turbine is controlled through rotor speed, their behaviour correlates better. Regarding the simplified model, no significant differences between the thrust forces for time steps of 0.1 or 0.025 seconds are observed.

8.5.3 Rotor Behaviour at a Sudden Wind Gust

To observe the contrasting behaviour of the reference and simplified models and its implications on the thrust force, an additional simulation is conducted. The turbine is initially held in a stable configuration, with a constant incident wind speed of 20 m/s, and no wave or current loads applied. At 100 seconds, an instantaneous increase in wind speed to 24 m/s occurs, followed by a return to initial conditions at 200 seconds. Figure 43 illustrates the time evolution of the wind speed, as well as the rotor thrust, either applied as a force onto the simplified model or calculated using BEMT for the reference model. Additionally, the evolution of the blade pitch angle for the reference model is depicted.
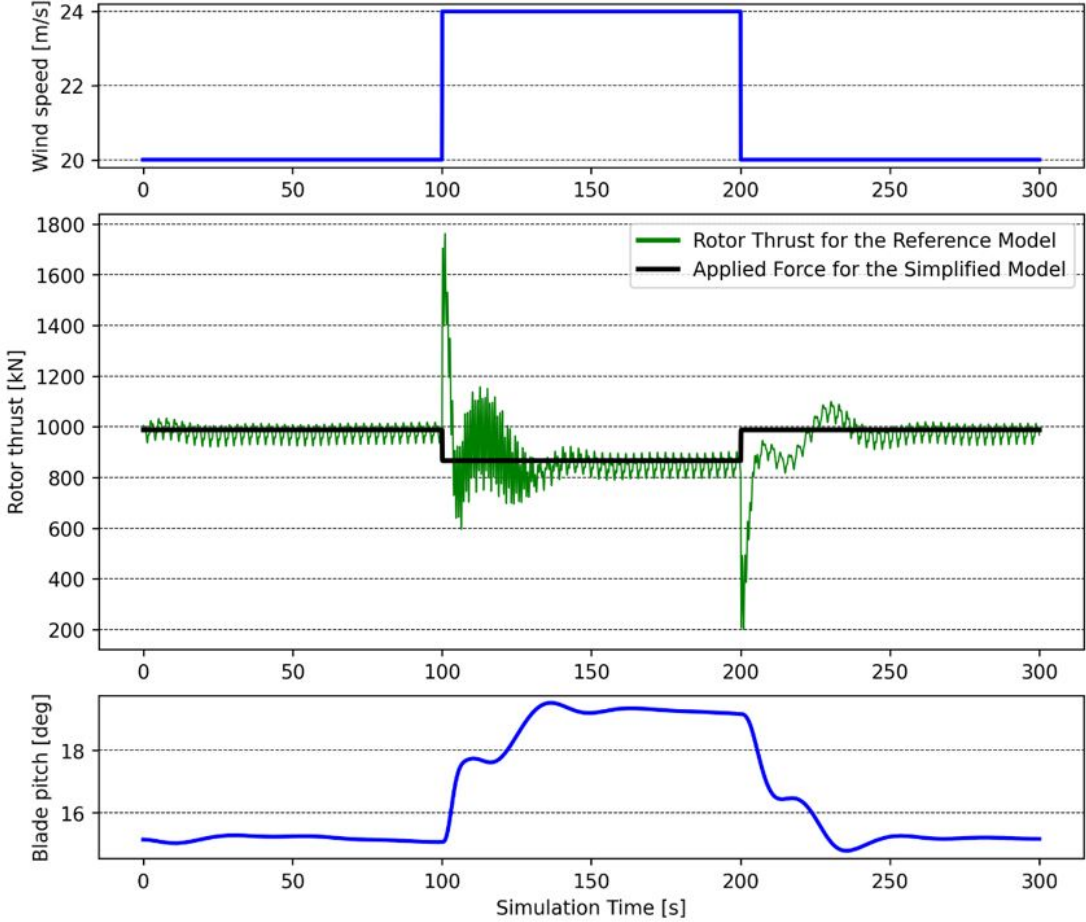
Figure 43: Wind speed, rotor thrust and blade pitch during a sudden wind gust

It is important to note that for the considered wind speeds, the turbine is controlled through blade

69

pitch adjustment. Prior to the sudden increase in wind speed, the blade pitch angle stabilises around 15 degrees. This value aligns with expectations based on the pitch database introduced in section 8.3.2. Furthermore, the database provides information on the blade pitch angle expected at a wind speed of 24 m/s, which is 19 degrees. However, upon increase in wind speed, the turbine does not instantaneously encounter the modified wind with the adapted pitch angle, as system adaptations require time. Consulting appendix A.5 with explanations about BEMT, it becomes apparent that due to the small pitch angle, the angle of attack of the wind on the blades is too low. Knowing that lift and drag coefficients are dependent on the angle of attack, employing equation (30) for thrust calculation reveals that the thrust forces are significantly higher at this lower angle of attack. These high thrust forces are observed in figure 43 as the peak in rotor thrust for the reference model immediately after the increase in wind speed. To counteract these high thrust forces and the accompanying high torque, the blade pitch is gradually increased. Consequently, the thrust force decreases, and the system undergoes fluctuations in thrust (and torque) to which the blade pitch is steadily adapted. The system eventually reaches a new equilibrium position after approximately 60 seconds, where blade pitch indeed is at a value of 19 degrees. When the wind speed undergoes its second instantaneous change back to initial conditions, a similar phenomenon occurs but in reverse. The blade pitch is too high for the encountered wind speed, leading to lower thrust forces. Again, the system requires approximately 60 seconds to adapt to this new configuration.

In contrast to the reference model, thrust adaptation in the simplified model is instantaneous, as indicated by the black line in figure 43. This instantaneous response, compared to the behaviour of the reference model, which requires time to adjust to changes in environmental conditions, is the primary reason for the observed differences discussed in section 8.5.2. With the rotor speed and the blade pitch, the rotor in the reference model possesses a "memory" that is not present in the simplified version. In other words, due to the rotor's inertia, implementing changes in the reference model requires time.

It is important noting that the rotor thrust in the reference model exhibits fluctuations even when environmental conditions are stable. These fluctuations can be attributed to the variations in rotor configuration. By plotting the time evolution of rotor thrust against the vertical position of the tips of the three blades, as shown in figure 44, it is observed that maximum aerodynamic thrust is achieved whenever the rotor configuration is such that one of the blades is on the verge of reaching its highest position, pointing upwards. Conversely, when one of the blades is point-

ing downwards, the rotor thrust is at its minimum. This dependency of thrust force on rotor configuration can be attributed to the vertical variation of wind speed caused by wind shear, as explained in appendix A.4. The simplified model, however, does not take into account these vertical variations but instead considers only the wind speed at the hub height. As a result, the simplified model does not exhibit the fluctuations observed in the reference model, which occur at a frequency three times higher than the rotational frequency of the rotor.
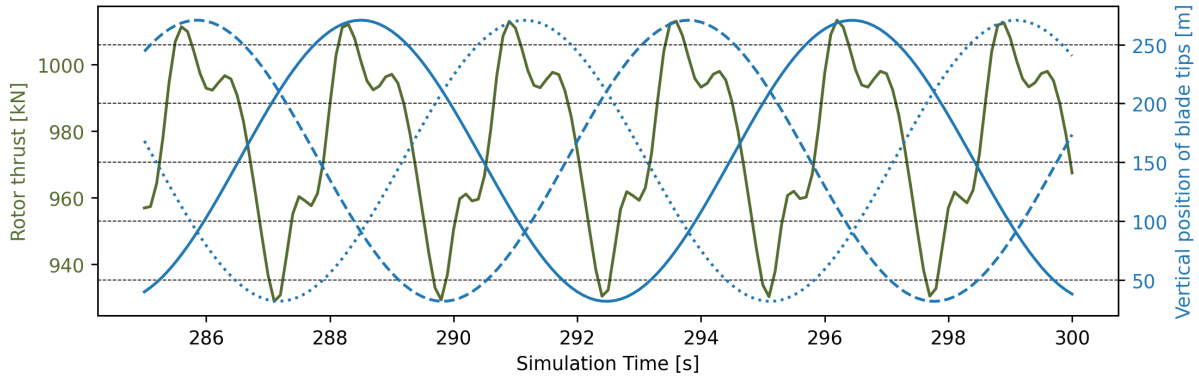
Figure 44: Time-evolution of rotor thrust and vertical position of blade tips for the reference model

8.5.4   *Absolute Tower Base Bending Moment*

In Section 6.6, the high correlation between tower base bending moments and aerodynamic thrust forces was established. This allowed the conclusion that the bending moments and subsequent stresses and fatigue loads in the tower base are primarily influenced by aerodynamic loads. Given that the simplified model introduces a change in the calculation of aerodynamic forces, it becomes crucial to examine its impact on this specific output parameter. Figure 45 displays the average and standard deviation for the tower base bending moment. It is evident that, as a general trend, the bending moments are overestimated in the simplified model, with an increase of 5.4% in average compared to the reference model. This overestimation aligns with the overestimation of average thrust force for the simplified model, as demonstrated in figure 42. However, when considering the standard deviation for the tower base bending moment, represented by the black error bars in figure 45, it is observed that variations are much more significant for the simplified model than for the reference model. Interestingly, this increase in standard variation cannot be attributed to a corresponding increase in the standard deviation of the thrust force. Figure 42 and table 9 demonstrate that variations in thrust force are much smaller for the simplified model compared to the reference model.
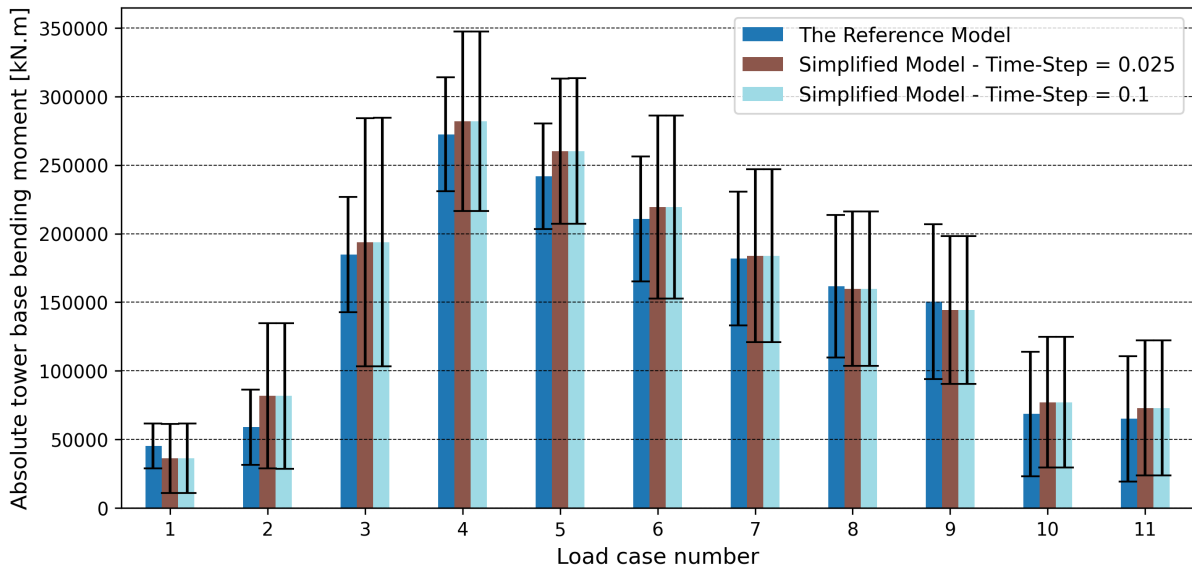
Figure 45: Average and standard deviation of absolute tower base bending moment for all 11 load cases

For a more in-depth analysis, load case number 3 is being focused on. In this specific case, figure 45 shows that the standard deviation in the simplified model is 116% higher compared to the reference model. In sharp contrast, the standard deviation for the thrust force given in figure 42 is 13% lower in the simplified model compared to the reference model for the exact same load case. To understand the cause of this phenomenon, the influence of wave and wind loads is examined, similar to analyses in section 6.6. The simplified model with a time-step of 0.1 seconds is used, and additional simulations are performed with wind loads only and wave loads only. The results, along with a comparison to combined loading, are shown in figure 46. Focusing on load case 3, it can be concluded that the overestimation of standard deviations observed in figure 45 originates from wind loads and not from wave loads.

To gain deeper insights into the high standard deviations observed for the absolute tower base bending moment, a thorough analysis of results for platform pitch is conducted in the subsequent section 8.5.5. Previous observations from section 6.6 have revealed that the tower base bending moment is influenced by two primary factors: the aerodynamic thrust force and gravitational loads. Gravitational loads result from the combined weight of the rotor, nacelle, and tower, acting with a leverage arm that depends on the platform pitch. Therefore, the investigation of variations in platform pitch becomes crucial in understanding the root cause behind the high fluctuations observed in the tower base bending moments.
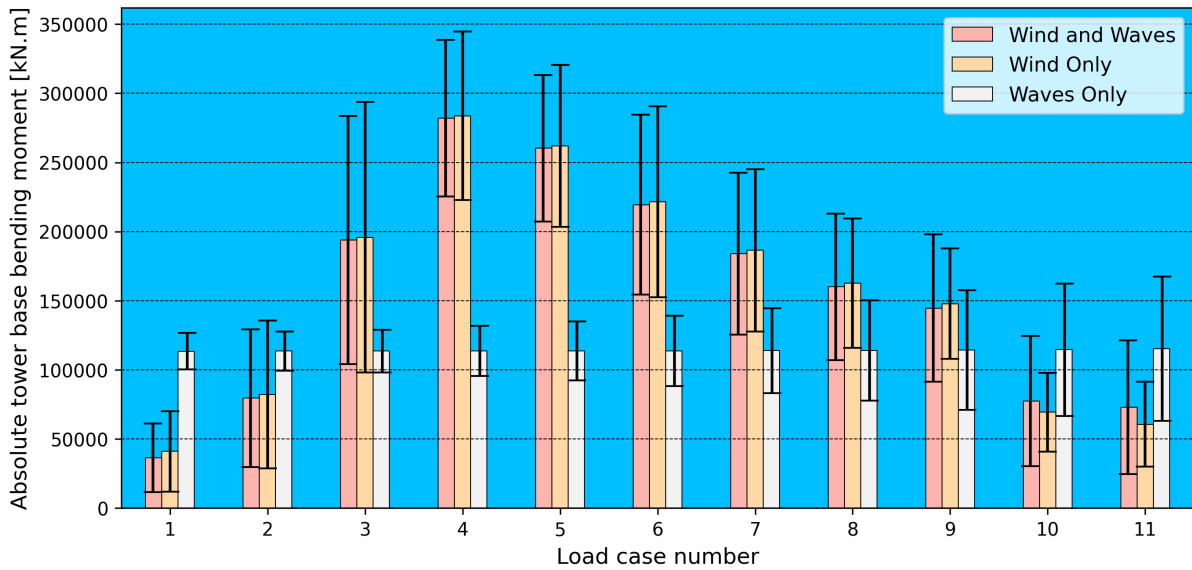
Figure 46: Average and standard deviation of the absolute tower base bending moment for the simplified model with a time-step of 0.1 seconds for wind loads only, wave loads only and combined load cases

8.5.5 *Platform Pitch and Mooring Line Tension*

Figure 47 displays the average and standard deviation of platform pitch for different load cases. Average values for the simplified model are underestimated for load cases for which no shut-down occurs. This can be attributed to the overestimation of average thrust forces displayed in figure 42, which results in a greater average inclination of the platform away from the wind. On the other hand, overestimations are observed in standard deviations. High variations in platform pitch can be attributed to the complex control system utilised in the FOWT, as explained in section 6.2.3. This control system plays a crucial role in mitigating the effects of intricate phenomena, as exemplified by the principle of negative damping. As depicted in figure 20, these effects can have a significant influences on platform pitch. The absence of a control system in the simplified model leads to some movements not being compensated, resulting in higher standard deviations. The overestimation of variations is most pronounced just below the rated wind speed of 10.6 m/s. As explained in section 6.2.2, the reference model includes a transition region that enables a smooth switch from partial to full load control. This transition region not being implemented in the simplified model results in an increase in platform pitch fluctuations, particularly for the third load case, corresponding to a mean wind speed of 8 m/s.

As mentioned in section 8.5.4, the tower base bending moment is highly dependent on platform pitch. Therefore, the substantial variations in platform pitch directly lead to significant variations in the tower base bending moment.

73
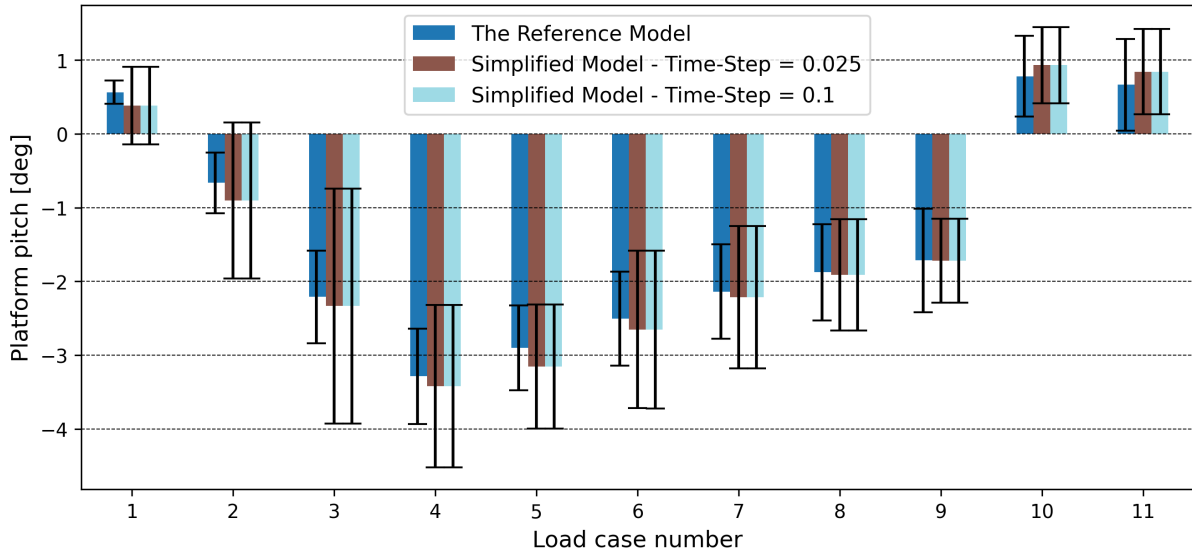
Figure 47: Average and standard deviation of platform pitch for all 11 load cases

Regarding average mooring line tension, the difference between the reference and simplified models is less than 2% in average. Unlike platform pitch, there are no significant overestimations of standard deviations. This can be attributed to the strong dependence of mooring line tension on surge motion. As discussed in section 6.2.3, the control system is more focused on mitigating pitch motions than surge motions, making mooring line tension resilient to its absence.

8.5.6 *Absolute Nacelle Acceleration and Velocity*

The last two parameters under analysis are the absolute nacelle acceleration and velocity. Upon examination, it is evident that the results for the simplified model with both time steps are very similar, showing no difference in average values and standard deviation greater than 0.2% for any load case. Therefore, figure 48 focuses on the comparison for the simplified model with a time step of 0.1 seconds. Similar to platform pitch and tower base bending moment, a significant overestimation of the standard deviation is observed for the lower load cases. Additionally, unlike previous findings, substantial differences in the average values are also observed. Notably, for load case 3, the average absolute nacelle acceleration is overestimated by around 98%, twice the value observed for the reference model. For absolute nacelle velocity, overestimations of averages are even more pronounced, reaching almost 2.5 times the values of the reference model for load case 3.

Figure 49 presents the comparison of absolute nacelle acceleration between wind-only, wave-only and combined load cases for the simplified model. Notably, overestimation of average
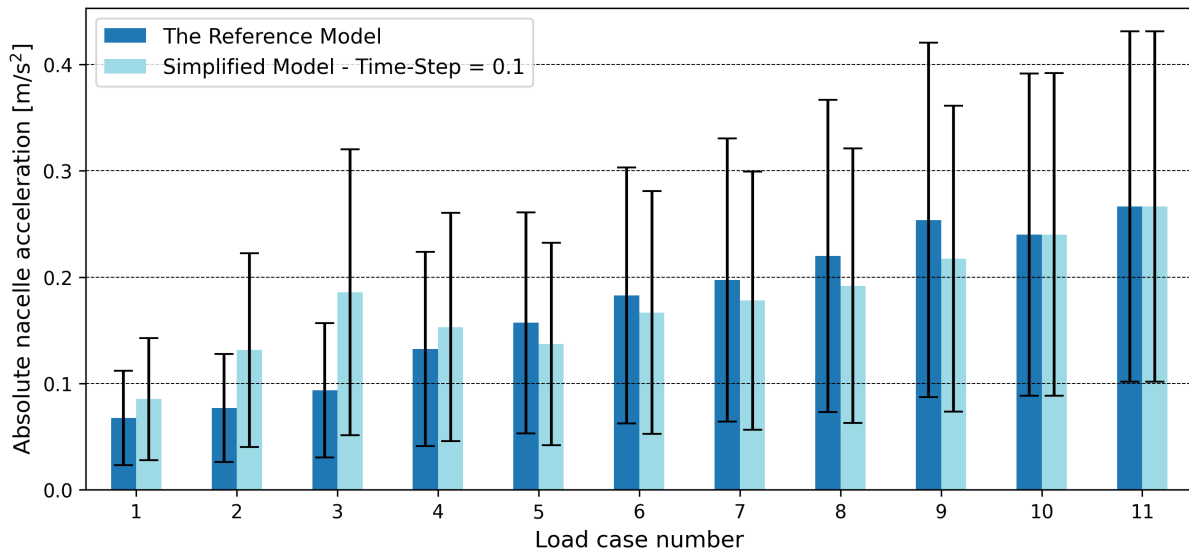
Figure 48: Average and standard deviation of absolute nacelle acceleration for all 11 load cases

accelerations still persists in the wind-only simulations, particularly evident in load case 3. Conversely, no such overestimation is observed in the wave-only simulations. For absolute nacelle velocity, these overestimations are even more pronounced. Consequently, it can be concluded that the overestimations in both average values and standard deviations of absolute nacelle acceleration and velocity for lower load cases are primarily attributed to wind loads, rather than wave-related phenomena. These overestimations are linked to the absence of a control system in the simplified model. They are most prominent in the transition region, where a control system would be vital to facilitate a smooth transition from partial to full power production.
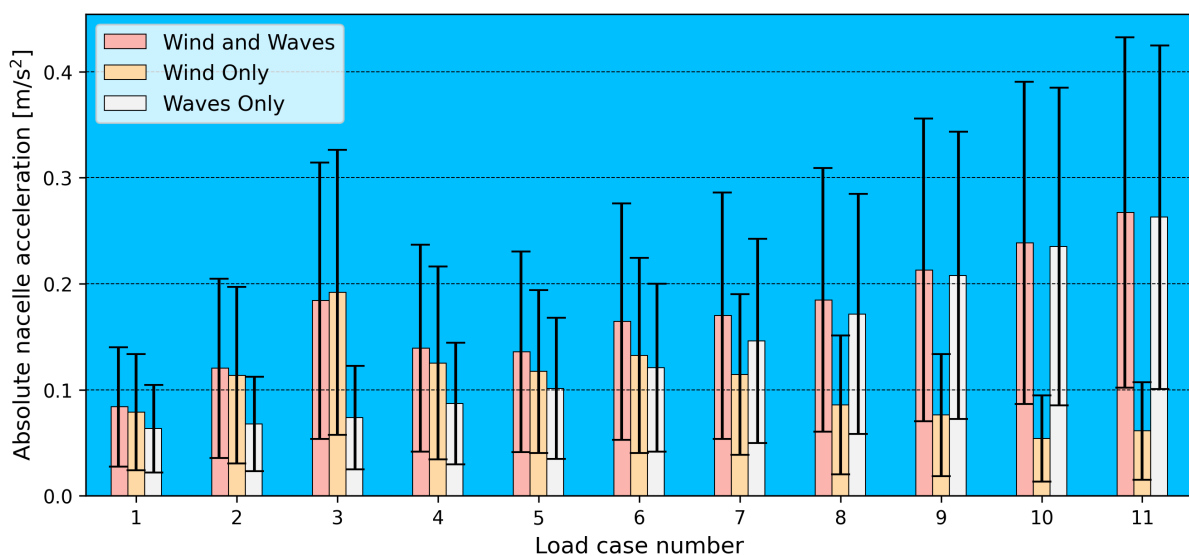
Figure 49: Average and standard deviation of the absolute nacelle acceleration for the simplified model with a time-step of 0.1 seconds for wind loads only, wave loads only and combined load cases

8.6 Summary - Key Findings from the Simplified Model

The simplified model offers a significant reduction in computational time. Employing the same time step as for the reference model, a reduction of 83% is achieved, while by employing a time-step of 0.1 seconds, computational time can be reduced by over 95%. Throughout the analyses, no significant differences were observed between results for different time steps.

For thrust forces, the simplified model slightly overestimates average values but presents important underestimations for their standard deviations. For higher load cases, when the turbine is controlled through blade pitch, discrepancies are most significant. For lower load cases where the turbine is controlled through rotor speed, differences are smaller and time-variations of thrust forces by the simplified model are better estimated. The discrepancies arise from the 'system memory' present in the reference model but absent in the simplified model. It causes the turbine to face wind at non-optimal configurations, whereas for the simplified model, turbine configuration is considered optimal all the time.

For global output parameters, namely platform pitch, mooring line tension, and tower base bending moment, the simplified model yields good predictions of average values. The absence of a control system for the simplified model leads to high fluctuations and thereby standard deviations for platform pitch, which translate to fluctuations in tower base bending moment. However, mooring line tension remains relatively unaffected due to its strong correlation with surge motion. For absolute nacelle acceleration and velocity, the absence of a control system not only increases standard deviations but also leads to important overestimations of absolute values, especially in the proximity of the transition region.

8.7 Conclusion - Domain of Application of the Simplified Model

The simplified model offers a trade-off between speed and accuracy, making it suitable for obtaining quick results while maintaining acceptable precision for most output parameters. Its efficiency allows for a higher volume of simulations within a limited timeframe, increasing overall work efficiency significantly. The domain of application of the simplified model would be during the preliminary stages of basic design (see figure 9). It is well-suited for a comparison between different floater layouts or turbine configurations, providing a global overview of turbine dynamics, aiding in decision-making processes. Once the floater layout is chosen, a more comprehensive model with a discretised representation of the rotor can be used for more detailed analyses and precise determination of dynamics, especially for complex load cases.

To conclude, the choice of model accuracy depends on the specific goal of the investigation. For comparative studies involving a large number of simulations, simplifications are advantageous. On the other hand, for in-depth examinations of a specific floater layout, using a more accurate model is preferable to ensure thorough results.

9 SUMMARY

For this study, the selection of the semi-submersible floater type is based on the analysis presented in section 2. As illustrated in [Mai+20] and [Cas+20], this choice is supported by the lower life cycle costs of the semi-submersible compared to other floater concepts, a factor partly driven by the simple and cost-effective float-out and installation procedures outlined in [Mai+20]. This floater type holds further advantages, such as its suitability for a wide range of water depths, as emphasised in [LKC18]. Additionally, ongoing technical advancements, like cancellation geometries and stabilising active ballast systems described in [LKC18], allow to compensate for some of the disadvantages of the concept. These favourable characteristics position the semi-submersible floater as the predominant choice for upcoming projects, as evidenced by [Día+22], making it suitable for the floating substructure used in this research.

Throughout this study, the complicated task of numerically modelling floating offshore wind turbines presented a great number of challenges, particularly due to the complicated nature of the aero-hydro-servo-elastic model, extensively discussed in [Far+22]. However, this complexity is ably addressed by the well-suited and efficient pairing of *OrcaWave* for diffraction and radiation analysis, alongside *OrcaFlex* for finite-element time-domain dynamic analysis. The validation of the turbine model in *OrcaFlex*, underpinned by comparison with alternative software and research results from FOWT prototypes, as depicted in [Ros18], provides confidence in its reliability. The software not only provides a coherent graphical interface, but also allows for a spectrum of model modifications and enhancements, tailored to specific research objectives, and offers a clear overview of outcomes. This research demonstrates the methodology for conducting a comprehensive analysis covering both the overall dynamics of the turbine and more intricate evaluations, including the assessment of local forces and kinematics. By harnessing the integration of both *Python* and *Excel*, the analytical capabilities are augmented, thereby allowing a more streamlined result analysis process and paving the path towards process automation. Incorporating external *Python* functions within the dynamic analysis, called upon at each time step, facilitates the intricate modelling of the turbine control system. Moreover, the conducted research illustrates how this approach enables the simplification and substitution of even essential turbine components, as exemplified in section 8. In summary, the decision to employ *OrcaFlex* has been successful and its capacity for modifications allowed for a deep understanding of key parameters influencing FOWT analysis.

Turbine control exerts a significant impact on system dynamics, as evidenced in section 6.2.3

where the dynamic effects related to negative damping are discussed, based on insights from [Lóp+22]. This influence becomes particularly pronounced when analysing the interplay of aerodynamic forces and turbine control, as highlighted in section 6.4. Regarding the chosen output parameters, their utility throughout this study proves valuable. Absolute nacelle acceleration and velocity play a crucial role in the study of local effects immediately aft the rotor, the modification of which is a major focus of this study. Wind loads dominantly govern these parameters, as elucidated in section 6.6. They collectively contribute to investigating the turbine's operational limits, both yielding similar conclusions across the research. Notably, nacelle acceleration, due to its specific capability in exploring turbine limits described in [Zho+21], often takes precedence over nacelle velocity when comparing outcomes. Platform pitch and absolute tower base bending moment display strong correlation, demonstrated in section 6.6.1, and offer valuable insights into the influence of modifications on overall system dynamics. Unlike nacelle acceleration and velocity, these two parameters are mainly driven by wind loads, acting not through wind speed but via rotor thrust, thereby accentuating the strong influence of the control system. Mooring line tension proves less effective in gauging model differences. It only displays minor disparities when comparing highly simplified models to the reference.

While model simplifications across various domains are performed, section 7 delves into the ones pertinent to turbine aerodynamics and rotor structural dynamics, offering insights that pave the way for more ventured simplifications in section 8. One significant outcome of this sensitivity analysis is that even the exclusion of minor parameters can yield substantial impacts on system dynamics. While enhancements to the aerodynamic model show relatively minor effects, the explored simplifications in structural dynamics yield more pronounced outcomes. This manifests in terms of both reduced simulation time and differences of output parameters when compared to simulations for the reference model, illuminating the delicate balance between computational speed and accuracy of results. However, the key discovery within section 7 is about the intricate interdependence among diverse domains. Altering the structural modelling of blades can induce direct changes in aerodynamic forces. Moreover, the linkage between hydrodynamics and structural dynamics is apparent, as adjustments in the structural modelling of the rotor lead to changes in how wave resonance influences certain output parameters, notably nacelle acceleration.

The simplified rotor model introduced in section 8 brings about a remarkable reduction in computational time, exceeding 95%. This efficiency enhancement translates into the capability to

conduct a greater number of simulations within a confined timeframe, significantly improving overall work productivity. Yet, it's crucial to acknowledge that this increase in computational efficiency does entail a trade-off in terms of output parameter accuracy. The results related to average rotor thrust are well approximated, while variations, represented by standard deviations, exhibit considerable underestimations. This suggests that the omission of the 'system memory', inherent in the reference model, leads to the oversight of important variations seen during abrupt shifts in wind speed, as demonstrated in section 8.5.3. Regarding output parameters, the most notable distinctions arise from the absence of a control system in the simplified model. This discrepancy becomes most pronounced in regions where the control system's impact is most profound, like the transition region elaborated in [Sam+20]. These observations indicate the appropriate scope for the simplified model. It finds its utility in the preliminary stages of the basic design, explained in [Far+22]. It is suitable for comparing different floater concepts or configurations, providing a global overview of turbine dynamics to support decision-making processes. This aligns with the context of this study, which aims to accelerate comparison between different concepts and layouts, as discussed in section 1.4. The reduction in computational time proves particularly valuable seen the important number of load cases required by class society, as illustrated in [DNV21c]. Once the floater layout is chosen, a more detailed model with a discretised rotor representation can be used to validate results and perform more in-depth analyses.

10   CONCLUSION

In conclusion, the performed research was a resounding success. The developed simplified model fully meets the objective described in section 1.4, reducing computation time by more than 95% while maintaining an acceptable accuracy, as corroborated through comparison with the reference model. Furthermore, in alignment with the findings presented in section 3.4, the model proves highly suitable for preliminary stages within the basic design phase. This mid-fidelity tool allows to incorporate the intricate interplay of diverse domains, encompassing hydrodynamics, aerodynamics, and structural dynamics. Its speed empowers the execution of a considerable number of simulations in a reduced amount of time, thereby significantly enhancing operational efficiency. Hence, the model could serves as a key instrument for the comparison of different floater concepts and layouts, which, in a later stage of the basic design phase, might be supplemented by verification and more comprehensive analyses using a model with a refined rotor representations. Given the critical need for decision-making concerning floater layout, as elaborated in section 1.3, the developed mid-fidelity tool has the potential to play a crucial role in future developments.

11 FUTURE RESEARCH

In the context of future research building upon the current study, possible progression could involve refining the simplified model introduced in section 8 to enhance its accuracy. As revealed in section 8.5.3, the absence of a 'system memory' in this model leads to an underestimation of thrust force variations. To address this, similar to the approach taken to anticipate rotor shutdown, the *Python* code used to estimate thrust force could be adapted to incorporate system inertia by considering blade pitch and rotor speed. Moreover, a more comprehensive investigation of the transition region from partial to full power production is recommended, as the high complexity of this operational region leads to discrepancies for output parameters in the simplified model. Addressing the analysis of environmental loads, the present study exclusively examines unidirectional loads within the operational range of the wind turbine, where mean wind speed stays between the cut-in and cut-off thresholds. A more extensive investigation should focus on assessing how the model simplifications perform when subjected to wind and waves from various directions, or under extreme scenarios such as storms and severe environmental conditions. Of particular interest would be to investigate the impact of sudden changes in wind direction, where the wind encounters the turbine at an angle. This situation would invalidate the assumptions made in section 8, necessitating adjustments such as wind angle-dependent databases. Moreover, it is advisable to test additional environmental seeds to ascertain whether this influences the manner in which model simplifications affect results. A similar exploration should be conducted for diverse floater layouts and geometries. Since the purpose of the simplifications is to facilitate the comparison of floater configurations, understanding whether applying rotor model simplifications yields distinct outcomes for different floating substructures is vital. However, it is important to remember that augmented complexity generally is accompanied by longer computational time. Striking a balance is key; an excessively intricate model could counteract the intent of the simplifications. Their purpose is not to produce the most precise results, but to allow for rapid and reasonably accurate outcomes.

In the future, the developed simplified model can find application in comparing an extensive database of floater layouts, by analysis and comparison of their dynamics. This could aid in determining which concepts are most suitable for distinct sites and environmental conditions. The reduced computational time of the simplified model would enable a greater number of comparisons, supporting decision-making within the industry and guiding investments towards the advancement of floating wind technology.

BIBLIOGRAPHY

Articles, Reports and Conference Papers

[AIC21]   Kehinde Adeseye Adeyeye, Nelson Ijumba, and Jonathan Colton. "The Effect of the Number of Blades on the Efficiency of A Wind Turbine." In: *Earth and Environmental Science* 801 (2021). DOI: 10.1088/1755-1315/801/1/012020.

[All+20]   Christopher Allen et al. "Definition of the UMaine VolturnUS-S Reference Platform Developed for the IEA Wind 15-Megawatt Offshore Reference Wind Turbine." In: *Technical Report: NREL TP-5000-76773* (2020). URL: https://www.nrel.gov/docs/fy20osti/76773.pdf.

[And+14]   S. Andrew Ning et al. "Development and Validation of a New Blade Element Momentum Skewed-Wake Model within AeroDyn ." In: *Conference Paper: NREL CP-5000-63217* (2014). URL: https://www.nrel.gov/docs/fy15osti/63217.pdf.

[AO20]   O. Apata and D.T.O. Oyedokun. "An overview of control techniques for wind turbine systems." In: *Scientific African* 10 (2020). DOI: 10.1016/j.sciaf.2020.e00566.

[BKS15]   Hasan Bagbanci, D. Karmakar, and C. Guedes Soares. "Comparison of Spar and Semisubmersible Floater Concepts of Offshore Wind Turbines Using Long-Term Analysis." In: *Journal of Offshore Mechanics and Arctic Engineering* 137.061601 (2015). DOI: 10.1115/1.4031312.

[BF11]   Petter Andreas Berthelsen and Ivar Fylling. "WINDOPT: An Optimization Tool for Floating Support Structures for Deep Water Wind Turbines." In: *Conference Paper OMAE2011* (2011). URL: 10.1115/OMAE2011-49985.

[Cas+20]   Laura Castro-Santos et al. "Economic Feasibility of Floating Offshore Wind Farms in the North of Spain." In: *Journal of Marine Science and Engineering* 8 (2020). DOI: 10.3390/jmse8010058.

[Día+22]   Hugo Díaz et al. "Market Needs, Opportunities and Barriers for the Floating Wind Industry." In: *Journal of Marine Science and Engineering* 10 (2022). DOI: 10.3390/jmse10070934.

[Eld17]   Steinar Eldøy. "Hywind Scotland Pilot Park Project: Plan for Construction Activities 2017." In: *Report from Statoil* C178-HYS-Z-GA-00001 (2017). URL: https://marine.gov.scot/sites/default/files/00516548.pdf.

[Far+22]   Emilio Faraggiana et al. "A review of numerical modelling and optimisation of the floating support structure for offshore wind turbines." In: *Journal of Ocean Engineering and Marine Energy* 8 (2022), pp. 433–456. DOI: https://doi.org/10.1007/s40722-022-00241-2.

[Gae+20]   Evan Gaertner et al. "Definition of the IEA Wind 15-Megawatt Offshore Reference Wind Turbine." In: *Technical Report / NREL* TP-5000-75698 (2020). URL: https://www.nrel.gov/docs/fy20osti/75698.pdf.

[GKD17]   Andrew J. Goupee, Richard W. Kimball, and Habib J. Dagher. "Experimental observations of active blade pitch and generator control influence on floating wind turbine response." In: *Renewable Energy* 104 (2017), pp. 9–19. DOI: 10.1016/j.renene.2016.11.062.

[Hai+13]   Lorenz Haid et al. "Simulation-Length Requirements in the Loads Analysis of Offshore Floating Wind Turbines." In: *International Conference on Offshore Mechanics and Arctic Engineering* Volume 8: Ocean Renewable Energy (2013). DOI: https://doi.org/10.1115/OMAE2013-11397.

[IEA19]   IEA. "Offshore Wind Outlook 2019." In: *Special Report* CC BY 4.0 (2019). URL: https://www.iea.org/reports/offshore-wind-outlook-2019.

[LRS21]   Jeremy Ledoux, Sebastián Riffo, and Julien Salomon. "Analysis of the Blade Element Momentum Theory." In: *Journal on Applied Mathematics* 81.(6) (2021), pp. 2596–2621. URL: https://hal.science/hal-02550763v2.

[LKC18]   M Leimeister, A Kolios, and M Collu. "Critical review of floating support structures for offshore wind farm deployment." In: *Journal of Physics: Conference Series* 1104.012007 (2018). DOI: 10.1088/1742-6596/1104/1/012007.

[Lem+20]   Frank Lemmer et al. "Semi-submersible wind turbine hull shape design for a favorable system response behavior." In: *Marine Structures* 71.102725 (2020). DOI: https://doi.org/10.1016/j.marstruc.2020.102725.

[Lóp+22]   Javier López-Queija et al. "Review of control technologies for floating offshore wind turbines." In: *Renewable and Sustainable Energy Reviews* 167.112787 (2022). DOI: 10.1016/j.rser.2022.112787.

[Mai+20]   C. Maienza et al. "A life cycle cost model for floating offshore wind farms." In: *Applied Energy* 266.114716 (2020). URL: https://doi.org/10.1016/j.apenergy.2020.114716.

[Mou14]   Jur Mourits. "BEM theory and CFD for Wind Turbine Aerodynamics." In: *Internship Report*. The University of Liverpool (2014). URL: https://purl.utwente.nl/essays/69276.

[Ørs22]   Ørsted. "Deeper waters, stronger winds; How can floating offshore wind be scaled?." In: *White paper* Version 1.0 (2022). URL: https://orsted.com/en/insights/white-papers/floating-wind.

[Ott+21]   Aldert Otter et al. "A review of modelling techniques for floating offshore wind turbines." In: *Wind Energy* 25 (2021), pp. 831–857. DOI: https://doi.org/10.1002/we.2701.

[Ros18]   A. Ross. "Wind Turbine Validation Report." In: *Orcina Project 1405* 01 (2018). URL: https://www.orcina.com/wp-content/uploads/resources/validation/R14050101-Wind-Turbine-Validation-Report.pdf.

[Sam+20]   Arash E. Samani et al. "The Impact of Pitch-To-Stall and Pitch-To-Feather Control on the Structural Loads and the Pitch Mechanism of a Wind Turbine." In: *Energies* 13.4503 (2020). DOI: 10.3390/en13174503.

[Sar+20]   Md. Rasel Sarkar et al. "Hybrid Pitch Angle Controller Approaches for Stable Wind Turbine Power under Variable Wind Speed." In: *Energies* 13.3622 (2020). DOI: 10.3390/en13143622.

[Sia+21]   Asiaban Siavash et al. "Wind and Solar Intermittency and the Associated Integration Challenges: A Comprehensive Review Including the Status in the Belgian Power System." In: *Energies* 14.2630 (2021). DOI: 10.3390/en14092630.

[Ste+16]   Gordon M. Stewart et al. "The creation of a comprehensive metocean data set for offshore wind turbine simulations." In: *Wind Energy* 19 (2016), pp. 1151–1159. DOI: 10.1002/we.1881.

[Vel+19]   Joey Velarde et al. "Probabilistic analysis of offshore wind turbines under extreme resonant response: Application of environmental contour method." In: *Applied Ocean Research* 93.101947 (2019). DOI: 10.1016/j.apor.2019.101947.

[YKK20]   Seong Mo Yeon, Joo-Sung Kim, and Hyun Joe Kim. "Numerical wind load estimation of offshore floating structures through sustainable maritime atmospheric boundary layer." In: *International Journal of Naval Architecture and Ocean Engineering* 12 (2020), pp. 819–831. DOI: 10.1016/j.ijnaoe.2020.07.003.

[Zho+21]   Shengtao Zhou et al. "Global sensitivity study on the semisubmersible substructure of a floating wind turbine: Manufacturing cost, structural properties and hydrodynamics." In: *Ocean Engineering* 221.108585 (2021). DOI: https://doi.org/10.1016/j.oceaneng.2021.108585.

Online Sources

[Ene21]   Weamec - Marine Energy. *WindFloat*. 2021. URL: https://www.weamec.fr/en/synthesis/windfloat/ (visited on 06/22/2023).

[Eng20]   Engineering.com. *The Future of Wind Turbines: Comparing Direct Drive and Gearbox*. 2020. URL: https://www.engineering.com/story/the-future-of-wind-turbines-comparing-direct-drive-and-gearbox (visited on 06/12/2023).

[Equ23a]   Equinor. *Hywind Scotland*. 2023. URL: https://www.equinor.com/energy/hywind-scotland (visited on 05/30/2023).

[Equ21]   Equinor. *Hywind Scotland remains the UK's best performing offshore wind farm*. 2021. URL: https://www.equinor.com/news/archive/20210323-hywind-scotland-uk-best-performing-offshore-wind-farm (visited on 05/09/2023).

[Equ17]   Equinor. *Hywind Scotland, The world's first commercial floating wind farm*. 2017. URL: https://www.equinor.com/content/dam/statoil/documents/newsroom-additional-documents/news-attachments/brochure-hywind-a4.pdf (visited on 06/22/2023).

[Equ23b]   Equinor. *Hywind Tampen*. 2023. URL: https://www.equinor.com/energy/hywind-tampen (visited on 05/30/2023).

[Geo18]   GeoTechSimulation. *Application of Rayleigh Damping and Numerical Damping in Finite Element/Difference Analysis*. 2018. URL: https://geotechsimulation.com/2018/04/09/rayleigh-and-numerical-damping-in-finite-element-analysis/ (visited on 06/01/2023).

[Goa23]   Mark Goalen. *Overcoming Floating Wind Challenges Is Key to Global Energy Transition*. 2023. URL: https://www.offshorewind.biz/2023/01/27/overcoming-floating-wind-challenges-is-key-to-global-energy-transition-houlder/ (visited on 08/08/2023).

[Ibe23]   Iberdrola. *Floating offshore wind power: a milestone to boost renewables through innovation*. 2023. URL: https://www.iberdrola.com/innovation/floating-offshore-wind (visited on 06/22/2023).

[Ide23]   BW Ideol. *Floatgen - France's first offshore wind turbine and BW Ideol's first unit*. 2023. URL: https://www.bw-ideol.com/en/floatgen-demonstrator (visited on 06/22/2023).

[NI23]   NI. *Wind Turbine Control Methods*. 2023. URL: www.ni.com/en-us/innovations/white-papers/08/wind-turbine-control-methods.html (visited on 06/11/2023).

[NRE23]   NREL. *FAST - Wind Research*. 2023. URL: https://www.nrel.gov/wind/nwtc/fast.html (visited on 04/21/2023).

[Off21]   Offshorewind. *Final Kincardine Floating Wind Platform Leaves Spain*. 2021. URL: https://www.offshorewind.biz/2021/05/10/final-kincardine-floating-wind-platform-leaves-spain/ (visited on 06/22/2023).

[Orc23a]   Orcina. *OrcaFlex - examples: renewables*. 2023. URL: https://www.orcina.com/resources/examples/?key=k (visited on 07/10/2023).

[Orc23b]   Orcina. *OrcaFlex - Help*. 2023. URL: https://www.orcina.com/webhelp/OrcaFlex/Default.htm (visited on 04/25/2023).

[Orc23c]   Orcina. *OrcaFlex - validation documents*. 2023. URL: https://www.orcina.com/resources/validation/ (visited on 04/21/2023).

[Orc23d]   Orcina. *OrcaWave - Help*. 2023. URL: https://www.orcina.com/webhelp/OrcaWave/Default.htm (visited on 05/10/2023).

[Ørs23]   Ørsted. *Advantages of offshore wind*. 2023. URL: https://us.orsted.com/renewable-energy-solutions/offshore-wind/what-is-offshore-wind-power/advantages-of-offshore-wind (visited on 05/30/2023).

[Pri22]   PrinciplePower. *The WindFloat advantage - Fabrication*. 2022. URL: https://www.principlepower.com/windfloat/advantage/fabrication (visited on 06/22/2023).

[Que23]   QuestFWE. *Quest Floating Wind Energy*. 2023. URL: https://questfwe.com/ (visited on 05/30/2023).

[Rab23]   Rabobank. *Great Efforts Required To Achieve EU Countries' National Offshore Wind Energy Targets*. 2023. URL: https://www.rabobank.com/knowledge/d011347929-great-efforts-required-to-achieve-eu-countries-national-offshore-wind-energy-targets (visited on 05/09/2023).

[Reo22]   Reoltec. *Soluciones Flotantes TLPWind Iberdrola*. 2022. URL: https://reoltec.net/project/tlpwind-iberdrola/ (visited on 06/22/2023).

[Sta20]   Laerd Statistics. *Pearson's product moment correlation*. 2020. URL: https://statistics.laerd.com/statistical-guides/pearson-correlation-coefficient-statistical-guide.php (visited on 06/16/2023).

[Str16]   University of Strathclyde. *Floating Structures*. 2016. URL: https://www.esru.strath.ac.uk//EandE/Web_sites/15-16/Floating_Windfarm_Installation/floating-structures.html (visited on 06/22/2023).

[Wik22]   Coastal Wiki. *Currents*. 2022. URL: http://www.coastalwiki.org/wiki/Currents#:~:text=The%5C%20most%5C%20important%5C%20tidal%5C%20currents,3%5C%20m%5C%2Fs. (visited on 04/24/2023).

Books

[Bra17]   Emmanuel Branlard. *Wind Turbine Aerodynamics and Vorticity-Based Methods*. Vol. 7. Jan. 2017, Chapter 13: pp. 189–204. ISBN: 978-3-319-55163-0. DOI: 10.1007/978-3-319-55164-7.

[EAA22]   Ali M. Eltamaly, Almoataz Y. Abdelaziz, and Ahmed G. Abo-Khalil. *Control and Operation of Grid-Connected Wind Energy Systems*. Mar. 2022. ISBN: 978-3-030-64338-6. DOI: 10.1007/978-3-030-64336-2.

[PK17]   Arthur Pecher and Jens Peter Kofoed. *Handbook of Ocean Wave Energy*. 2017. ISBN: 978-3-319-39888-4. DOI: 10.1007/978-3-319-39889-1.

[POD08]   Roxy Peck, Chris Olsen, and Jay Devore. *Introduction to Statistics and Data Analysis*. Vol. 3. 2008. ISBN: 978-0-495-11873-2.

Class Society Standards

[DNV21a]   DNV-RP-0286. *Coupled analysis of floating wind turbines*. Standard. October, 2021.

[DNV21b]   DNV-RP-C205. *Environmental conditions and environmental loads*. Standard. September, 2021.

[DNV21c]   DNV-ST-0437. *Loads and site conditions for wind turbines*. Standard. November, 2021.

A   APPENDIX - THEORETICAL BACKGROUND

This appendix serves as a supplementary resource to provide detailed explanations of the theoretical background of various concepts utilised and discussed throughout this paper. It starts with a general description of the main components of a wind turbine in appendix A.1. Then, it delves into explanations of the energy extraction mechanism employed by turbine blades in appendix A.2, which supplies additional insights into supplementary factors that impact turbine performance, such as the influence of the control system and the number of blades. Appendix A.3 provides an explanation of the spectral representation of ocean waves, while appendix A.4 does the same for wind, exploring the theory of wind turbulence and long-term wind variations. Appendix A.5 presents the theoretical background behind the *Blade Element Momentum Theory*, while appendix A.6 explains how this theorem is applied within *OrcaFlex*. Both appendices A.7 and A.8 focus on the theoretical foundations underlying the modelling sensitivity analysis conducted in section 7. Finally, appendix A.9 provides a description of the Pearson product-moment correlation coefficient, which is frequently used throughout this report in data comparisons.

A.1   Main Components of a Wind Turbine

According to [Lóp+22], various wind turbine configurations exist, with the horizontal axis wind turbine with three blades being most prominent. The three-blade configuration offers enhanced power production, lower cut-in wind speeds, and a favourable balance between performance and cost, as outlined in appendix A.2.4. The wind turbine consists of three main components: the tower, the nacelle, and the rotor. The tower is a tall structure that provides support for other components. Its height is a crucial factor as it allows for extraction of higher wind speeds, resulting in increased energy production. The nacelle is located at the tower top and houses the mechanical and electrical components needed for power production. It furthermore incorporates a yaw mechanism that enables the turbine to align with the prevailing wind direction. The rotor is the rotating part of the wind turbine, consisting of the blades attached to a central hub. The blades are aerodynamically shaped to capture the kinetic energy of the wind. As the wind flows over them, lift and drag forces are generated, causing rotor rotation and a downwind thrust force. Figure 50, provides a schematic overview of the principal components of a wind turbine.

The gearbox serves to increase the rotational speed of the rotor before transmitting it to the generator. However, according to [Eng20], direct-drive wind turbines exist where generator speed
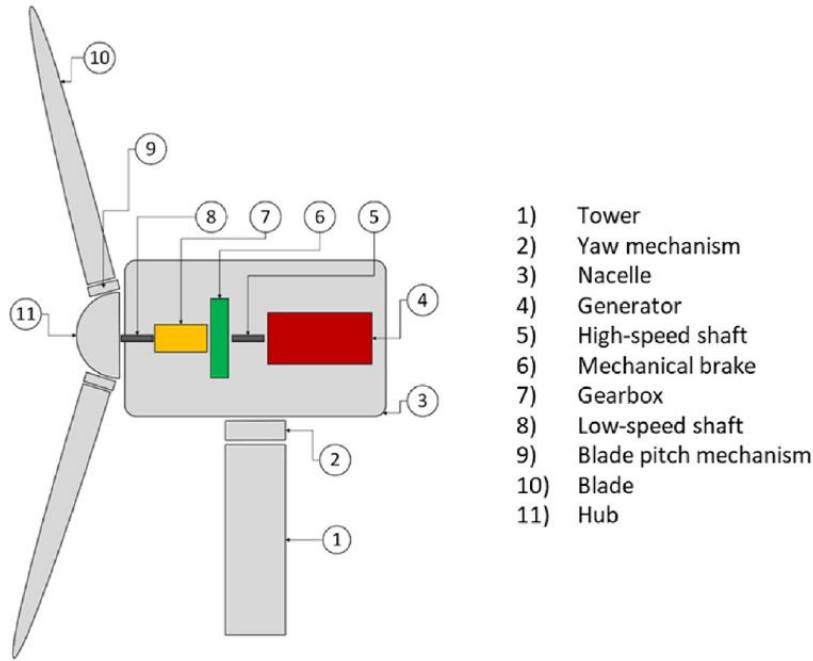
Figure 50: Wind turbine main components [Lóp+22]

1)	Tower
2)	Yaw mechanism
3)	Nacelle
4)	Generator
5)	High-speed shaft
6)	Mechanical brake
7)	Gearbox
8)	Low-speed shaft
9)	Blade pitch mechanism
10)	Blade
11)	Hub

is equivalent to the rotor speed, reducing the number of moving parts, eliminating gearbox failure, and decreasing transmission losses. To generate electricity at a low rotational speed, the generator in direct-drive wind turbines incorporates multiple magnetic poles to achieve the desired high output frequency. Consequently, direct-drive turbines require heavier generators with a larger diameter and are in general more expensive. As outlined in [Lóp+22], there are four distinct wind turbine configurations based on the presence of a blade pitch mechanism or fixed pitch operation and the ability to operate at variable or fixed speeds. Their influence on turbine control is investigated in appendix A.2.5. For large turbines, the variable-speed-variable-pitch (VS-VP) configuration is the most prominent one.

A.2   Wind Turbine Power Extraction

This appendix serves as a supplementary resource to further elucidate the concepts discussed in section 6.2. It provides detailed explanation of the energy extraction mechanism employed by turbine blades, offering a comprehensive understanding of the factors that contribute to the determination of the optimal power coefficient as depicted in equation (8):

$$P_w = 0.5\rho A C_p V^3 \ .$$

To comprehend the origin of the optimal power coefficient and its variation over the tip speed ratio, it is crucial to understand how the aerodynamic forces exerted on the turbine blades lead

to the rotational motion of the turbine and the extraction of power. As explained in [Mou14], the turbine blades can be conceptually divided into infinitesimal blade sections, with one such section illustrated in figure 51.
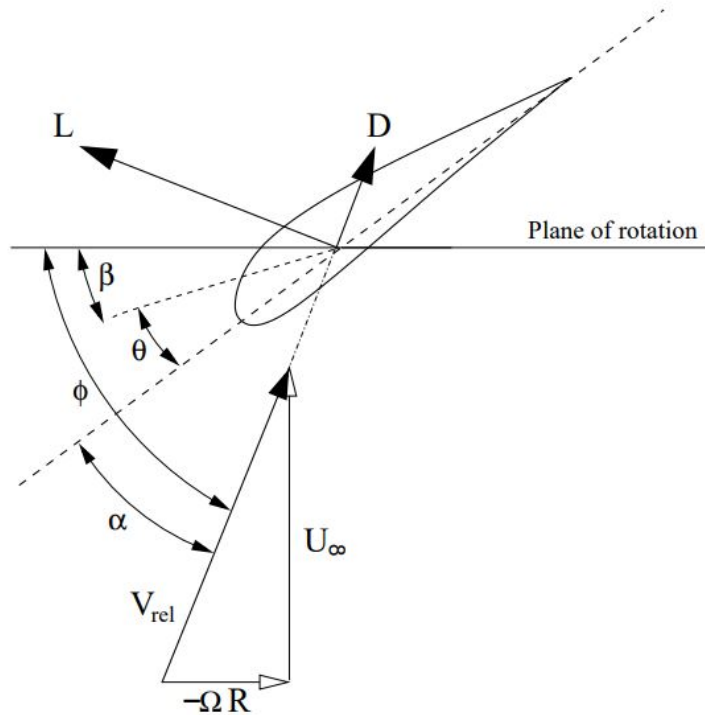
Figure 51: Aerodynamic forces acting on an infinitesimal blade section [Mou14]

In this figure 51 the relative inflow angle ϕ is defined as the sum of the sectional angle of attack α, the geometric twist angle θ and the pitch angle of the blade β. Furthermore, the lift and drag forces experienced by the blade section are denoted as L and D respectively. The velocity of the incident wind is called U_∞ and it is normal to the plane of rotation of the blade. Together with the tangential velocity of the section, formed by its rotational velocity Ω and its radius R, the relative wind velocity V_{rel} experienced by the blade section is obtained. The component of the aerodynamic forces that contributes to the torque, thus driving the rotation of the blades, can be expressed as $[L\sin(\phi) - D\cos(\phi)]$. Simultaneously, the component that contributes to the thrust is $[L\cos(\phi) + D\sin(\phi)]$.

A.2.1 Power, Torque and Thrust Coefficients

Previous equations reveal that the thrust, torque, and subsequently the power extracted by the rotor are exclusively determined by the relative inflow angle ϕ. Through figure 51, it is furthermore observed that the relative inflow angle is influenced by two underlying parameters: the

blade pitch angle β and the relationship between the incident and rotational velocities, which can be quantified by the tip speed ratio λ, defined in equation (9) as:

$$\lambda = \frac{\Omega R_{\text{tip}}}{V} \ .$$

Consequently, it can be concluded that the power coefficient is fully determined by two variables: the blade pitch angle β and the tip speed ratio λ and therefore express as $C_p(\lambda, \beta)$. In a similar manner to equation (8), torque and thrust can be represented using thrust and torque coefficients, which are dependent on the blade pitch angle and tip speed ratio only. They are therefore denoted as $C_t(\lambda, \beta)$ and $C_q(\lambda, \beta)$.

A.2.2 The Optimal Power Coefficient

Article [Sar+20] provides insights into the relationship between the power coefficient and the tip speed ratio and blade pitch. Results presented in figure 52 demonstrates that, for a given blade pitch, the power coefficient exhibits a maximum value at a specific tip speed ratio.
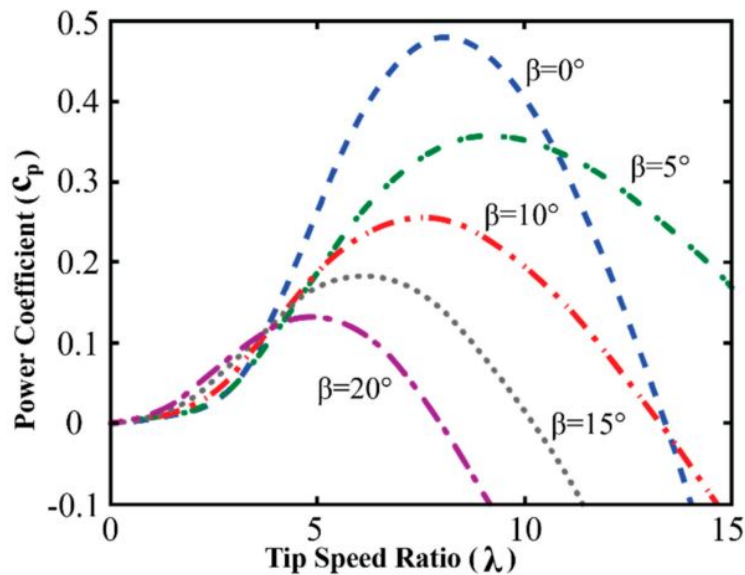
Figure 52: Power coefficient as a function of the tip speed ratio for different pitch angles [Sar+20]

The exact location and magnitude of this maximum power coefficient depend on the specific blade geometry. In the context of figure 52, the highest power coefficient is achieved at a blade pitch angle of zero degrees. To establish a connection between these maximum power coefficients and the operational regions illustrated in figure 18, it can be inferred that for the wind speeds ranging from cut-in to rated speed, the blade pitch angle would be fixed at zero degrees.

Furthermore, the rotational speed of the turbine would be continuously adjusted to match the incident wind speed, thereby maintaining a constant tip speed ratio corresponding to the maximum power coefficient. This configuration would allow for maximum power extraction. Figure 53 illustrates the relationship between the power coefficient and both the tip speed ratio and the blade pitch angle for the NREL5MW reference wind turbine. It provides an overview of how the power coefficient changes as these two parameters vary.
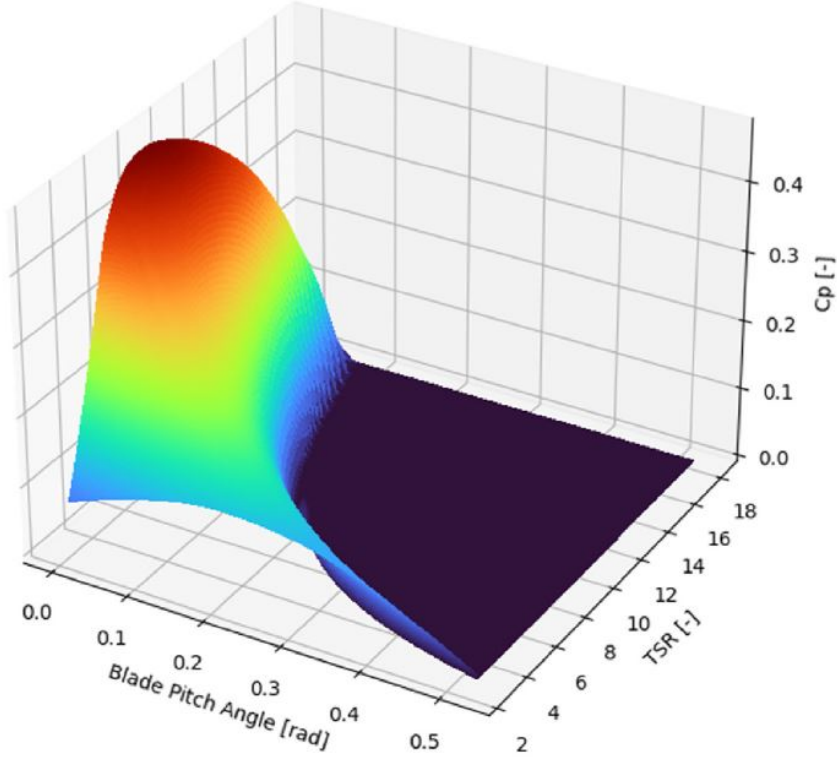
Figure 53: The power coefficient as a function of blade pitch angle and tip speed ratio [Lóp+22]

A.2.3   Betz's Law

As explained in [Lóp+22], the power that can be extracted from the wind is inherently limited. To comprehend this constraint, the extreme scenario can be considered where all available power is extracted. According to the law of conservation of energy (equation (21)), this would lead to a zero velocity behind the turbine, which is physically unattainable as it would result in fluid particle blockage. Through mathematical analysis, a theoretical upper limit for the power coefficient is derived, referred to as Betz's law, with a value of 0.593. Consequently, wind turbines are constrained to capture a theoretical maximum of 59.3% of the kinetic energy of the wind.

A.2.4   The Number of Blades

According to [AIC21], the number of blades in a vertical axis wind turbine has a significant impact on its performance. Figure 54 demonstrates the relationship between the performance coefficient (formerly referred to as the power coefficient), the tip speed ratio, and the number of rotor blades. The results indicate that increasing the number of blades from one to two, and then from two to three, leads to a substantial increase in the maximum value of the performance coefficient. Additionally, this maximum value is shifted to a lower tip speed ratio. Consequently, a rotor with three blades enables a significant improvement in power production compared to a rotor with fewer blades, resulting in an increase in rated power output.
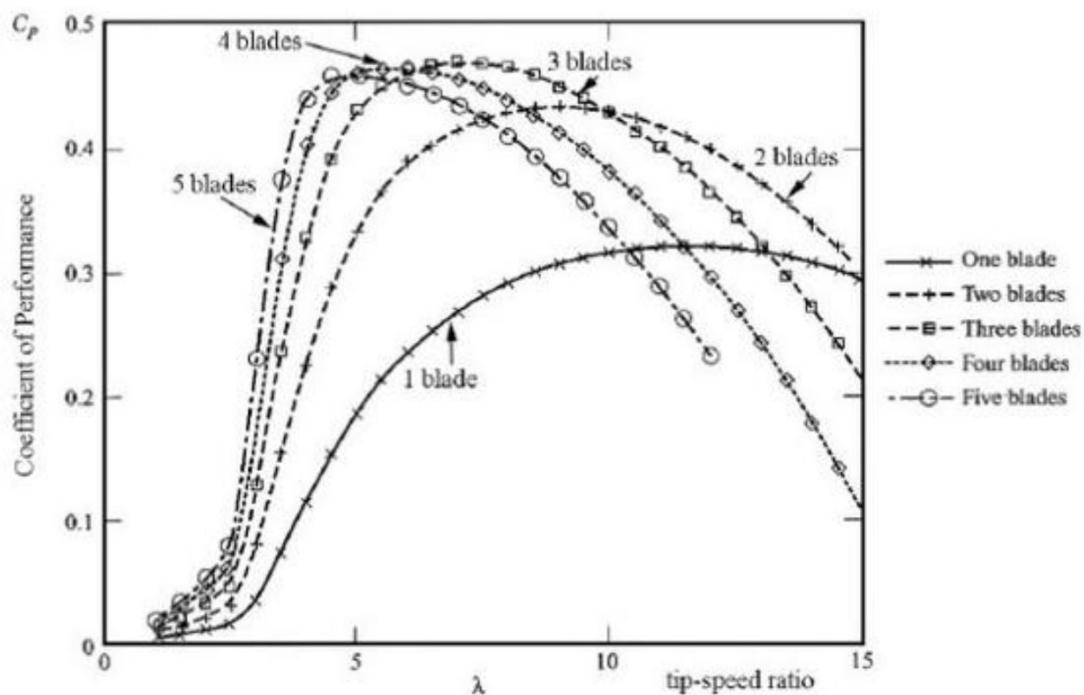
Figure 54: The effect of the number of blades on the performance coefficient [AIC21]

However, further increasing the number of blades does not yield any additional enhancement in the maximum performance coefficient. Instead, it is observed that maximum values occur at lower tip speed ratios. According to [AIC21], this could be beneficial since, based on the definition of the tip speed ratio, maximum power production can be achieved at lower rotational speeds. Moreover, a decrease in the cut-in wind speed can be expected, which allows the turbine to operate within a wider range of wind speeds. Increasing the number of blades above three is particularly significant in areas with low average wind speeds, as it can lead to a considerable increase in annual power generation. However, in regions with favourable wind conditions, such

93

as offshore locations, the additional increase in annual power production resulting from an increased number of blades would be minimal. Considering the high costs associated with blade manufacturing and installation, this slight increase in power production would not justify the additional expenses. Hence, the three-blade configuration appears to be the most suitable choice for turbines situated in areas with at least moderate average wind speeds.

A.2.5   Different Control Strategies

By integrating the insights provided in section 6.2 with the content presented in this appendix, the subsequent section illustrates the benefits associated with a variable speed - variable pitch (VS-VP) control system, as used for figure 19. Figure 55 presents the power curve corresponding to distinct control strategies, which differ based on the implementation of either fixed speed (FS) or variable speed (VS), as well as fixed pitch (FP) or variable pitch (VP) approaches.
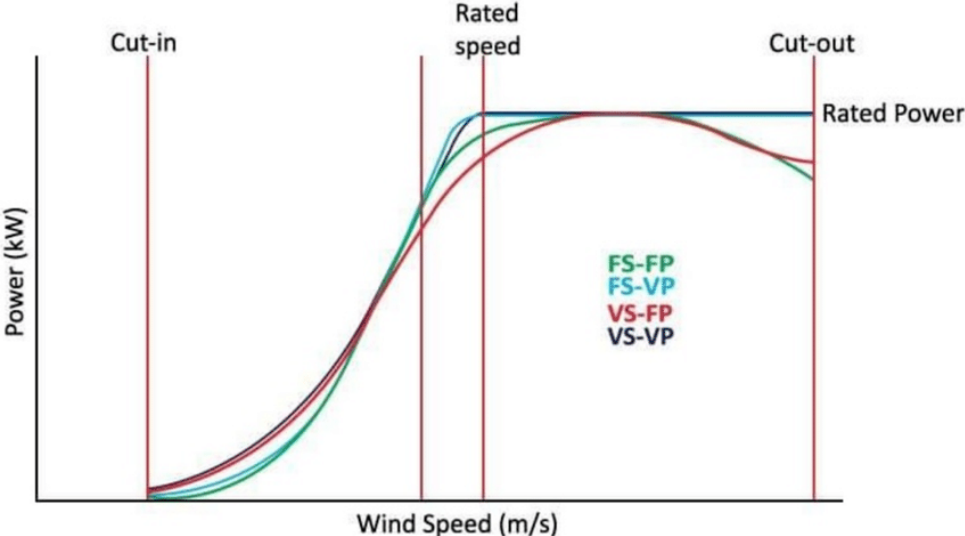
Figure 55: Power curves for different control strategies [NI23]

According to [NI23], the FS-FP (fixed speed - fixed pitch) control system represents the most basic approach. Operating at a fixed speed enables direct coupling of the turbine's generator to the power grid and the absence of a blade pitch system reduces the number of movable parts, resulting in simplified maintenance requirements. In this setup, the absence of active control limits the potential for performance enhancement. As both the rotational speed and the blade pitch are fixed, the turbine can operate at maximum efficiency solely at a specific wind speed within the low-speed region. Similarly, the rated power output is attainable only at a single wind speed. Consequently, this configuration exhibits poor power regulation and is not utilised in

multi-megawatt turbines. Operating the turbine at a variable rotational speed is feasible when the generator is not directly connected to the grid, allowing it to rotate independently of the grid frequency. In the low-speed region, by continuously adjusting the rotor speed to maintain a constant tip speed ratio (TSR), maximum power extraction can be achieved. However, due to the absence of a blade pitch mechanism, the rated power can only be attained at a single operating point. Incorporating a variable pitch system in the turbine control strategy enables operation with a fixed pitch angle below the rated wind speed, while continuously adjusting the pitch angle above the rated wind speed. This allows for the extraction of rated power across the entire range of region III. Consequently, the variable speed-variable pitch (VS-VP) control strategy stands out as the only approach that enables maximal energy extraction throughout the feasible range of wind speeds.

A.2.6   *Control for Floating Offshore Wind Turbines*

In section 6.2.3, the challenges faced in controlling FOWTs are discussed, emphasising the crucial role of the control system in mitigating dynamic effects. To expand this discussion, [Lóp+22] presents approaches on how the conventional onshore VS-VP controller can be modified to account for the complex dynamic behaviour of the floating structure. A first approach uses a collective pitch control strategy, where an additional blade pitch control loop is implemented that utilises the tower top acceleration signal as feedback. By adapting the aerodynamic rotor thrust based on the system's movements, the collective pitch control can help mitigate the effects of the floating platform's dynamics. Another approach consists of the application of individual pitch control to counteract fore-aft pitch motion of the floater. By adjusting the pitch angles of the upper and lower blade differently, a restoring moment is generated at the tower top to counter the platform's pitch movements.

It is important to note that these mitigation systems introduce additional complexity to the overall system and rely on mechanical components such as the pitch system. Consequently, the increased use of such systems can lead to greater mechanical wear and, subsequently, necessitate higher maintenance requirements. [Lóp+22] acknowledges the presence of additional systems, such as tuned mass dampers for structural vibration control. However, the detailed discussion of these more advanced strategies is beyond the scope of the present study.

A.3 Wave Spectra

According to [PK17], the representation of the actual sea state often assumes that the water surface can be characterised as the sum of sinusoidal waves with different frequencies, amplitudes, and directions. This representation allows for the modelling of the complex wave patterns observed in the ocean. The wave spectrum refers to the variation of wave energy with respect to frequency. Figure 56 illustrates the superposition of waves and the accumulation of energy associated with each wave component, corresponding to specific periods or frequencies. The figure showcases how individual waves combine and interact to form a composite wave pattern. As these waves overlap, their individual energy contributions add up, resulting in an overall energy distribution.
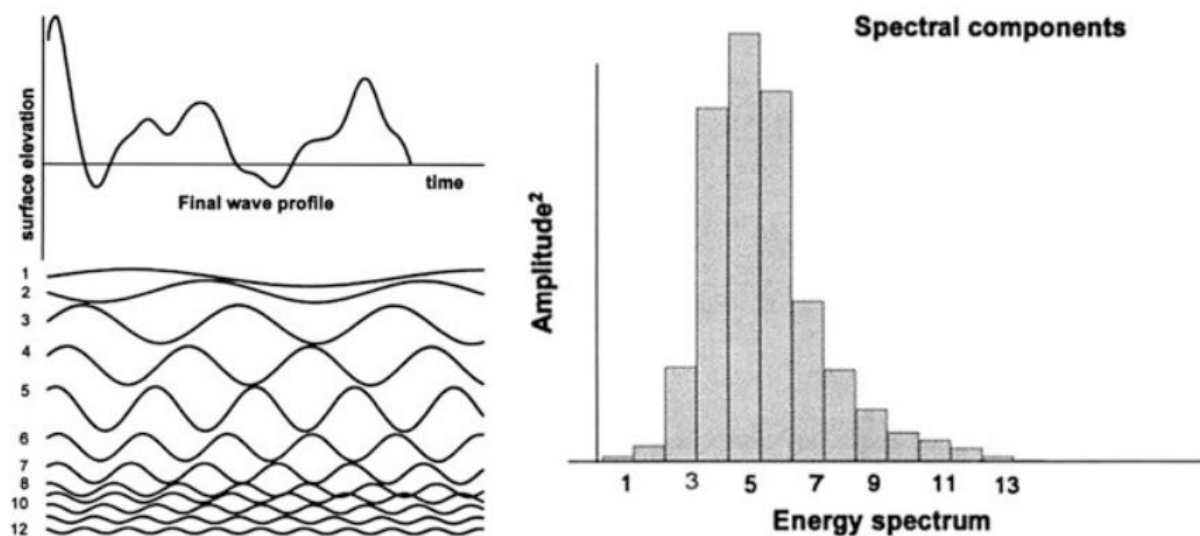
Figure 56: Superposition of waves and classification into a wave spectrum [PK17]

[PK17] specifies that several idealised wave spectra have been developed to model different sea states. One widely used spectrum is the Pierson-Moskowitz (PM) spectrum, which represents a fully developed sea state. The PM spectrum assumes that the waves have reached equilibrium with the wind due to prolonged and extensive wind action over a large water area. In contrast, alternative research has been conducted, such as the *Joint North Sea Wave Observation Project* (JONSWAP), which is applicable in scenarios where the sea state is not fully developed. The spectral variance density $S(\omega)$ for the PM spectrum and JONSWAP spectrum, denoted by equations (15) and (16) respectively, quantify the distribution of wave energy per unit frequency in m^2/Hz. In these equations, ω_p is the peak frequency, g is the gravitational acceleration, ω is the wave component frequency and γ is the peak enhancement factor, defining how the energy is

96

spread over the range of frequencies. For JONSWAP, α depends on the reference wave height.

$$S(\omega) = \frac{\alpha g^2}{\omega^5} \exp\left[-\beta \left(\frac{\omega_p}{\omega}\right)^4\right] \tag{15}$$

$$S(\omega) = \frac{\alpha g^2}{\omega^5} \exp\left[-\frac{5}{4}\left(\frac{\omega_p}{\omega}\right)^4\right] \gamma^{\exp\left[-\frac{(\omega-\omega_p)^2}{2\sigma^2 \omega_p^2}\right]} \tag{16}$$

A comparison between equations (15) and (16) reveals that when the peak enhancement factor of the JONSWAP spectrum is equal to 1.0, the spectra are identical. However, the peak enhancement factor being generally greater than 1.0 results in a higher peak in the spectrum and a concentration of energy on a narrower bandwidth of frequencies. Consequently, it can be deduced that in new and developing seas, where the JONSWAP spectrum is applicable, the bandwidth of frequencies is narrower. This means that the wave components in such seas tend to have similar frequencies, resulting in a more focused distribution of wave energy. In contrast, in fully-developed seas represented by the PM spectrum, the bandwidth of frequencies is broader. This results in the wave energy being spread over a larger range of frequencies, indicating a more dispersed distribution of energy across the spectrum. Due to the influence of various wind sources with different directions, speeds, and fetch lengths, waves can be generated from multiple sources, resulting in the presence of multiple peaks in the wave spectrum. Following figure 57 illustrates a bi-modal sea state associated with two distinct sources of waves.
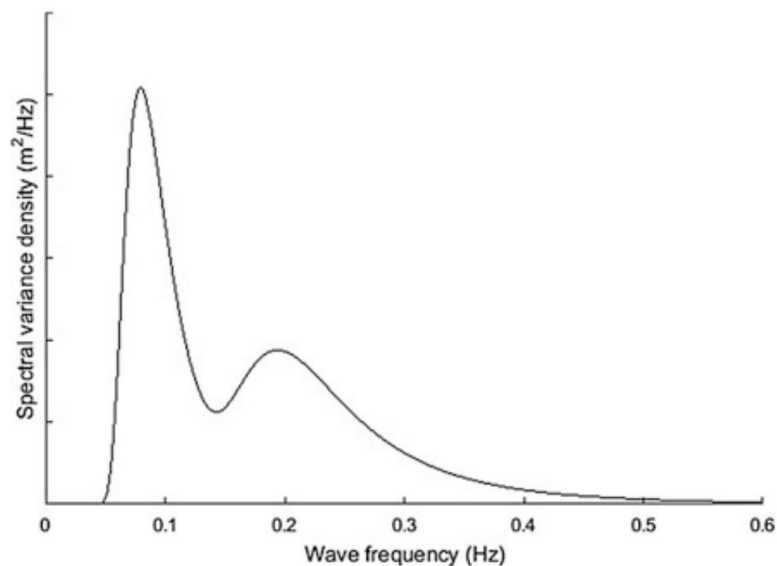
Figure 57: Example spectrum of a bi-modal sea-state [PK17]

A.4 Wind Spectra

A.4.1 Boundary Layer

As described in [YKK20], from a meteorological perspective, the wind profile is considered a part of the *Atmospheric Boundary Layer* (ABL). The ABL represents the lowest portion of the Earth's atmosphere, directly influenced by interactions with the underlying surface. Moreover, it is emphasised that for wind speeds relevant for wind turbines, turbulence is predominantly influenced by shear flow rather than heat exchange. Furthermore, it is described that in offshore conditions, it is reasonable to assume that the ABL has a uniform roughness over the water surface and that horizontal homogeneity holds. These assumptions simplify the modelling process and allow for the consideration of a so-called *Horizontally Homogeneous Turbulent Boundary Layer* (HHTBL).

A.4.2 Wind Speed Profiles

The development of wind flow within a boundary layer introduces spatial variations in wind speed. According to [DNV21b], these variations can be modelled by applying a wind speed profile that accounts for the change in mean wind speed with height above the still water level. The most commonly used approach is to assume a logarithmic wind speed profile, which can be expressed by the following set of equations:

$$
\begin{cases}
U(z) = \frac{u^*}{k_a} \ln \frac{z}{z_0} \\
u^* = \sqrt{\kappa} \cdot U_{10}
\end{cases}
\tag{17}
$$

In the equations, z represents the height above the still water level, and z_0 is a terrain roughness parameter that depends on factors such as wind speed, distance to land, water depth, and wave conditions. The parameter κ denotes the surface friction coefficient, and k_a is a constant known as von Karman's constant, typically assumed to have a value of 0.4. By utilizing this logarithmic wind speed profile, the model can capture the changes in wind speed with height, providing a more realistic representation of wind conditions within the boundary layer. The proximity of the support structure can lead to localised disturbances in wind conditions known as tower influence. Additional models can be implemented to take into account those local influences, which however will not be covered here.

A.4.3 Stationary Model and Development of Wind Spectra

In addition to spatial variations, wind conditions also exhibit temporal variations. As described in classification standard [DNV21a], wind conditions are typically considered stationary over a 10-minute duration, with deviations within this timeframe referred to as turbulence. Variations that extend beyond the this period are described by a long-term wind speed distribution. To address the small-scale natural variability of wind speed within the 10-minute stationary wind assumption, a turbulence model is employed. This turbulence model helps account for the fluctuations and inherent variability in wind speed during that time frame. [DNV21b] specifies that those turbulence can be described by the standard deviation σ_u around the 10-minute mean wind speed U_{10}. Similar for what was done in A.3 for waves, wind speed variations at a specific point in space can be described in the frequency domain using power spectral density. This spectral representation provides information about the distribution of energy across different frequencies, revealing the intensity and dominant frequency components of the wind fluctuations. Figure 59 visually demonstrates the turbulent peak in spectral density. Furthermore, it shows that spectral density remains low for periods between 10 minutes and 2 hours, suggesting infrequent variations in horizontal wind speed over such periods.

To illustrate how the spectrum is developed from site data using the 10-minute mean wind speed U_{10} and its standard deviation σ_u, following equation (18) shows the Davenport spectrum. It was developed to model wind over land and therefore is not accurate for offshore applications. Nevertheless, it is useful to understand the principle of wind spectra. In this equation L_u is a length scale of the wind speed process and is generally taken equal to 1200 meters.

$$S_U(f) = \sigma_U^2 \frac{\frac{2}{3}\left(\frac{L_u}{U_{10}}\right)^2 \cdot f}{\left(1 + \left(\frac{fL_u}{U_{10}}\right)^2\right)^{4/3}} \tag{18}$$

A.4.4 Offshore Wind Turbulence Models

According to [DNV21a], several turbulence models have been developed specifically for modelling offshore wind conditions. These models take into account both the spatial variation of wind speed at different elevations and the temporal variation based on the spectral distribution of wind. Certain turbulence models even have the capability to consider three-dimensional factors that influence wind speed variations. Following figure 58 gives an overview of the most prominent turbulence models for offshore conditions.

Turbulence model	No. components	Industry source	Reference	Additional comments
Kaimal	3D [1]	Wind turbine	IEC 61400-1	
Frøya	1D	Oil and gas	DNV-RP-C205	Also referred to as NPD.
API	1D	Oil and gas	API	
ESDU	3D [1]	Wind turbine	ESDU	Modified form of von-Kármán. Also, referred to as 'improved von Kármán'.
Mann	3D [1]	Wind turbine	IEC 61400-1	Might be a problem to produce long wind files in practice, due to 3D coherence.
1) 3D: correlation of u, v and w components of wind speed in space.				

Figure 58: Summary of commonly used wind turbulence models for offshore conditions [DNV21a]

According to [Orc23b], *OrcaFlex* provides the capability to implement three different turbulent models: those developed by the API (*American Petroleum Institute*), ESDU (*Engineering Sciences Data Unit*), and NPD (*Norwegian Petroleum Directorate*). Comparing the turbulence models in figure 58, it can be observed that both the NPD and API wind spectra are designed to model one-dimensional wind flow, whereas the ESDU spectrum is more suitable for three-dimensional wind flow. Given the focus of this paper on uni-directional wind flow, the ESDU spectrum is not selected as the preferred choice. According to [DNV21b], the NPD spectrum is designed to provide a more refined representation of wind turbulence in the low-frequency range and is therefore is chosen for this study. As by [Orc23b], the spectrum is defined by:

$$S(f, z) = 3.2 U_{\text{ref}}^2 \left(\frac{z}{10} \right)^{0.45} \left[1 + \tilde{f}^n \right]^{-5/3n} , \qquad (19)$$

where n is equal to 0.468, U_{ref} is the reference mean wind speed and $\tilde{f}$ is defined as:

$$\tilde{f}(z) = 172 f \left(\frac{z}{10} \right)^{2/3} \left(\frac{U_{\text{ref}}}{10} \right)^{-3/4} . \qquad (20)$$

It is important to mention that the power spectral density $S(f, z)$ incorporates both spatial and temporal variations of wind speed and therefore is expressed in $[(m/s)^2/Hz]$.

A.4.5 Long-Term Wind Variation

The aforementioned wind turbulence models primarily focus on modelling wind speed variations at the timescale of minutes or seconds. However, [Sia+21] indicates that these models are not suitable for capturing wind variations over longer time periods. This suggests a need

for alternative models to accurately represent long-term wind variations. [Sia+21] categorises wind variations into several levels, each being caused by different phenomena and therefore necessitating the use of distinct models to achieve accurate predictions and forecasts. Figure 59 illustrates the spectral density variation of wind with respect to time periods, demonstrating the distribution of energy within different temporal scales. Three distinct peaks are observed, each corresponding to one of the primary sources of wind speed changes. The first peak corresponds to turbulent variations, encompassing fluctuations in wind speed occurring at the scale of seconds or minutes. The second peak denotes diurnal variations, which encompass wind speed changes based on the time of one day. These changes are influenced by temperature fluctuations between day and night. Finally, the largest peak corresponds to synoptic wind variations, which are influenced by the movement of weather systems and subject to seasonal and annual effects. This research does not delve into the modelling of wind speeds associated with long-term variations observed around the diurnal and synoptic peaks. However, these variations are crucial for calculating the return period of wind speeds and can be represented through statistical approaches, such as the utilisation of a Weibull distribution.
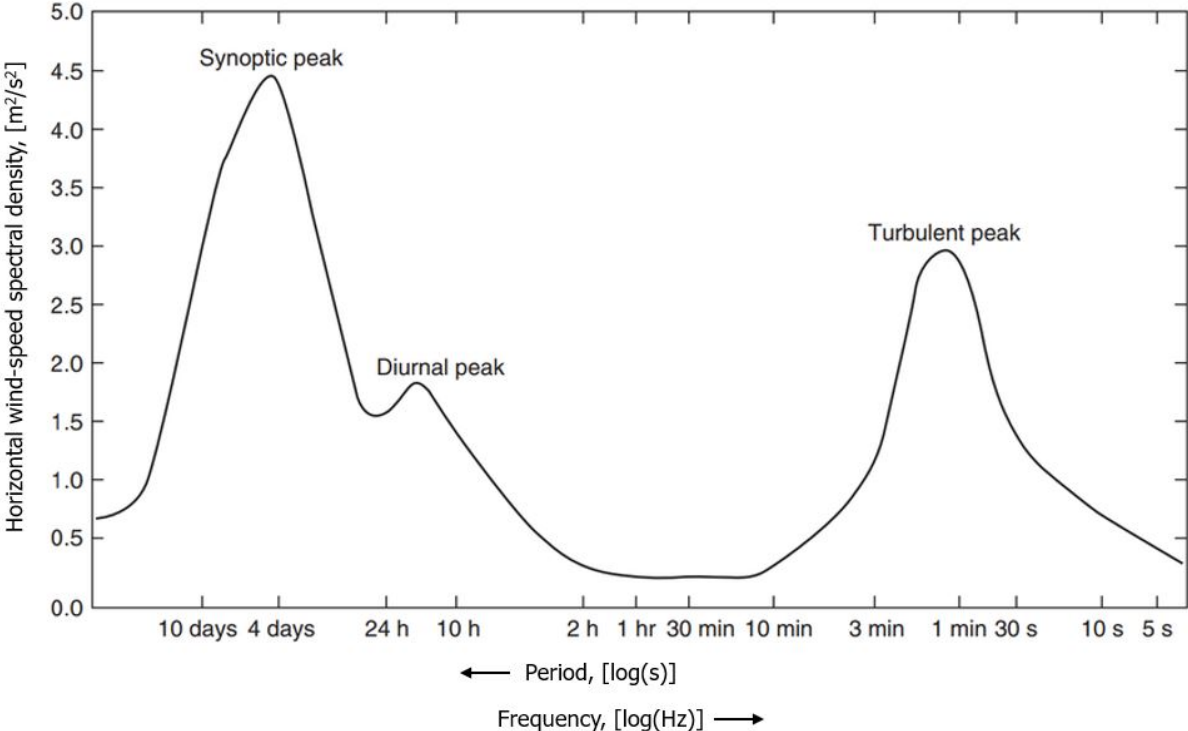
Figure 59: Horizontal wind speed spectral density as a function of the wind frequency [Sia+21]

A.4.6   Comparison of wind and wave spectra

Comparing the distribution of power spectral density of waves and wind offers valuable insights into the distinct characteristics of these phenomena. In the wave spectra (as seen in appendix A.3), one or multiple peaks are observed, typically occurring at periods between 5 and 20 seconds. In contrast, wind spectra exhibit peaks at much higher periods, as clearly illustrated in figure 59. These differences are reinforced by a direct comparison of the two spectra in figure 60. Analysing these spectra together with observations from [Sia+21] and [GKD17] reveals significant dissimilarities. Waves display a well-defined oscillating pattern, characterised by regularly spaced peaks and troughs, reflecting their inherent oscillatory nature. On the other hand, winds tend to maintain a relatively constant profile, in which the only short-term variations are due to turbulence. These turbulent variations lack the organised oscillatory behaviour seen in waves, showing a more irregular behaviour instead. In conclusion, according to [Vel+19], waves, with their well-defined oscillations at much lower periods, pose a greater risk for resonance phenomena in offshore structures compared to wind.
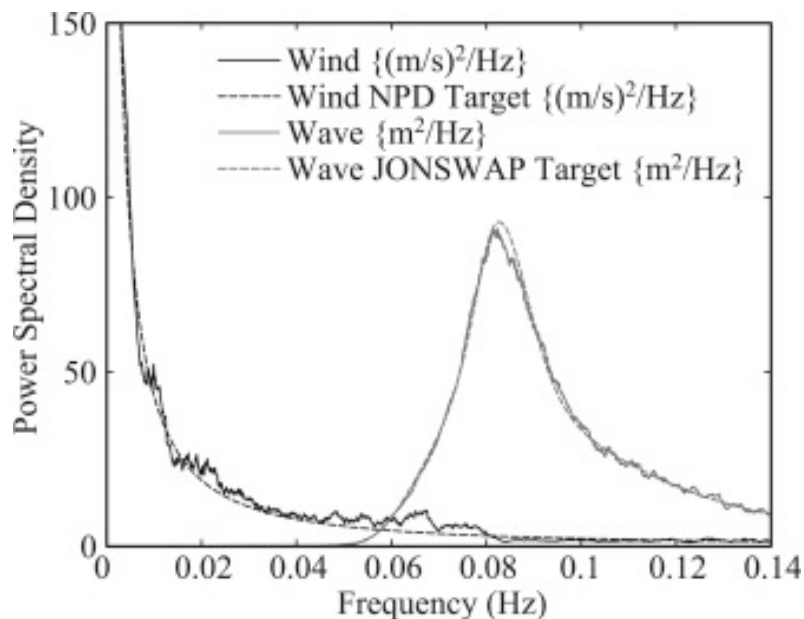
Figure 60: Comparison between the power spectral density for wind and waves [GKD17]

A.5 Blade Element Momentum Theory

As by [LRS21], the *Blade Element Momentum Theory* (BEMT) is a model that assesses the performance of a propelling or extracting turbine based on its geometric properties and the characteristics of the interacting flow. BEMT combines two theories, namely the *Blade Element Theory* and the *Momentum Theory*, which is further divided into the *Axial Momentum Theory* and the *Tangential Momentum Theory*.

A.5.1 Axial Momentum Theory

According to [Mou14], the rotor of a wind turbine is regarded as a uniform actuator disc that introduces a pressure discontinuity in a steady, incompressible, and uniformly homogeneous flow, as depicted in figure 61.
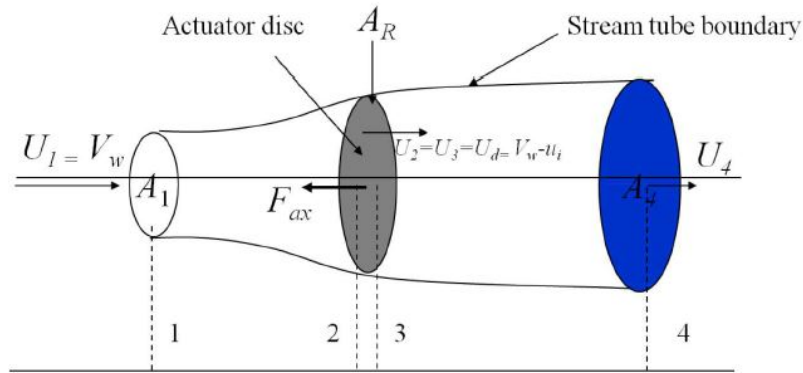
Figure 61: Stream tube with indicated velocities [Mou14]

Applying the principles of mass, momentum, and energy conservation on the 1D stream tube passing through this actuator disc, the *Axial Momentum Theory* derives expressions for the mass flux $\dot{m}$, thrust force T, and power extracted by the actuator disc P_{ow}:

$$
\begin{cases}
\dot{m} = \rho U_1 A_1 = \rho U_d A_d = \rho U_4 A_4 \\[2mm]
T = \dot{m} \left(U_4 - U_1 \right) \\[2mm]
P_{ow} = T U_d = \tfrac{1}{2} \dot{m} \left(U_1^2 - U_4^2 \right)
\end{cases}
\tag{21}
$$

In these equations, U_i and A_i are the velocities and sectional surface areas of the stream tube shown if figure 61 respectively and ρ is the fluid density. By defining the axial induction factor a as the decrease of the wind velocity at the rotor plane U_d with respect to the free stream wind velocity U_∞ (denoted as U_1 in figure 61):

$$a = \frac{U_\infty - U_d}{U_\infty} \; , \tag{22}$$

the axial thrust can be expressed as:

$$T = \dot{m} \left(U_4 - U_1 \right) = \rho U_\infty^2 2a(1-a) A_r \; , \tag{23}$$

with A_r the surface area of the rotor plane.
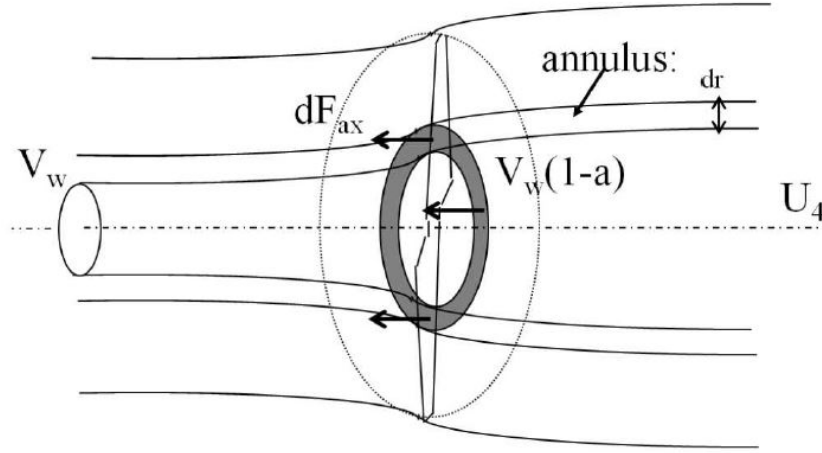
Figure 62: Division of the surface area of the rotor plane into annular rings [Mou14]

By dividing the rotor surface area into annular rings, as shown in figure 62, the axial thrust force is expressed as a function of the radius:

$$dT(r) = \rho U_\infty^2 4a(1-a)\pi r \; dr \tag{24}$$

A.5.2 Tangential Momentum Theory

As by [Mou14], the *Tangential Momentum Theory* derives an expression for the torque in the rotor plane by applying the conservation law for angular momentum to an infinitesimal ring of the rotor disc.

$$dQ(r) = \dot{m}r \left(\omega_1 r - \omega_4 r \right) \tag{25}$$

Where $\dot{m}$ represents the mass flow passing through the rotor plane, $\omega_1 r$ and $\omega_2 r$ correspond to the rotational velocities of the upstream and downstream flows respectively, and r denotes the radius of the annular ring of infinitesimal thickness. By utilising equation (22) and the first

equation in (21), and assuming a uniform and non-rotating upstream flow (which allows us to set ω_1 to zero), the torque in the infinitesimal ring expresses as follows:

$$dQ(r) = \rho U_\infty 2(1-a)r^3 \omega_4 \pi \ dr \ , \tag{26}$$

where ω_4 represents the wake rotation in [rad/s], which can be expressed in terms of the angular induction factor a', describing the following relationship:

$$\omega_4 = 2a'\Omega \ . \tag{27}$$

Finally, by combining equation (26) and (27), the torque expresses as:

$$dQ(r) = \rho U_\infty 4a'(1-a)r^3 \Omega \pi \ dr \ . \tag{28}$$

A.5.3 Blade Element Theory

According to [Mou14], the *Blade Element Theory* is employed to assess the aerodynamic forces exerted on individual sections of the blade, taking into account their geometric properties and the inflow angle. The flow is assumed to be steady, incompressible, and two-dimensional, as well as uniform, homogeneous, and non-turbulent. For each section along the radius of the blade, the angles and velocities can be defined as depicted in figure 63.

By defining the relative inflow angle ϕ as the sum of the sectional angle of incidence α, the geometric twist angle θ and the pitch angle of the blade β:

$$\phi = \alpha + \theta + \beta \ , \tag{29}$$

the contribution of the thrust and torque per section dr are expressed in terms of the lift and drag forces acting on that particular section.

$$\begin{cases} dT(r) = B\frac{1}{2}\rho U_{rel}^2 \left(C_l \cos(\phi) + C_d \sin(\phi)\right) c \ dr \\ dQ(r) = B\frac{1}{2}\rho U_{rel}^2 \left(C_l \sin(\phi) - C_d \cos(\phi)\right) cr \ dr \end{cases} \tag{30}$$

In the given equations, B represents the number of blades, r denotes the radial position, and c the chord length of the local section. The lift coefficient is represented by C_l, while the drag coefficient is denoted by C_d. To accurately calculate the relative velocity U_{rel}, it is necessary to
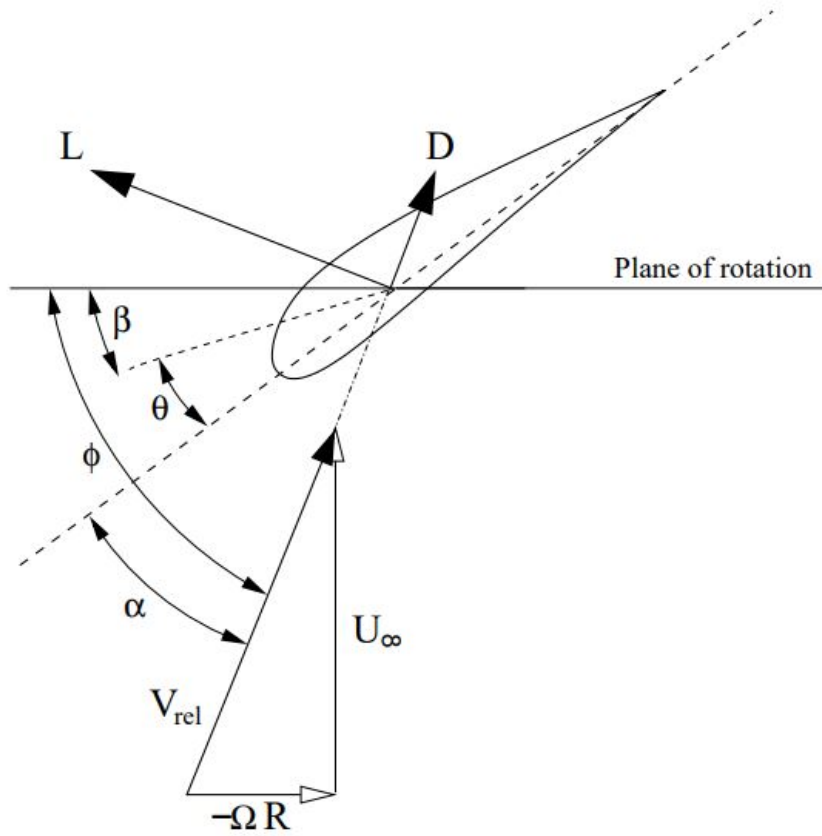
Figure 63: Angles and velocities for a blade section [Mou14]

consider the rotational velocity of the blade. By referring to figure 63, the following expressions for the relative velocity and relative inflow angle can be determined:

$$\begin{cases} U_{rel} = \sqrt{(U_\infty(1-a))^2 + (\Omega r\,(1+a'))^2} \\ \phi = \arctan\left(\frac{U_\infty(1-a)}{\Omega r(1+a')}\right) \end{cases} \quad (31)$$

where U_∞ corresponds to the free stream fluid velocity in [m/s] and Ω to the rotational velocity of the blade in [rad/s]. By using the speed ratio, which is defined as

$$\lambda_r = \frac{\Omega r}{U_\infty}\,, \quad (32)$$

it is finally possible to derive a relation between the two induction factors:

$$\tan(\phi) = \frac{1-a}{\lambda_r\,(1+a')} \quad (33)$$

$$\Leftrightarrow \quad a = 1 - \tan(\phi)\lambda_r\,(1+a') \quad (34)$$

106

A.5.4 General Principle of the Blade Element Momentum Theory

As explained in [Mou14], when the *Momentum Theory* is coupled with the *Blade Element The-ory*, it gives rise to the *Blade Element Momentum Theory*, which is used in practice to analyse and assess the forces and performance of a rotor. By combining the expressions for thrust and torque derived from both methods, specifically equations (24) and (28) for the *Momentum Theory*, and equation (30) for the *Blade Element Theory*, the following system of equations is obtained:

$$
\begin{cases}
U_\infty^2 4a(1-a)\pi r = Bc\frac{1}{2}U_{rel}^2\left(C_l\cos(\phi) + C_d\sin(\phi)\right) \\[2mm]
4a'(1-a)U_\infty\pi r^2\Omega = Bc\frac{1}{2}U_{rel}^2\left(C_l\sin(\phi) - C_d\cos(\phi)\right)
\end{cases}
\tag{35}
$$

Combining those equations with (31) and (34), we obtain the following set of equations:

$$
\begin{cases}
\phi = \arctan\left(\frac{1-a}{\lambda_r(1+a')}\right) \\[2mm]
\alpha = \phi - (\theta + \beta) \\[2mm]
\frac{a}{(1-a)} = \frac{Bc(C_l(\alpha)\cos(\phi) + C_d(\alpha)\sin(\phi))}{8\pi r\sin(\phi)^2} \\[2mm]
\frac{a'}{(1+a')} = \frac{Bc(C_l(\alpha)\sin(\phi) - C_d(\alpha)\cos(\phi))}{4\pi r\sin(2\phi)}
\end{cases}
\tag{36}
$$

For a given wind velocity, blade geometry, and operating conditions, this system of equations provides a complete description of the problem. With the availability of aerodynamic data for each section of the blade profile, an iterative approach can be employed to solve these equations. The iterative scheme used in BEMT involves initialising the induction factors with an initial guess, which are then updated at each iteration. The influence of the wind velocity and operating conditions is captured by the speed ratio λ_r defined in equation (32). Once this set of equations is solved, additional properties such as thrust and torque can be determined. This can be accomplished by applying either the equations derived from the Momentum Theory (equations (24) and (28)) or the Blade Element Theory (equations (30)). By repeating this procedure for every section dr along the radius of the blade, a solution for the entire blade can be obtained. Summing up the sectional values of thrust and torque provides the total thrust and torque per blade.

A.6   Aerodynamic Loads in *OrcaFlex*

As described in [Orc23b], the implementation of the BEMT model within *OrcaFlex* is slightly different to the one described in appendix A.5. However, they rely on the same principles. Aerodynamic loads due to the wind inflow at velocity w and incidence angle α are calculated individually at the aerodynamic centre of each blade mid-segment illustrated in figure 64.
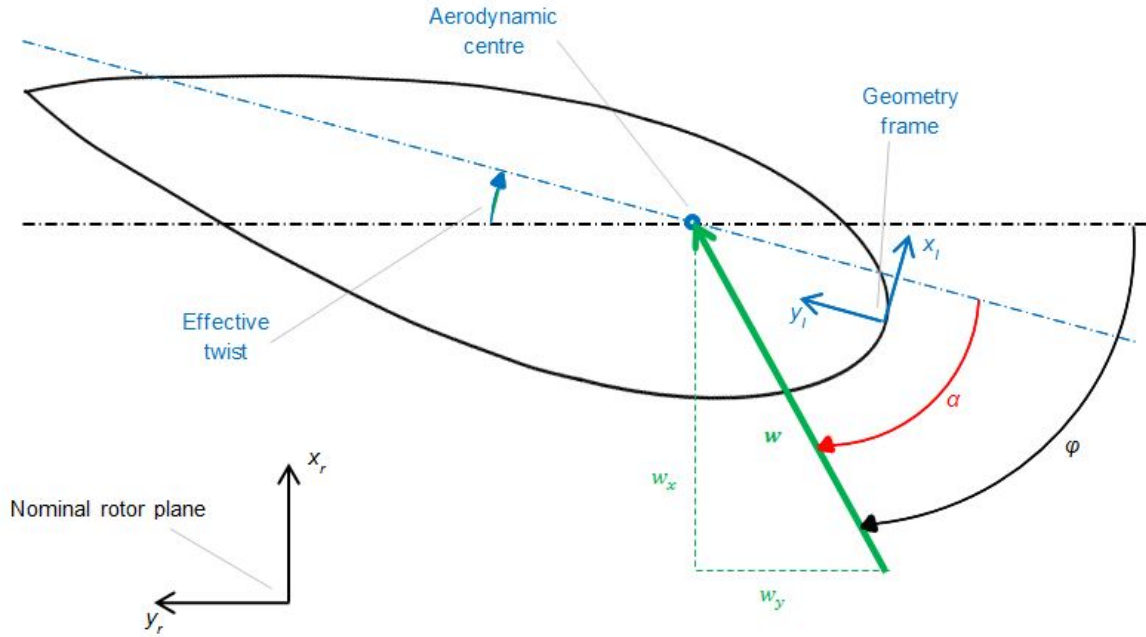
Figure 64: Blade section modelling in *OrcaFlex* [Orc23b]

The lift force (f_L), drag force (f_D), and pitching moment about the z-axis (m_z) can be expressed as follows:

$$\begin{cases} f_L = \frac{1}{2}\rho A C_l(\alpha)|\boldsymbol{w}|^2 \\[2mm] f_D = \frac{1}{2}\rho A C_d(\alpha)|\boldsymbol{w}|^2 \\[2mm] m_z = \frac{1}{2}\rho A c C_m(\alpha)|\boldsymbol{w}|^2 \end{cases} \tag{37}$$

where ρ represents the air density, c denotes the chord length, A corresponds to the element area (which is the product of the chord and the segment length), and C_l, C_d, and C_m are the lift coefficient, drag coefficient, and moment coefficient, respectively.

The *Blade Element Momentum Theory* is utilised to consider the induction effects caused by the rotor. This theory involves the calculation of the axial and tangential induction factors, denoted as a and a' respectively. These factors are used to express the inflow velocity w as a function of the free stream velocity v. It is assumed that there is no flow along the blade axis, resulting in a

relative flow in the z-direction of zero.

$$
\begin{cases}
w_{\mathrm{x}} = (1 - a)v_{\mathrm{x}} \\[2mm]
w_{\mathrm{y}} = (1 + a')v_{\mathrm{y}} \\[2mm]
w_{\mathrm{z}} = 0
\end{cases}
\tag{38}
$$

As the turbine element in *OrcaFlex* supports a pre-cone angle, as well as blade deflection, a nominal rotor plane frame of reference is defined for each blade segment and it is in this plane that the BEMT method is applied. The lift and drag coefficients in this nominal rotor plane depend on the angle of attack α and express as:

$$
\begin{cases}
C_{\mathrm{x}}(\alpha) = C_{\mathrm{l}}(\alpha)\cos\phi + C_{\mathrm{d}}(\alpha)\sin\phi \\[2mm]
C_{\mathrm{y}}(\alpha) = C_{\mathrm{d}}(\alpha)\cos\phi - C_{\mathrm{l}}(\alpha)\sin\phi
\end{cases}
\tag{39}
$$

Where ϕ is the angle between the inflow velocity w and the nominal rotor plane y-axis. Furthermore, two non-dimensional parameters κ and κ' are defined as:

$$
\begin{cases}
\kappa & = \dfrac{\sigma C_{\mathrm{x}}(\alpha)}{4F\sin^2\phi} \\[4mm]
\kappa' & = -\dfrac{\sigma C_{\mathrm{y}}(\alpha)}{4F\sin\phi\cos\phi}
\end{cases}
\tag{40}
$$

where σ is the local blade solidity, defined by:

$$
\sigma = \frac{n_{\mathrm{B}}c}{2\pi r} \; ,
\tag{41}
$$

and n_{B} the number of blades, c the local chord length and r the instantaneous radius. The term F is used to incorporate additional correction factors, and its value is 1 when no correction is applied. The expression of the axial induction factor a depends on the operating region of the turbine. In the momentum/empirical region ($\phi v_x > 0$), it is given by:

$$
a =
\begin{cases}
\dfrac{\kappa}{1+\kappa} & \text{if } \kappa \leq \frac{2}{3} \\[4mm]
\dfrac{\gamma_1 - \sqrt{\gamma_2}}{\gamma_3} & \text{otherwise}
\end{cases}
\tag{42}
$$

In the propeller brake region ($\phi v_x \leq 0$), the expression is:

$$
a = \frac{\kappa}{1 - \kappa}
\tag{43}
$$

The empirical coefficients are defined as follows:

$$
\begin{cases}
\gamma_1 = 2F\kappa - \left(\frac{10}{9} - F\right) \\[2mm]
\gamma_2 = 2F\kappa - F\left(\frac{4}{3} - F\right) \\[2mm]
\gamma_3 = 2F\kappa - \left(\frac{25}{9} - 2F\right)
\end{cases}
\tag{44}
$$

The tangential induction factor, in contrast, is independent of the region and expresses as:

$$
a' =
\begin{cases}
\frac{\kappa'}{1-\kappa'} & \text{if } v_\mathrm{x} > 0 \\[3mm]
\frac{-\kappa'}{1+\kappa'} & \text{otherwise}
\end{cases}
\tag{45}
$$

[Orc23b] finally defines the residual function $\mathcal{R}(\phi)$ as:

$$
\mathcal{R}(\phi) = \frac{\sin\phi}{1-a} - \frac{v_\mathrm{x}}{v_\mathrm{y}}\left(1 - \kappa'\right)\cos\phi
\tag{46}
$$

The equation $\mathcal{R}(\phi) = 0$ is solved iteratively to determine the values of the induction factors. These induction factors are then used to calculate the inflow velocity $\boldsymbol{w}$, which is further used to compute the aerodynamic loads acting on the blade section. *OrcaFlex* employs a bracketed root finding algorithm for the iterative scheme.

A.7 Turbine Aerodynamic Model Enhancements

This appendix provides a detailed presentation of the theoretical foundations underlying the aerodynamic model enhancements utilised in section 7. The majority of explanations are sourced from the *OrcaFlex* website, supplemented by additional in-depth research where necessary.

A.7.1 Tip and Hub Losses

According to [Bra17], when comparing a two-dimensional wing configuration to a three dimensional wing with finite span, significant differences in both kinematics and dynamics are observed. These disparities, commonly known as "tip losses", are most pronounced at the outer sections of the rotor blades. They arise due to the circulation flow that occurs at the wingtip, where the pressure equalises between the suction and pressure sides of the airfoil. In addition to tip losses, there are also "hub losses" present at the inner sections of the rotor blades. These losses occur due to the obstruction caused by the tower and the turbine hub. The presence of these structures disrupts the flow near the hub, resulting in lower air velocities, altered flow angles, and changes in the aerodynamic forces experienced by the blades. These effects are corroborated by [Mou14], where a comparison was made between BEMT and CFD results. The study revealed that the BEMT method yields accurate outcomes for blade sections located in the middle. However, in regions near the root and tip, the BEMT method tends to overestimate the pressure differences between the suction and pressure sides of the blade, leading to an overestimation of the aerodynamic forces.

To account for the impacts at the blade extremities, *OrcaFlex* has the possibility to integrate a correction factor $F = F_{\text{tip}} F_{\text{hub}}$ into the computation of the induction factors, as described in equations (40) and (44) provided in appendix A.6. According to [Orc23b], Prandtl's loss factor correction is utilised and can be expressed as:

$$\begin{cases} F_{\text{tip}} & = \frac{2}{\pi} \cos^{-1} \left\{ \exp \left(-\frac{1}{2} n_{\text{B}} \frac{x_{\text{b}} - x}{(x + r_{\text{hub}}) |\sin \phi|} \right) \right\} \\ F_{\text{hub}} & = \frac{2}{\pi} \cos^{-1} \left\{ \exp \left(-\frac{1}{2} n_{\text{B}} \frac{x}{r_{\text{hub}} |\sin \phi|} \right) \right\} \end{cases} \tag{47}$$

where x_{b} represents the blade length, x is the unstretched mid-segment arc length, n_{B} denotes the number of blades, and r_{hub} corresponds to the hub radius. In the absence of tip loss correction or hub loss correction, the values of F_{tip} and F_{hub} are equal to one, respectively.

A.7.2 Dynamic Inflow

According to the documentation provided in [Orc23b], the general BEMT method incorporates the equilibrium wake assumption, meaning that the induced velocities are calculated directly from the instantaneous flow conditions. This assumption implies that the wake reacts instantaneously to changes in the flow. This principle is applied in equation (38), where the term $\boldsymbol{v_q} = (-av_{\mathrm{x}}\ ,\ a'v_{\mathrm{y}}\ ,\ 0)$ corresponds to the quasi-steady induced velocity. However, in reality, the wake response takes time to adapt to changes in the flow conditions. To account for the physics associated with the delayed wake response, the *Øye Dynamic Inflow Model* can be optionally activated. This model incorporates a series of first-order filters to approximate the "dynamic induced velocity" $\boldsymbol{v_d}$. Consequently, the inflow velocity $\boldsymbol{w}$ used in equation (37) is now expressed as $\boldsymbol{w} = \boldsymbol{v} + \boldsymbol{v_d}$ instead of $\boldsymbol{w} = \boldsymbol{v} + \boldsymbol{v_q}$. The filters applied in this dynamic model correspond to solving the following set of equations:

$$
\begin{cases}
\dot{\boldsymbol{v}}_{\mathrm{int}} = \frac{1}{\tau}\boldsymbol{v}_{\mathrm{q}} + 0.6\dot{\boldsymbol{v}}_{\mathrm{q}} - \frac{1}{\tau}\boldsymbol{v}_{\mathrm{int}} \\[2mm]
\dot{\boldsymbol{v}}_{\mathrm{d}} = \frac{1}{\tau'}\left(\dot{\boldsymbol{v}}_{\mathrm{int}} - \boldsymbol{v}_{\mathrm{d}}\right) \\[2mm]
\tau = \frac{1.1}{1-1.3\bar{a}}\frac{r_{\mathrm{x}}}{\bar{v}_{\mathrm{a}}} \\[2mm]
\tau' = \left[0.39 - 0.26\left(\frac{r}{r_{\mathrm{x}}}\right)^2\right]\tau
\end{cases}
\tag{48}
$$

where r_{x} represents the maximum instantaneous radius, $\bar{v}_{\mathrm{a}}$ denotes the mean disturbed flow velocity, and $\bar{a}$ represents the mean axial induction, each calculated over all blade elements.

A.7.3 Skewed Wake Correction

To account for the non-uniform flow patterns in the wake resulting from the rotational movement of the wind turbine rotor, *OrcaFlex* provides the capability to incorporate a skewed wake correction by adjusting the induction factor "a" defined in equations (42) and (43). This modification is defined as:

$$
a_{\mathrm{skew}} = a\left(1 + F_s\frac{r}{r_{\mathrm{x}}}\tan\frac{\chi}{2}\sin\psi\right)\ ,
\tag{49}
$$

with ψ the segment azimuth angle, χ the wake skew angle and F_s a user-specified skewed wake factor. Although [And+14] indicates that the effects of a skewed wake are most pronounced during yaw operation, it also suggests that skewed wake effects can occur even under normal operating conditions due to the uneven distribution of flow velocities in the wake caused by rotor

rotation. Therefore, despite the uniform wind direction assumed in the conducted simulations, it is important to investigate the potential significance of skewed wake effects.

A.8   Structural Dynamics

This appendix presents a thorough explanation of the theoretical foundations underlying the modelling sensitivity analysis of the rotor structural dynamics conducted in section 7.

A.8.1   *Structural Damping*

As described in [Geo18], structural damping quantifies the rate of energy dissipation during vibrations. In numerical simulations, the mathematical Rayleigh damping model can be employed to address two specific objectives:

1. Account for energy dissipation at low shear strain levels.

2. Dampen out spurious oscillations that arise in the high-frequency domain. These oscillations, often accompanied by high-frequency noise, can lead to computational instability, particularly in systems with a large number of degrees of freedom.

The utilisation of Rayleigh damping helps mitigate these issues and improves the accuracy and stability of numerical analyses. When utilising an implicit integration scheme, Rayleigh damping is available in *OrcaFlex* for both line elements and turbine blades. As stated in [Orc23b], Rayleigh damping in *OrcaFlex* entails the creation of a system damping matrix $\boldsymbol{C}$, which is used to determine the damping loads incorporated into the equation of motion (3). Two types of structural damping are available, the first being the *Classical Rayleigh Damping*, where the damping matrix is formulated as

$$\boldsymbol{C} = \mu\boldsymbol{M} + \lambda\boldsymbol{K} \ , \tag{50}$$

with $\boldsymbol{M}$ and $\boldsymbol{K}$ representing the structural mass and stiffness matrices, respectively. The coefficients μ and λ are the mass and stiffness proportional Rayleigh damping coefficients. The second type of structural damping the *Separated Rayleigh Damping*, which divides the stiffness matrix and coefficient to its contribution to axial, bending and torsional deformation, allowing for different damping ratios and writing as

$$C = \mu M + \lambda_a \mathbf{K}_a + \lambda_b \mathbf{K}_b + \lambda_t \mathbf{K}_t \ . \tag{51}$$

where $\boldsymbol{K}_a$, $\boldsymbol{K}_b$ and $\boldsymbol{K}_t$ are the stiffness matrices associated with axial, bending, and torsional deformations, respectively. The coefficients λ_a, λ_b and λ_t represent the damping ratios for each deformation mode.

A.8.2 Finite Element Representation:

According to [Orc23b], the most accurate and therefore most prominent method for modelling lines or pipes in *OrcaFlex* is the finite element method. As shown in figure 65, the discretised line model consists of a series of straight model segments with a node at each end. The model segments represent the axial and torsional properties of the line, being represented as spring-damper elements. All other properties of the line, such as mass, buoyancy, drag, etc. are modelled at the nodes, whereas each node includes the properties of the two half-segments at either side. All forces and moments are then applied at those nodes, with the exception of the weight that can be applied with an offset.
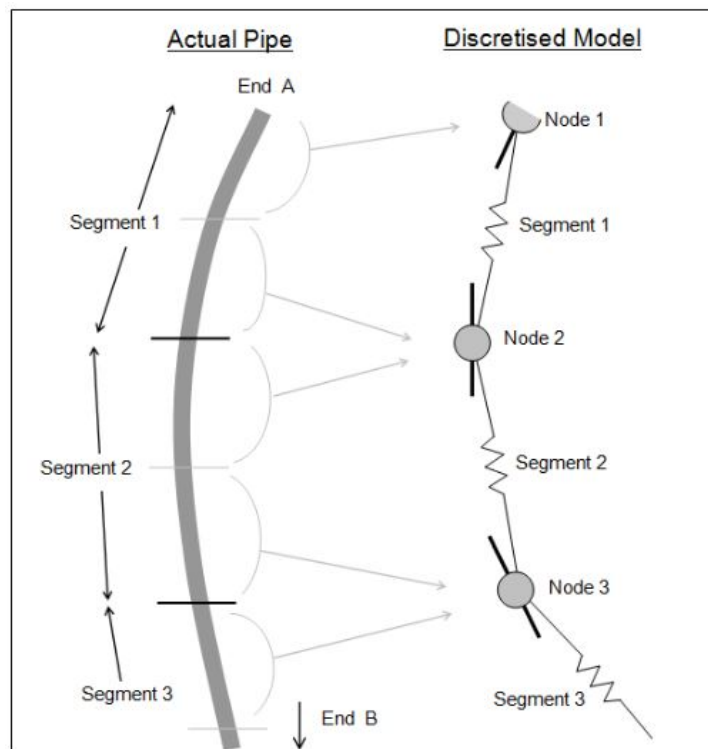
Figure 65: Finite element modelling of pipes and lines in *OrcaFlex* [Orc23b]

A.9 Pearson Product-Moment Correlation

According to [Sta20], the Pearson product-moment correlation coefficient, commonly represented as r, is used to quantify the strength of a linear relationship between two variables. The coefficient measures the degree to which the data points deviate from the best-fit line that represents the relationship between the variables. In other words, it assesses how well the data points align with the proposed linear model. According to [POD08] the Pearson correlation coefficient for a samples of size n with the two variables x and y expresses as:

$$r = \frac{1}{n-1} \sum_{i=1}^{n} \left(\frac{x_i - \bar{x}}{s_x} \right) \left(\frac{y_i - \bar{y}}{s_y} \right) = \frac{1}{n-1} \sum_{i=1}^{n} z_{x,i} \, z_{y,i} \,, \tag{52}$$

with the mean, standard deviation and standard score defined as:

$$\bar{x} = \frac{1}{n} \sum_{i=1}^{n} x_i \,, \tag{53}$$

$$s_x = \sqrt{\frac{1}{n-1} \sum_{i=1}^{n} (x_i - \bar{x})^2} \,, \tag{54}$$

$$z_{x,i} = \left(\frac{x_i - \bar{x}}{s_x} \right) \,. \tag{55}$$

To provide insight into the origin of these relations, figure 66 illustrates the standard scores of a sample with two variables, x and y. In regions I and III, the product of the standard scores $(z_{x,i} \cdot z_{y,i})$ is positive, indicating a positive relationship between the variables. Conversely, in regions II and IV, the product is negative, indicating a negative relationship. In figure (a), where a positive correlation ($r > 0$) is observed, the product of the standard scores is predominantly positive. On the other hand, in figure (b), a negative correlation ($r < 0$) is evident as the product of the standard scores is mostly negative.

In [Sta20], the connection between the distribution of a sample and the value of the correlation coefficient is made, as illustrated in figure 67. Additionally, [POD08] states that correlation coefficients with absolute values below 0.5 indicate a weak correlation, while coefficients above 0.8 indicate a strong correlation. It is important to note that the correlation coefficient does not represent the slope of the line of best fit. A correlation coefficient of +1 or -1 indicates that there is no variation between the data points and the line of best fit. In other words, the data points perfectly align with the line.
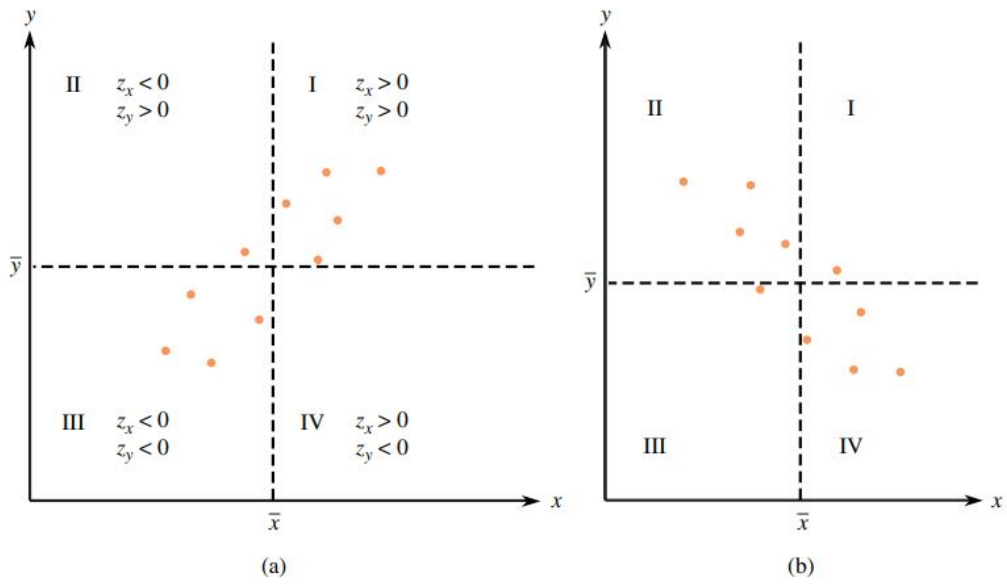
Figure 66: Standard scores of a sample showing a positive and negative correlation [POD08]
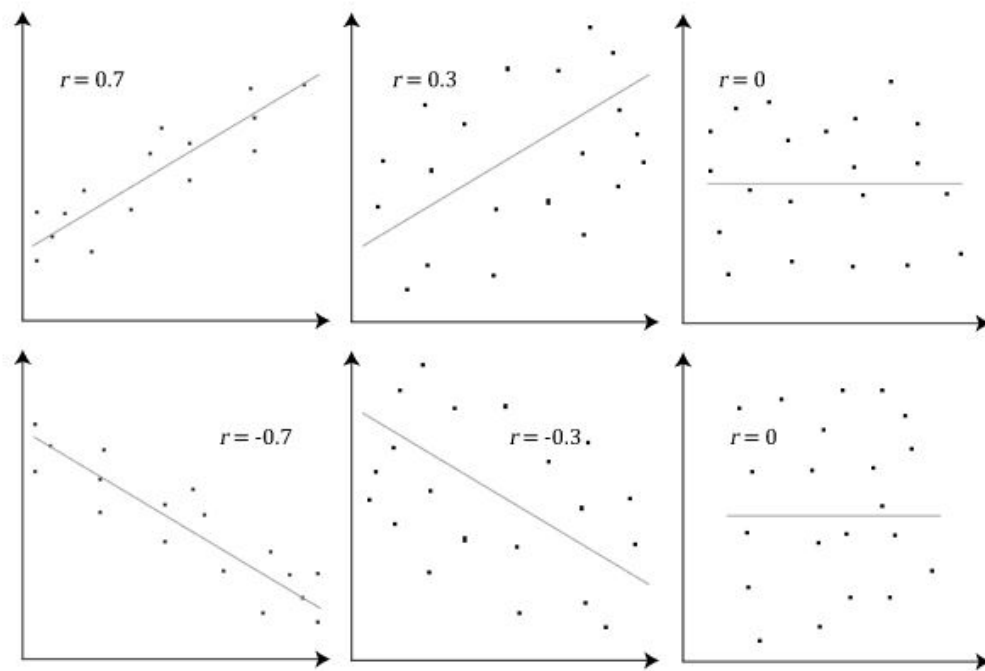
Figure 67: Sign and value of the Pearson correlation coefficient for different samples [Sta20]

B APPENDIX - ADDITIONAL EXPLANATIONS

This appendix provides supplementary information that supports the choices and decisions made in the main body of the paper. While not critical to the main analysis, these details are important for a comprehensive understanding of the study. Appendix B.1 justifies the selection of the reference wind turbine and provides details about certain characteristics. Additionally, appendix B.2 delves into the analytical expression and the physical interpretation of the torque and thrust factors employed in section 8.4.3.

B.1 Choice of the Reference Wind Turbine

To study the modelling of floating offshore wind turbines, a reference configuration must be selected. In section 2, a semi-submersible floater type is chosen as substructure. The size of the turbine is selected based on observations from the offshore wind industry. In recent years, a trend of increasing turbine sizes has been seen, from 3 MW in 2010 to 8 MW in 2016, with a projected target of 15-20 MW turbines by 2030, as discussed in [IEA19]. Considering the aim of this study to facilitate dynamic modelling for future years, a turbine of 15 MW size is therefore chosen. The selected turbine is the *15 MW Offshore Reference Wind Turbine* provided by the *IEA Wind TCP Task 37*. This choice is based on the availability of extensive information in literature. For the reference floater, the *VolturnUS-S Reference Platform* developed at the University of Maine (UMaine) is chosen. This selection is based on the substantial amount of information available in literature and the availability of a predefined *OrcaFlex* model, which will be used as a base case for dynamic analyses. Detailed descriptions of the reference wind turbine and the floating substructure can be found in the technical reports [Gae+20] and [All+20], respectively. Key values are available in figures 77 and 78 in appendix C.3.

B.1.1 Control System and Turbine Performance

Special attention is dedicated to the performance of the FOWT across its operational wind speed range, spanning from 3 to 25 m/s. The control strategy employed is a variable speed-variable pitch (VS-VP) controller, as depicted in figure 68. Just below the rated wind speed of 10.59 m/s, the blade pitch remains fixed at 0°, and above the rated wind speed, the pitch angle is increased to maintain a constant rotor speed of 7.56 RPM. Figure 68 highlights the constant tip speed ratio (TSR) in region 2, which is desirable for optimal power extraction, as discussed in appendix A.2.

It is important to note that the thrust force reaches its peak at the rated wind speed, resulting in the highest aerodynamic forces experienced by the turbine.
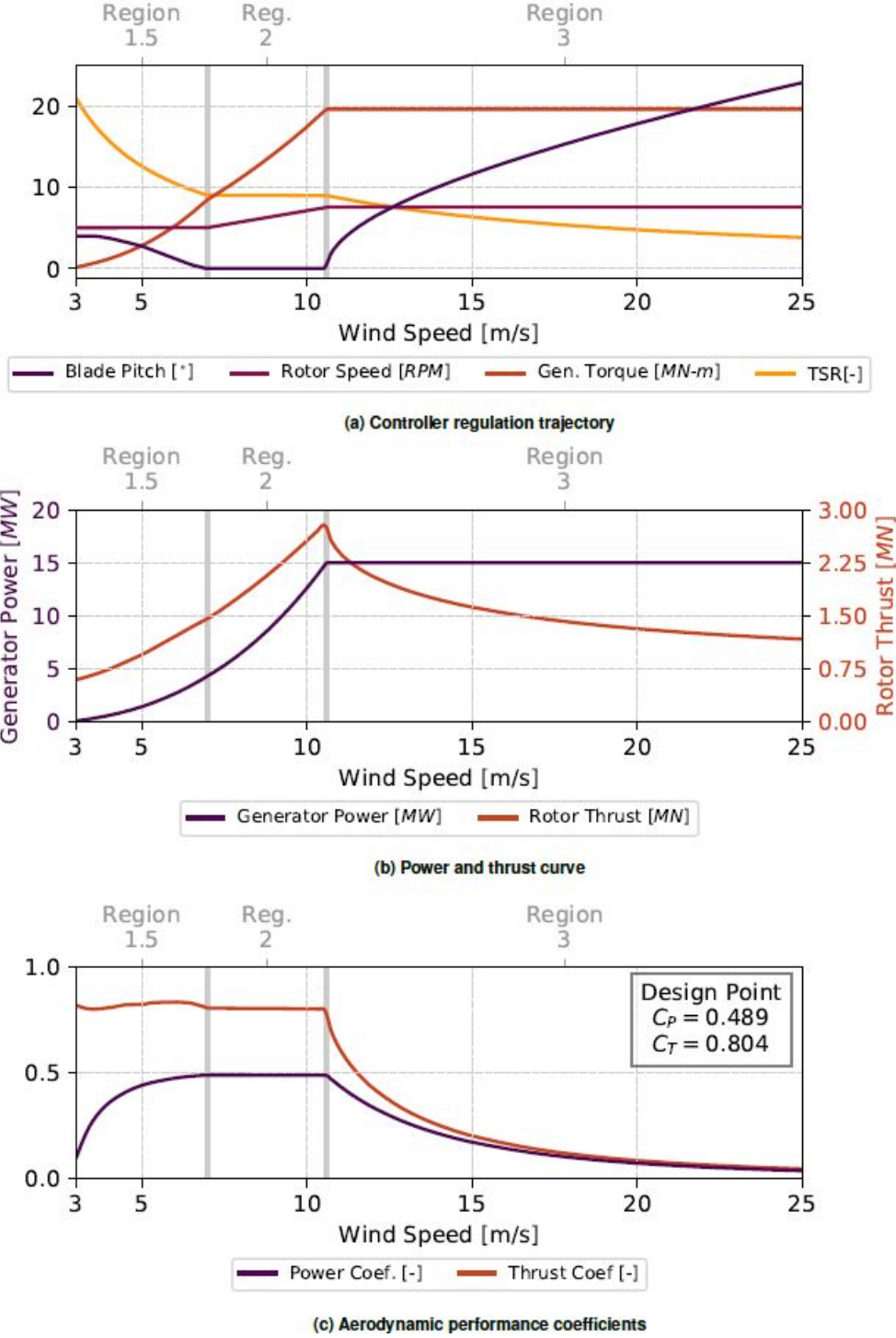
Figure 68: Performance and operation of the 15-MW Reference FOWT [Gae+20]

B.1.2 OrcaFlex Model

From [Orc23a], an *OrcaFlex* model for the above described reference FOWT is obtained. Minor discrepancies exist between this model and the data presented in [Gae+20] and [All+20]. However, as the focus of this study is on exploring model simplifications, these differences are considered minor and the representation provided in [Orc23a] is considered as reference.

B.1.3 Finite Element Representation of the Rotor

As outlined in section 4.3.4, modelling of wind turbines in *OrcaFlex* is done through the incorporation of FAST software. To account for aerodynamic forces, the BEMT model is employed, as detailed in appendix A.5. To accurately capture the aerodynamic behaviour, a refined representation of the blades is necessary. Figure 69 illustrates the adoption of a finite element approach to model the blades. Each node along the blade corresponds to a specific aerodynamic shape, determined by a predefined wing type with known lift and drag coefficients, named C_l and C_d in equation (30). Given that each blade spans a length of 117 meters and is divided into 50 nodes, the computation of aerodynamic loads constitutes a significant portion of the simulation time and requires considerable computational efforts.
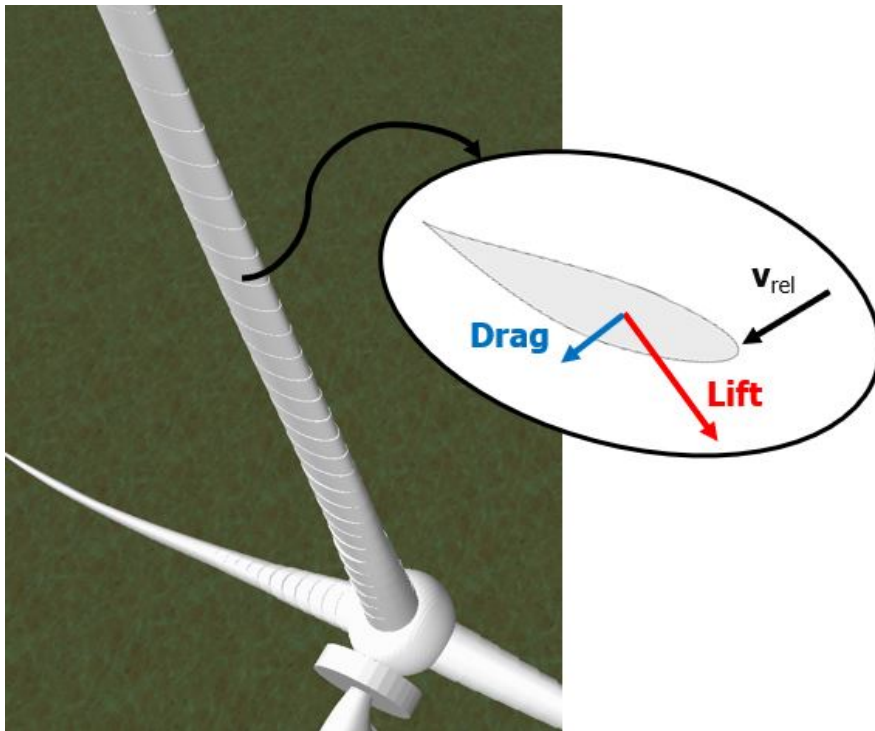
Figure 69: Finite element representation of the rotor as an assembly of wing types

B.2 Torque and Thrust Factors

In this appendix, an analytical expression and a physical interpretation of the torque and thrust factors used in section 8.4.3 are given. Furthermore, section 8.4.3 explains how these factors are integrated and applied in the *Python* code for simulations.

The torque r_{torque} and thrust factor r_{thrust} are both obtained through an empirical approach, utilising simulations for the reference wind turbine. In this process, the ramp-up time and thrust force at zero rotor speed are extracted from the simulations. By observing patterns and trends in the data, it is postulated that both the thrust factor and the torque factor can be approximated using a tangential hyperbolic function. To determine the specific parameters for the hyperbolic function, a sensitivity analysis is conducted. This involves running multiple simulations with varying parameters and evaluating the resemblance of the resulting ramp-up stages to the reference model. Through this analysis, the most suitable parameters are identified and selected.

B.2.1 Torque Factor

It is assumed that this factor depends solely on the wind speed v. Physically, this factor indicates the part of the torque that is independent of the rotor speed and is analytically expressed as:

$$r_{\text{torque}}(\text{v}) = 0.5 - 0.49 \tanh(\text{v} - 5) \,, \tag{56}$$

with the resulting relationship depicted in figure 70 below.
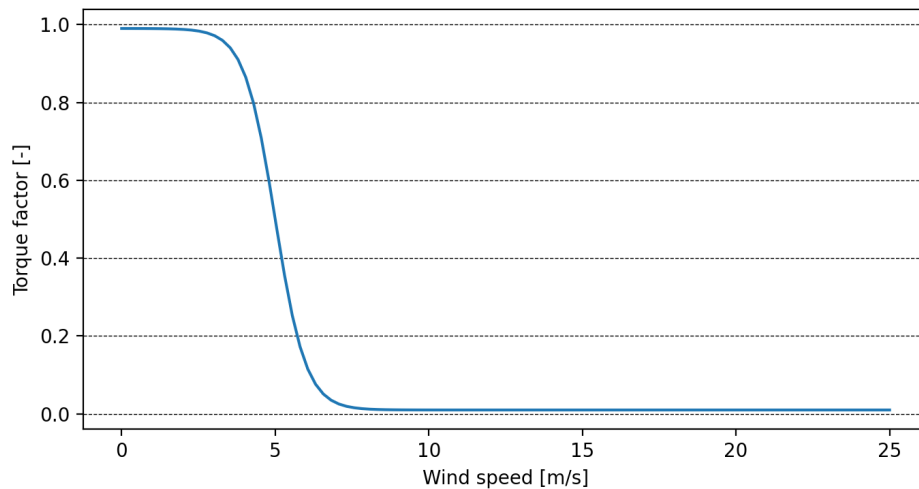
Figure 70: Evolution of the torque factor r_{torque} as a function of the wind speed

To understand the dependency of aerodynamic torque on rotational speed, equation (31) can be

120

consulted. It provides an expression for the relative inflow angle, corresponding to the angle at which the air interacts with the blade. From this equation, it becomes evident that the manner in which the rotor experiences torque is contingent upon the ratio between the incident wind speed and the rotational velocity. When wind speeds are high, small deviations in rotational speed do not significantly impact the relative inflow angle. However, for lower wind speeds, even minor fluctuations in rotational speed result in substantial variations in the relative inflow angle. Consequently, these variations directly influence the lift and drag forces encountered by the blade.

B.2.2   Thrust Factor

In section 8.4.3, a thrust coefficient denoted as r_{thrust} is introduced to account for the portion of thrust that remains independent of rotor speed. Its analytical expression is given by:

$$r_{\text{thrust}}(\mathbf{v}) = 0.04 + 0.6 \tanh\left(\frac{\mathbf{v}^2}{1000}\right) , \tag{57}$$

and the relationship is illustrated in figure 71 below. It was determined through analysis of the reference model, as explained at the beginning of this appendix. From figure 71 and equation (12), it is seen that for higher wind speeds, the proportion of the thrust that is independent of rotor speed is greater.
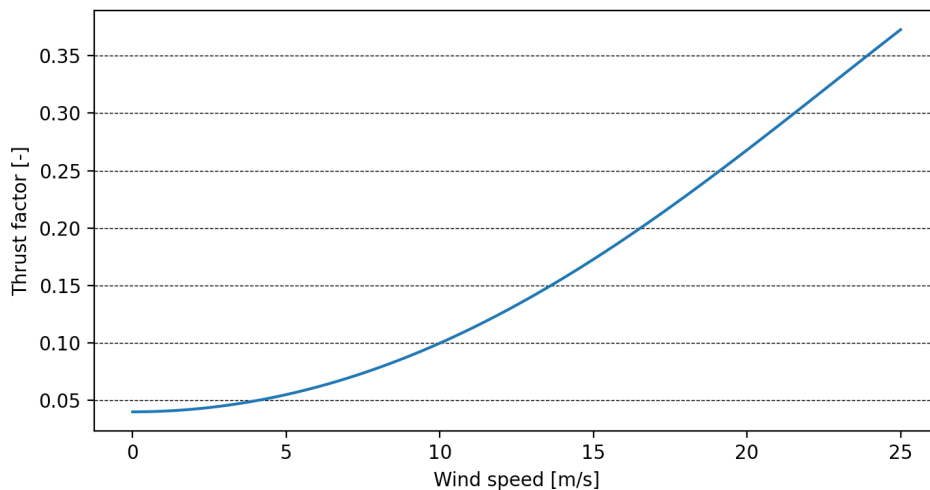
Figure 71: Evolution of the thrust factor r_{thrust} as a function of the wind speed

C APPENDIX - Database

This appendix contains data referenced throughout the report. Appendix C.1 presents the current status of floating offshore wind projects, as well as plans for upcoming years. Additionally, appendix C.2 shows an overview of modelling tools utilised for different domains of floating offshore wind turbines. Appendix C.3 offers a detailed overview of the layout of the reference wind turbine used in this study, focusing on both the turbine and the floating substructure. Furthermore, appendix C.4 specifies the design load cases defined by DNV, while appendix C.5 provides the database for the rotor simplified model employed in section 8.

C.1 Overview of Floating Wind Projects

This appendix presents a comprehensive overview of the current state of floating offshore wind projects. Figures 72, 73 and 74 provide a summary of both upcoming and existing wind projects in Asia, Europe and America respectively. Additionally, a map displaying global projects and prototypes, sourced from [Que23], is included to offer a worldwide perspective.

Project	Country	Status	COD	Capacity (MW)	Water Depth (m)	Developer	Turbine Rating (MW)	Substructure
Fukushima floating offshore wind farm phase 1	Japan	Installed	2013	2	120	Marubeni Corporation	2	Semisubmersible
Fukushima floating offshore wind farm phase 2	Japan	Installed	2015	5	120	Marubeni Corporation	5	Semisubmersible
Sakiyama	Japan	Installed	2016	3	100	TODA Corporation	2	Spar
Kitakyusu (NEDO)	Japan	Under construction	2019	3	70	NEDO—Ideol	3	Semisubmersible
Hitachi Zosen	Japan	Permitting	2024	400	-	Equino—Hitachi	-	Semisubmersible
Macquaire	Japan	Planning	2025	500	100	Macquaire	-	-
Ulsan	South Korea	Financial close	2019	0.75	15	Consortium	0.75	Semisubmersible
Donghae KNOC	South Korea	Planning	2027	-	-	Equinor—KNOC	-	-
Ulsan shell	South Korea	Planning	2027	200	-	Shell—Hexicon	-	Semisubmersible
Ulsan Macquaire	South Korea	Planning	2027	200	-	Macquaire	-	-
Ulsan SK	South Korea	Planning	2027	200	-	SK—E&S	-	-
Ulsan KF	South Korea	Planning	2027	200	-	KF Wind—PPI	-	Semisubmersible
Floatinf W1N	Taiwan	Planning	2025	500	-	Eolfi—Cobra	-	-

Figure 72: Asia's floating wind projects [Día+22]

Project	Country	Status	COD	Capacity (MW)	Water Depth (m)	Developer	Turbine Rating (MW)	Substructure
Eolink 2/10 scale prototype	France	Installed	2018	0.2	10	Eolink	0.2	Semisubmersible
Floatgen project	France	Installed	2018	2	33	Ideol	2	Barge
Groix Belle Ille	France	Approved	2021	24	62	Eolfi	6	Semisubmersible
Provence Grand Large	France	Approved	2021	24	30	EDF	8	Tension Leg Platform
Eolmed	France	Approved	2021	24	62	Ideol	6.2	Barge
Les Eoliennes Flotant du Golfe du Lion	France	Approved	2021	24	71	Engie, EDPR, Caisse de Depots	6	Semisubmersible
GICON Schwimmendes Offshore Fundament SOF Pilot	Germany	Financial close	2022	2.3	37	GICON	2.3	Tension Leg Platform
Hywind Demo	Norway	Installed	2009	2.3	220	Unitech offshore	2.3	Spar
TetraSpar Demostrator	Norway	Financial close	2019	3.6	200	Innogy, Shell, Stiesdal	3.6	Semisubmersible
Hywind Tampen	Norway	Permitting	2022	88	110	Equinor	8	Spar
NOAKA	Norway	Planning	2023	-	130	Equinor. Aker, BP	-	-
Windfloat Atlantic	Portugal	Financial close	2019	25	50	Windplus	8	Semisubmersible
DemoSath—Bimep	Spain	Approved	2020	2	68	Saitec offshore technologies	-	Semisubmersible
X1 Wind prototype—Plocan	Spain	Approved	2021	-	62	X1 wind	-	Tension Leg Platform
Floating Power Plant - Plocan	Spain	Approved	2021	-	62	FPP	8	Hybrid wave power semisubmersible
Hwind Scotland Pilot Park	UK	Installed	2017	30	100	Equinor	6	Spar
Dounreay Tri	UK	Approved	2021	10	76	Hexicon	5	Semisubmersible
Kinkardine Offshore wind farm—Phase 1	UK	Installed	2018	2	62	Cobra	2	Semisubmersible
Kinkardine Offshore wind farm—Phase 2	UK	Under construction	2020	50	62	Cobra	9.5	Semisubmersible

Figure 73: Europe's floating wind projects [Día+22]

Project	Country	Status	COD	Capacity (MW)	Water Depth (m)	Developer	Turbine Rating (MW)	Substructure
Castle Wind	USA	Planning	2027	1000	900	EnBW	8	Semisubmersible
Redwood coast	USA	Planning	2025	150	550	EDPR—PPI	8	Semisubmersible
Aqua Ventus I	USA	Planning	2022	12	100	University of Maine	6	Semisubmersible
Oahu North	USA	Planning	2027	400	850	AW Wind	6	Semisubmersible
Oahu South	USA	Planning	2027	400	600	AW Wind	6	Semisubmersible
Progression Wind	USA	Planning	2027	400	650	Progression Wind	6	Semisubmersible

Figure 74: America's floating wind projects [Día+22]

Q Vision overview of Global Floating Wind Projects and Markets

Worldwide Floating Wind Capacity by Status and Online Year 2023 - 2024

Near-to-medium term Floating Wind Contract Awards Are a $35b Billion Opportunity

Scotland Floating Project Capacity by Developer 2023 - 2024

North & Southern Europe Capacity by Developer under Development & Pre-development Project Outlook 2023 - 2024

Floating Wind Energy
Projects of the World 2023

This map offers insight into the currently known active, planned or forecast Floating Wind Energy projects and associated floating systems. The data is from a proprietary database and remains the copyright of Quest Floating Wind Energy, LLC.
Extensive data on floating wind projects and floating systems & concepts is available in the Q FWE Floating Wind Energy Database.
Please contact Q FWE for more information on data packages or go to QuestFWE.com

Q FWE
www.QuestFWE.com

How to read this map.

Project Status
The floating wind projects shown on this map are from the Quest FWE main 'Vesting' database. We track a project from the earliest intelligence and designate it POSSIBLE. Only when it hits a significant number of boxes for reliability and probability will it move along to status PLANNED.

Preferred Supplier Relationship (PSR)

LEGEND

C.2   Summary of Modelling Tools

	Aerodynamics	Hydrodynamics	Struct. dynamics	Mooring	Control	Simulation	Development/License
3DFloat (Nygaard et al. 2016)	BEMT+DS DI	ME, CE+QD	FE	SM, FE	BPC, VSTC, UD	TD	RIG, CO
ANSYS AQWA (ANSYS 2012)	N/A	PT+CE+(MD+NA), FDE	RB, FE	SM, QS, FE	N/A	FD, TD	IN, CO
aNySIM-PHATAS (Gueydon et al. 2013)	BEMT+DS+DS+DI	ME, CE+QD+MD	MOD	DYN	BPC, VSTC	TD	RIG, PR
BLADED (DNV-GL 2022)	BEMT+DS+DI	ME, CE+QD	MOD, MB	SM, QS, FE	BPC, VSTC, YC	TD	IN, CO
CHARM3D+ FAST (Bae et al. 2011)	(BEMT, GDW)+DS	ME, CE+QD+(MD+NA)	MOD, MB	FE	BPC, VSTC, YC, UD	TD	RIG, PR
Deeplines Wind (Principia 2022)	BEMT+DS	ME, CE+(MD+QTF+NA)	FE	FE	BPC, VSTC, YC, UD	TD	IN, CO
Dymola+ MoWiT (Leimeister et al. 2020a)	(BEMT, GDW)+DS	ME, CE	FE, MOD	DYN	BPC, VSTC	TD	RIG, PR
FAST v8 (Jonkman 2013)	(BEMT,GDW)+DS+DI	ME, CE+QD	MOD, MB, FE	QS, FE, LM	BPC, VSTC, YC, UD	TD	RIG, OS
Flex5 (Jørgensen 2013)	BEMT+DS+DI	ME, CE+QD	FE, MOD	QS	UD	TD	RIG, CO
FloaWDyn (Campos et al. 2017)	(BEMT, GDW)+DS+DI	ME, CE	FE	FE	BPC, VSTC	TD	RIG, PR
HAWC2 (Larsen et al. 2005)	BEMT+DS+ DI	ME, CE+ QD	MB, FE	SM, QS, FE	BPC, VSTC, UD	TD	RIG, CO
hydro-GAST (Manolas 2016)	BEMT, FWV	ME, CE+QD+(MD+NA)	MB, FE	FE	BPC, VSTC	TD	RIG, PR
Mbwind+Lupton PhD thesis (Lupton 2015b)	Lin. BEMT	FDE	SM (Lin. MB)	SM	Lin. (BPC, VSTC)	FD	RIG, OS
MLTSIM-FAST (Koo et al. 2013)	(BEMT, GDW)+DS+DI	CE+QD+(MD+NA)	MOD, MB, FE	QS, FE	BPC, VSTC, YC, UD	TD	IN, PR
MOST (Cottura et al. 2021, 2022; Sirigu et al. 2022)	BEMT	CE+QD	N/A	QS	BPC, VSTC	TD	RIG, PR
OPASS+ FAST (Armendáriz et al. 2011)	(BEMT, GDW)+DS	ME, CE+QD	MOD, MB	LM	BPC, VSTC, YC, UD	TD	RIG, PR
OpenFAST (National Renewable Energy Laboratory 2022b)	(BEMT, GDW)+DS+DI	ME, CE+QD	MOD, MB, FE	QS, FE, LM	BPC, VSTC, YC, UD	TD	RIG, OS
OrcaFlex (Orcina 2022)	(BEMT, GDW)+DS+DI	ME, CE+QD	FE	SM, QS, FE, LM	BPC, VSTC, YC, UD	TD	IN, CO
QuLAF (Pegalajar-Jurado et al. 2018)	DM	FDE	SM (Lin. MB)	SM	Lin. (BPC, VSTC)	FD	RIG, PR

Figure 75: Summary of main modelling tools (I) [Far+22]

	Aerodynamics	Hydrodynamics	Struct. dynamics	Mooring	Control	Simulation	Development/License
SIMA (SIMO/RIFLEX) (MARINTEK 2022)	BEMT+DS+DI	ME, CE+QD+(MD+NA)	MB, FE	SM,QS, FE	BPC,VSTC, UD	TD	IN, CO
Simo+Riflex+ Aerodyn (Ormberg and Bachynski 2012)	(BEMT, GDW)+DS	ME, CE	FE	FE	BPC, VSTC	TD	RIG, PR
Simpack (Matha et al. 2011)	(BEMT, GDW)+DS+DI, FWV, CFD	ME, CE+QD	MOD, MB	SM, QS, MB	BPC, VSTC, YC	TD	IN, CO
SLOW (Lemmer et al. 2020a)	APM	ME, CE, FDE	MOD, MB, SM(Lin. MB)	QS, SM	BPC, VSTC	FD, TD	RIG, PR
UOU+FAST v8 (Ahn and Shin 2019)	(BEMT, GDW)+DS+DI	ME, PT+ CE+QD	MOD, MB, FE	QS, FE, LM	BPC, VSTC, YC, UD	TD	RIG, PR
WAMIT (Newman and Lee 1992)	N/A	PT+(MD+ NA), FDE	RB, MOD	SM	N/A	FD	IN, CO
WINDOPT (Fylling and Berthelsen 2011)	N/A	FDE	RB	QS, FE	N/A	FD	RIG, PR

Aerodynamics BEMT = blade element momentum theory; GDW = generalized dynamic wake; DS = dynamic stall; FWV = free-wake vortex; DI = dynamic inflow; CFD = computational fluid dynamics; APM = actuator point model; FDT = filtered dynamic thrust; DM = damping matrix

Hydrodynamics PT = potential theory; ME = Morrison equation; QD = quadratic drag; MD = mean drift; QTF = quadratic transfer function; CE = Cummins equation; FDE = frequency domain equation; NA=Newman's approximation

Struct. dyn. RB = rigid body; SM = stiffness matrix; MB = multi-body; FE = finite element; MOD = modal

Mooring dynamics QS = quasi-static; FE = finite element; LM = lumped mass; SM = stiffness matrix; DYN = dynamic

Control BPC = blade pitch control; VSTC = variable speed torque control; YC = yaw control; UD = user defined

Simulation FD = frequency-domain; TD = time-domain

Development/License IN = industry; RIG = research institute or group; OS = open-source; CO = commercial; PR = private

Figure 76: Summary of main modelling tools (II) [Far+22]

126

C.3 Reference Wind Turbine
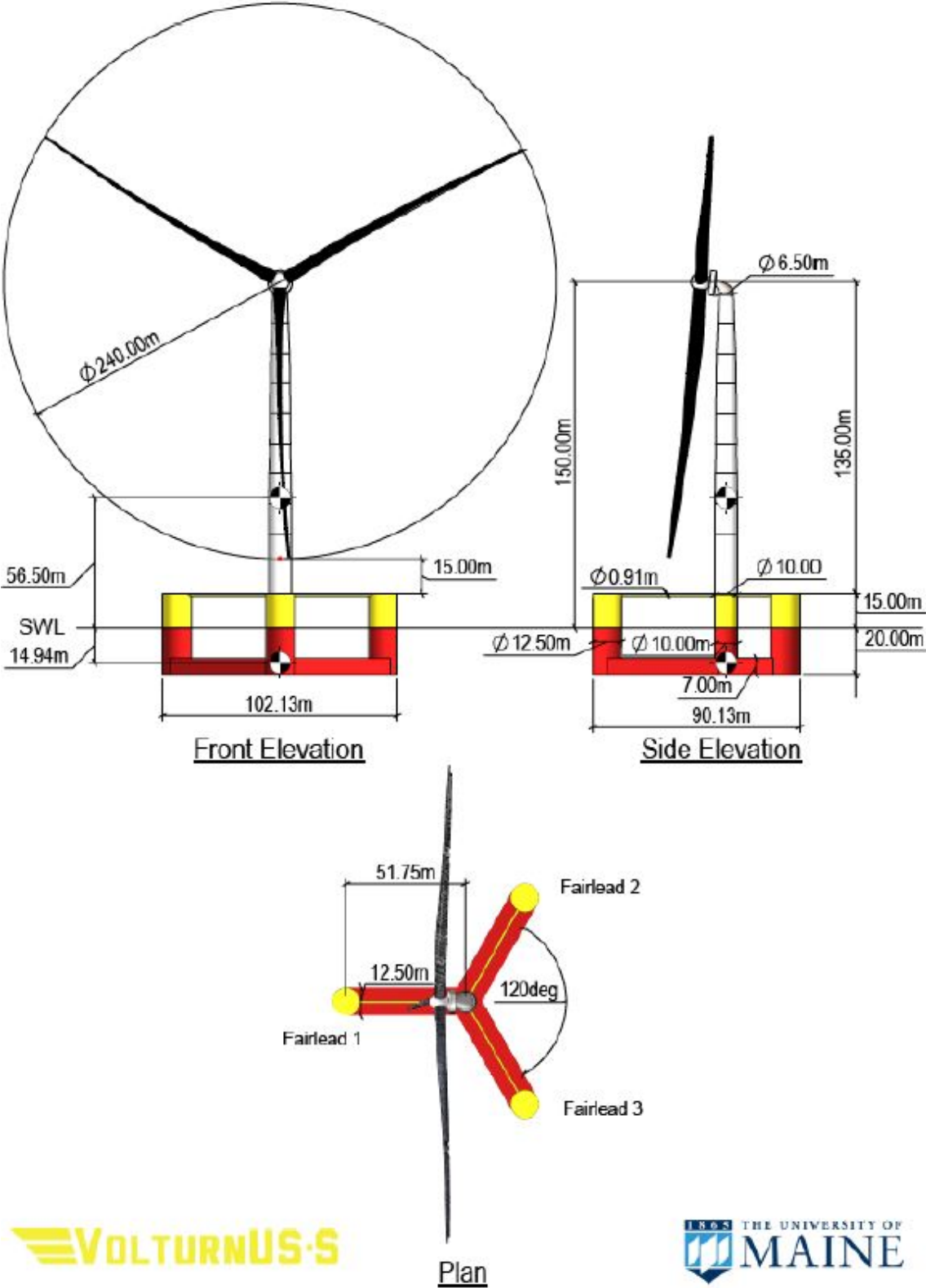
Figure 77: General arrangement of the 15-MW reference FOWT [All+20]

Parameter	Units	Value
Power rating	MW	15
Turbine class	-	IEC Class 1B
Specific rating	W/m^2	332
Rotor orientation	-	Upwind
Number of blades	-	3
Control	-	Variable speed Collective pitch
Cut-in wind speed	m/s	3
Rated wind speed	m/s	10.59
Cut-out wind speed	m/s	25
Design tip-speed ratio	-	9 0
Minimum rotor speed	rpm	5.0
Maximum rotor speed	rpm	7.56
Maximum tip speed	m/s	95
Rotor diameter	m	240
Airfoil series	-	FFA-W3
Hub height	m	150
Hub diameter	m	7.94
Hub overhang	m	11.35
Rotor precone angle	deg	-4.0
Blade prebend	m	4
Blade mass	t	65
Drivetrain	-	Direct drive
Shaft tilt angle	deg	6
Rotor nacelle assembly mass	t	1,017

Parameter	Units	Value
Hull Displacement	m^3	20,206
Hull Steel Mass	t	3,914
Tower Interface Mass	t	100
Ballast Mass (Fixed/Fluid)	t	2,540/11,300
Draft	m	20
Freeboard	m	15
Vertical Center of Gravity from SWL	m	-14.94
Vertical Center of Buoyancy from SWL	m	-13.63
Roll Inertia about Center of Gravity	$kg\text{-}m^2$	1.251E+10
Pitch Inertia about Center of Gravity	$kg\text{-}m^2$	1.251E+10
Yaw Inertia about Center of Gravity	$kg\text{-}m^2$	2.367E+10

Figure 78: Properties of the *IEA Wind 15 MW Offshore Reference Wind Turbine* [Gae+20] (left) and the *VolturnUS-S Reference Platform* [All+20] (right)

C.4 Design Load Cases

The subsequent pages contain tables presenting the various design load cases (DLCs) defined by DNV available within the DNV-ST-0437 standard [DNV21c]. These DLCs serve as a crucial reference for evaluating the performance of a floating offshore wind turbine model. By encompassing both 'normal' and 'extreme' environmental configurations, these DLCs provide a comprehensive understanding of the diverse scenarios that floating structures may encounter and must withstand. The presented DLCs help to define the environmental load cases in this study, as discussed in section 5.2.

Design Situation	DLC	Wind Condition	Waves	Wind and wave directionality	Sea Currents	Water Level	Other Conditions:	Onshore	Offshore	Partial safety factor
1) Power Production:	1.1	NTM $V_{in} < V_{hub} < V_{out}$	NSS $H_s = E[H_s|V_{hub}]$	COD, UNI	NCM	MSL	For extrapolation of extreme loads (offshore – only RNA)	U	U	N (1.25)
	1.2	NTM $V_{in} < V_{hub} < V_{out}$	NSS Joint prob. distribution of H_s, T_p, V_{hub}	MIS, MUL	No Currents	NWLR or ≥ MSL		F/U	F/U	F/N
	1.3	ETM $V_{in} < V_{hub} < V_{out}$	NSS $H_s = E[H_s|V_{hub}]$	COD, UNI	NCM	MSL		U	U	N
	1.4	ECD $V_{hub} = V_r – 2$ m/s, $V_r, V_r + 2$ m/s	NSS $H_s = E[H_s|V_{hub}]$	MIS, wind direction change	NCM	MSL		U	U	N
	1.5	EWS $V_{in} < V_{hub} < V_{out}$	NSS $H_s = E[H_s|V_{hub}]$	COD, UNI	NCM	MSL		U	U	N
	1.6	NTM $V_{in} < V_{hub} < V_{out}$	SSS $H_s = H_{s,SSS}$	COD, UNI	NCM	NWLR		-	U	N
	1.7	NTM $V_{in} < V_{hub} < V_{out}$	NSS Joint prob. distribution of H_s, T_p, V_{hub}	MIS, MUL	No Currents	NWLR or ≥ MSL	Ice formation	F/U	F/U	F/N

Design Situation	DLC	Wind Condition	Marine Condition				Other Conditions:	Type of Analysis		Partial safety factor
			Waves	Wind and wave directionality	Sea Currents	Water Level		Onshore	Offshore	
2) Power Production + occurrence of fault:	2.1	NTM $V_{in} < V_{hub} < V_{out}$	NSS $H_s = E[H_s\|V_{hub}]$	COD, UNI	NCM	MSL	Normal control system fault or primary layer control function fault	U	U	N
	2.2	NTM $V_{in} < V_{hub} < V_{out}$	NSS $H_s = E[H_s\|V_{hub}]$	COD, UNI	NCM	MSL	Abnormal control system fault or secondary layer protection function fault	U	U	A
	2.3	EOG $V_{hub} = V_r \pm 2$ m/s and V_{out}	NSS $H_s = E[H_s\|V_{hub}]$	COD, UNI	NCM	MSL	External or internal electrical fault including loss of electrical network	U	U	A
	2.3 alternatively	NTM $V_{in} < V_{hub} < V_{out}$	NSS $H_s = E[H_s\|V_{hub}]$	COD, UNI	NCM	MSL	External or internal electrical fault including loss of electrical network	U	U	N
	2.4	NTM $V_{in} < V_{hub} < V_{out}$	NSS $H_s = E[H_s\|V_{hub}]$	COD, UNI	No currents	NWLR or ≥ MSL	Normal control system fault or loss of electrical network or primary layer control function fault	F/U	F/U	F/N
	2.5	NWP $V_{in} < V_{hub} < V_{out}$	NSS $H_s = E[H_s\|V_{hub}]$	COD, UNI	NCM	MSL	Fault ride through	U	U	N (1.20)
3) Start up	3.1	NWP $V_{in} < V_{hub} < V_{out}$	NSS $H_s = E[H_s\|V_{hub}]$	COD, UNI	No currents	NWLR or ≥ MSL		F/U	F/U	F/N

Design Situation	DLC	Wind Condition	Marine Condition				Other Conditions:	Type of Analysis		Partial safety factor
			Waves	Wind and wave directionality	Sea Currents	Water Level		Onshore	Offshore	
	3.2	EOG $V_{hub} = V_{in}$, $V_r \pm 2$ m/s, and V_{out} or ETM $V_{in} < V_{hub} < V_{out}$	NSS $H_s = E[H_s\|V_{hub}]$	COD, UNI	NCM	MSL	The timing of the gust and the start-up event chosen for minimum 4 distinct points	U	U	N
	3.3	EDC $V_{hub} = V_{in}$, $V_r \pm 2$ m/s and V_{out}	NSS $H_s = E[H_s\|V_{hub}]$	MIS, wind direction change	NCM	MSL		U	U	N
4) Normal shutdown	4.1	NWP $V_{in} < V_{hub} < V_{out}$	NSS $H_s = E[H_s\|V_{hub}]$	COD, UNI	No currents	NWLR or ≥ MSL		F/U	F/U	F/N
	4.2	EOG $V_{hub} = V_r \pm 2$ m/ sand V_{out} or ETM $V_{in} < V_{hub} < V_{out}$	NSS $H_s = E[H_s\|V_{hub}]$	COD, UNI	NCM	MSL	The timing of the gust and the shutdown event chosen for minimum 6 distinct points	U	U	N
5) Emergency stop	5.1	NTM $V_{hub} = V_r \pm 2$ m/ sand V_{out}	NSS $H_s = E[H_s\|V_{hub}]$	COD, UNI	NCM	MSL	Azimuth position at the time of the emergency stop shall be randomly selected	U	U	N

Design Situation	DLC	Wind Condition	Marine Condition				Other Conditions:	Type of Analysis		Partial safety factor
			Waves	Wind and wave directionality	Sea Currents	Water Level		Onshore	Offshore	
6) Parked (standing still or idling)	6.1	EWM $V_{hub} = V_{ref}$	ESS $H_s = H_{s,50}$	MIS, MUL	ECM $U = U_{50}$	EWLR	Yaw misalignment of ±8 deg Possible yaw slippage	U	U	N
	6.2	EWM $V_{hub} = V_{ref}$	ESS $H_s = H_{s,50}$	MIS, MUL	ECM $U = U_{50}$	EWLR	Loss of electrical network Yaw misalignment of ±180°	U	U	A
	6.3	EWM $V_{hub} = V_1$	ESS $H_s = H_{s,1}$	MIS, MUL	ECM $U = U_1$	NWLR	Extreme yaw misalignment Yaw misalignment of ±20 deg	U	U	N
	6.4	NTM $V_{hub} < V_{in}$ and $V_{out} < V_{hub} < 0,7$ V_{ref}	NSS Joint prob. distribution of H_s, T_p, V_{hub}	COD, MUL	No currents	NWLR or ≥ MSL	Investigation of natural frequencies during idling	F/U	F/U	F/N
	6.5	EWM $V_{hub} = V_1$	ESS $H_s = H_{s,1}$	MIS, MUL	ECM $U = U_1$	NWLR	Ice formation on structure	-	U	N
7) Parked and fault conditions:	7.1	EWM $V_{hub} = V_1$	ESS $H_s = H_{s,1}$	MIS, MUL	ECM $U = U_1$	NWLR	Fault that produces deviations from the normal turbine behaviour while parked; including loss of electrical network	U	U	A

Design Situation	DLC	Wind Condition	Marine Condition				Other Conditions:	Type of Analysis		Partial safety factor
			Waves	Wind and wave directionality	Sea Currents	Water Level		Onshore	Offshore	
	7.2	NTM $V_{hub} < V_{out}$	NSS Joint prob. distribution of H_s, T_p, V_{hub}	COD, MUL	No currents	NWLR or ≥ MSL		-	F/U	F/N
8) Transport, installation, maintenance and repair	8.1	NTM $V_{hub} = V_T$ to be stated by the manufacturer	NSS $H_s = H_{sT}$ to be stated by the manufacturer	COD, MUL	No currents	NWLR	Design conditions shall be stated by the manufacturer	U	U	N
	8.2	EWM $V_{hub} = V_1$	ESS $H_s = H_{s,1}$	COD, MUL	No currents	NWLR	Transport, installation, maintenance and repair	U	U	A
	8.3	EWM $V_{hub} = V_1$	ESS $H_s = H_{s,1}$	COD, UNI	ECM $U = U_1$	NWLR	Vortex-induced vibrations due to wind, waves or currents	F/U	F/U	F/N
	8.4	NTM $V_{hub} < 0,7V_{ref}$	NSS Joint prob. distribution of H_s, T_p, V_{hub}	COD, MUL	No currents	NWLR or ≥ MSL	No grid during installation period	-	F/U	F/N
	8.5	NTM $V_{hub} = V_T$	ESS $H_s = H_{sT}$	COD, MUL	ECM $U = U_1$	NWLR	Service vessel impact and helicopter loads – normal event	-	U	N
	8.6	NTM $V_{hub} = V_T$	ESS $H_s = H_{sT}$	COD, MUL	ECM $U = U_1$	NWLR	Supply vessel impact – abnormal event	-	U	A

133

C.5 Database for Rotor Simplification

C.5.1 Database for the Thrust

Table 12: Database for aerodynamic thrust at different wind speeds for the rotor simplified representation

Wind Speed [m/s]	Thrust [kN]		
0	0.00	20	987.41
0.5	5.73	20.5	969.59
1	22.94	21	952.07
1.5	51.61	21.5	938.61
2	91.75	22	919.10
2.5	143.36	22.5	901.96
3	206.44	23	889.42
3.5	280.99	23.5	875.61
4	367.00	24	866.10
4.5	464.49	24.5	851.86
5	573.44	25	841.53
5.5	693.86	25.5	831.19
6	825.75	26	820.86
6.5	969.11	26.5	810.53
7	1035.26	27	800.19
7.5	1198.39	27.5	789.86
8	1359.64	28	779.53
8.5	1465.58	28.5	769.19
9	1585.62	29	758.86
9.5	1768.83	29.5	748.53
10	1864.82	30	738.19
10.5	1775.90	30.5	727.86
11	1687.86	31	717.53
11.5	1634.10	31.5	707.19
12	1611.52	32	696.86
12.5	1597.18	32.5	686.53
13	1528.30	33	676.20
13.5	1464.43	33.5	665.86
14	1405.47	34	655.53
14.5	1346.41	34.5	645.20
15	1289.38	35	634.86
15.5	1246.60	35.5	624.53
16	1211.04	36	614.20
16.5	1179.61	36.5	603.86
17	1141.73	37	593.53
17.5	1107.31	37.5	583.20
18	1081.09	38	572.86
18.5	1057.30	38.5	562.53
19	1037.25	39	552.20
19.5	1010.73	39.5	541.86
		40	531.53

C.5.2 Database for the Blade Pitch

Table 13: Database for blade pitch at different wind speeds for the rotor simplified representation

Wind Speed [m/s]	Blade Pitch [deg]		
0	3.44	20	15.04
0.5	3.44	20.5	15.56
1	3.44	21	16.08
1.5	3.44	21.5	16.58
2	3.44	22	17.09
2.5	3.44	22.5	17.58
3	3.44	23	18.07
3.5	3.44	23.5	18.56
4	3.44	24	19.04
4.5	3.30	24.5	19.52
5	2.84	25	21.44
5.5	2.25	25.5	54.10
6	1.57	26	87.97
6.5	0.82	26.5	90.00
7	0.06	27	90.00
7.5	0.00	27.5	90.00
8	0.00	28	90.00
8.5	0.00	28.5	90.00
9	0.00	29	90.00
9.5	0.02	29.5	90.00
10	0.73	30	90.00
10.5	2.08	30.5	90.00
11	3.23	31	90.00
11.5	3.98	31.5	90.00
12	4.66	32	90.00
12.5	5.33	32.5	90.00
13	6.18	33	90.00
13.5	7.01	33.5	90.00
14	7.79	34	90.00
14.5	8.52	34.5	90.00
15	9.21	35	90.00
15.5	9.87	35.5	90.00
16	10.50	36	90.00
16.5	11.12	36.5	90.00
17	11.72	37	90.00
17.5	12.30	37.5	90.00
18	12.87	38	90.00
18.5	13.43	38.5	90.00
19	13.97	39	90.00
19.5	14.51	39.5	90.00
		40	90.00

C.5.3 Database for the Aerodynamic Torque

Table 14: Database for aerodynamic torque at different wind speeds for the rotor simplified representation

Wind Speed [m/s]	Torque [kN.m]	Wind Speed [m/s]	Torque [kN.m]
0	0	20	19786
0.5	1.60	20.5	19786
1	6.01	21	19786
1.5	13.46	21.5	19786
2	24.46	22	19786
2.5	39.95	22.5	19786
3	127.33	23	19786
3.5	578.89	23.5	19786
4	1152.94	24	19786
4.5	1879.43	24.5	19786
5	2850.97	25	19786
5.5	4036.74	25.5	0
6	5442.27	26	0
6.5	7064.16	26.5	0
7	8888.12	27	0
7.5	10236.68	27.5	0
8	11606.93	28	0
8.5	13043.90	28.5	0
9	14539.70	29	0
9.5	16027.64	29.5	0
10	16690.28	30	0
10.5	16658.06	30.5	0
11	17364.30	31	0
11.5	18446.77	31.5	0
12	19500.71	32	0
12.5	19786	32.5	0
13	19786	33	0
13.5	19786	33.5	0
14	19786	34	0
14.5	19786	34.5	0
15	19786	35	0
15.5	19786	35.5	0
16	19786	36	0
16.5	19786	36.5	0
17	19786	37	0
17.5	19786	37.5	0
18	19786	38	0
18.5	19786	38.5	0
19	19786	39	0
19.5	19786	39.5	0
		40	0

136